
Chapter 18

Space-Based Remote Sensing Radars

R. Keith Raney

Johns Hopkins University Applied Physics Laboratory

18.1 PERSPECTIVE

Motivation. Worldwide, the rate of investment in space-based radar (SBR) during the time the radars in this chapter were operating was on the order of one billion dollars per year. Space-based synthetic aperture radar (SAR) systems capable of 1-m resolution have become the norm, with systems under development or already launched by at least seven countries. As expanded in the appropriate sections of this chapter, the (range) measurement precision of surface height change is now on the order of 1 millimeter per year, as established by two different classes of Earth-observing SBRs (SARs and radar altimeters). Several nations are sponsoring radars for exploration at the Moon and beyond. SBR-related patent applications continue apace. In short, SBR is an exciting, exacting, extensive, and expanding topic.

Space-based radar systems face fundamental challenges. The permissible options for the value of several parameters (such as pulse repetition frequency) are more restricted for SBR than for airborne systems. Likewise, the hardware environment imposes more rigorous constraints on implementation, and SBR systems do not enjoy the luxuries of hands-on maintenance nor in-field parts replacement. However, the payoff from radars in space more than compensates for these challenges, since space offers a unique perspective for Earth observation and is an essential viewpoint for lunar or planetary exploration.

Covered and Omitted Topics. This chapter introduces space-based remote sensing radars. The focus is on Type II SBRs, as outlined in the previous edition of this *Handbook*, including both Earth-orbiting and planetary systems. The material in this chapter is designed to be reasonably complete at a survey level; the discussion zooms in on selected case examples to illustrate application-specific implementations or technological innovations. An outstanding early example is the Seasat satellite launched in 1978 (Figure 18.1), which (as its name suggests) was designed for oceanic observations. Three of its sensors were SBRs—a synthetic aperture radar, an altimeter, and a scatterometer. As the reader will discover in this chapter, these three Seasat instruments established the initial paradigm for virtually all subsequent radars of their respective classes.^{1,2}

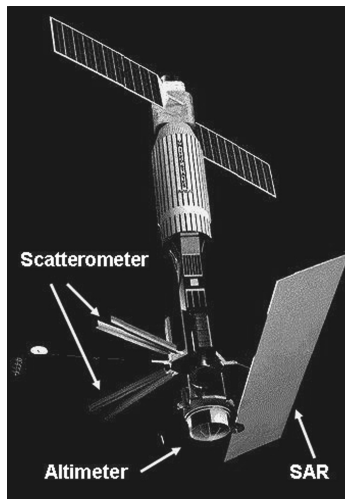


FIGURE 18.1 The Seasat satellite, featuring the antennas of its three radars (*Courtesy of NASA*)

This chapter does not cover the Type I short-range specialized SBR systems reviewed in earlier editions, such as terminal guidance or rendezvous radars. Also not covered are Type III SBRs, such as multi-spacecraft systems for space-based radar surveillance of the Earth's surface or airspace. (Although these large SBR concepts are interesting in principle, their implied costs remain a disincentive, particularly if their erstwhile sponsors expect their performance to approach the current state-of-the-art in airborne search or surveillance radars.) Except for the mention of a few basic concepts, this chapter does not delve into the extensive subjects of orbitology, implementation of space-qualified hardware, nor system integration and test, for which the interested reader is directed to standard references.^{3,4}

Basic Orbit Characteristics. Unlike an airborne platform that can go anywhere at any time (subject to fuel and air-space limitations), a satellite's position and velocity when in orbit about a planetary body are rigidly governed by orbital dynamics, summarized compactly by Kepler's laws. Further, access by an SBR to a given area of interest depends on the rotation rate of the planet, as well as the satellite's position along its orbit and the radar's viewing geometry. Thus, the primary parameters to be included in SBR mission design include orbital altitude, spacecraft on-orbit velocity (and hence period), orbit inclination, and the rotation rate of the planet.

Earth-observing SBRs, such as SARs, tend to operate from spacecraft in near-circular low-Earth orbits (LEO). Typical LEO altitudes span 500 km to 850 km. Lower altitudes incur larger atmospheric drag, whereas higher altitudes imply higher radiation levels and longer radar ranges, neither of which are desirable in most situations. Spacecraft velocities at these LEO altitudes are on the order of 7.5 km/s; their corresponding periods are about 100 minutes. Earth rotation (at a rate of ~0.25 degree/min) shifts the sub-satellite point at the equator by ~3300 km orbit-to-orbit. The orbit altitude normally may be chosen to tune the period and Earth rotation rate so that an exact-repeat pattern develops that has a stipulated number of days. The repeat period

often is an integral number, such as the 24-day repeat of RADARSAT, although a non-integral period may be preferred, such as the 9.916-day repeat of the TOPEX/Poseidon radar altimeter. Orbit parameters such as repeat period must be maintained, requiring small boosts from spacecraft thruster maneuvers,⁴ typically applied every several weeks for LEO missions. The revisit time of a given SBR asset depends on the range swath width covered by the radar in question, as well as the orbit's exact-repeat period and the latitude of the site of interest. The off-nadir^{*} look angle of certain SBRs can be adjusted to increase the effective revisit rate. Note that orbit maneuvers are not a practical means to improve the frequency of site coverage, since a large change in altitude (hence velocity), or especially any change of orbit inclination (the angle of the inertial orbit plane with respect to the Earth's equator), would require a substantial expenditure of precious onboard fuel resources.³

The Earth is flattened at the poles, due primarily to its relatively rapid rotation. The resulting lack of spherical symmetry in the gravity field at orbital altitude imposes small lateral forces on an inclined orbit plane, which consequently precesses in inertial space. The amount, direction, and rate of orbit precession can be controlled by choice of the inclination and the mean altitude of the orbit. Many satellite platforms use this degree of freedom to generate a sun-synchronous orbit, which is one that maintains a constant angle of its orbit plane relative to solar illumination over the entire year. The European Space Agency's Envisat spacecraft is a good example of a sun-synchronous LEO, having ~98.5° inclination[†] and 785 km altitude. Sun-synchronous spacecraft that host optical instruments (such as Japan's ALOS) choose the phase of the sun angle to favor illumination of the surface, which usually leads to a midday orbit from which most of the Earth's surface is viewed at about the same local time, near midday. Such orbits imply that the spacecraft must pass through the Earth's shadow about half the time, which has consequences on the design of the thermal and power subsystems in particular. In contrast, spacecraft that carry only radars, such as RADARSAT, tend toward favorable illumination of the spacecraft. The natural result in this case is the so-called dawn-dusk orbit, in which the satellite—and its solar-panel-dependent power system—avoids the shadow of the Earth almost always for almost all seasons.

Certain applications are particularly well-served by exact-repeat orbits. For example, if a group of orbital trajectories falls within a small radius of each other when over an area of interest, then radar measurements from several orbits may be compared coherently, thus potentially sensitive at the order of a wavelength to changes in the scene between observations. Such coherent change detection is a standard technique in the field of space-based SAR interferometry, reviewed in the following section. Exact-repeat orbits are standard for most radar altimeters, but for geophysical reasons, not for mutual coherency. Sun-synchronicity presents its own problems for ocean-sensing altimeters. These comments are elaborated in Section 18.3.

As discussed in several chapters of this book, the performance of doppler-sensitive radars is conditional upon the velocity of their host platform. The velocity of a spacecraft in orbit at altitude h above a planet of radius R_p and mass M_p is given by

$$V_{SC} = \sqrt{M_p G / (R_p + h)} \quad (18.1)$$

^{*} Nadir is the point below the spacecraft on the surface intersected by the radius vector from the Earth's center to the spacecraft.

[†] Inclinations greater than 90° are retrograde because their E-W velocity component in the ascending pass is contrary to the direction of the Earth's rotation, in contrast to prograde orbits whose inclinations are less than 90°.

TABLE 18.1 Spacecraft Velocities

Body	Mass (kg)	Radius (km)	Altitude h (km)	V_{SC} (m/s)	hV_{SC} (km 2 /s)
Earth	5.97×10^{24}	6380	800	7466	6000
Venus	4.87×10^{24}	6052	300	7151	2200
Mars	6.4×10^{23}	3397	400	3353	1600
Ganymede	1.4×10^{23}	2631	100	1849	185
Calisto	1.08×10^{23}	2400	100	1697	170
Moon	7.35×10^{22}	1737	100	1634	160
Europa	4.8×10^{22}	1569	100	1385	140

where G is the universal gravity constant[‡] 6.67×10^{-11} Nm 2 kg $^{-2}$. Table 18.1 lists representative spacecraft velocities for bodies in the solar system that have been visited, or are likely to be observed, by range-doppler radars. Feasible satellite altitudes are limited below by the prevailing atmospheric density. The final column of the table lists the altitude-velocity product hV_{SC} corresponding to each entry. This product is a scaling factor that characterizes the range-doppler space confronting an SBR intended to be deployed in that environment. There is approximately a 40-fold spread in the value of this parameter, from the Earth to Jupiter's moon Europa. It follows that radar designs that work in one situation may not be at all appropriate if migrated to a different planetary body.

It is often said that radar is "all-weather," but this generalization clearly is not universally true, especially for SBRs. From space, the ionosphere and/or atmosphere may corrupt or even prevent radar propagation. The ionosphere may induce Faraday rotation,[§] thus degrading or destroying the polarization properties of the transmitted and received signals.⁴ The Faraday rotation β of a linearly-polarized E-vector is proportional to RM λ^2 , where the rotation measure RM is a function of ionospheric electron density. The ionosphere also introduces dispersion and, under certain unfavorable circumstances, effectively cuts off propagation. Thus, for example, it was not possible for the 5-MHz MARSIS radar sounder to probe the Martian surface during daylight hours, because the cutoff frequency under those conditions increased to about 10 MHz. Thus, MARSIS worked as a surface sounder during dark hours and as an ionospheric sounder during daylight hours. More on the MARSIS radar may be found in Section 18.6. The 12-cm wavelength of the Magellan Venus radar (reviewed in Section 18.4) was chosen in response to the trade-off between propagation through Venus' very dense atmosphere (for which longer wavelengths would be better) and synthetic aperture radar system considerations (for which shorter wavelengths would be better). Propagation speed is retarded along the path length from an ocean-viewing altimeter to the Earth by a very small fraction of the speed of light, but sufficient nevertheless to impose range measurement errors of many meters. These errors must be estimated and compensated before the required cm-level accuracy can be achieved, as summarized in Section 18.3.

Comments on Hardware. On a popular American children's television program, one is told that "It is not easy being green." Likewise, it is not easy being

[‡] N is the standard symbol for Newton, force, with the units m kg s $^{-2}$.

[§] The plane of polarization of an EM wave is perturbed by interaction with the magnetic field through which it passes, an effect discovered by Faraday.

a radar, especially aboard a spacecraft. Because a radar by definition must transmit, its near-field radiation is a potential threat to all other instruments and subsystems of the host spacecraft and its payload. Once having got past the risk (or paranoia) of near-field radiation, normal spacecraft design principles kick in. The first order considerations on hardware that are characteristic of (and essentially unique to) the space environment include radiation and energetic particles, vibration (especially during the launch phase), harsh and contrasting thermal environments, often challenging mass limitations, and a premium on payload power. In Earth orbit and, perhaps surprisingly, also at the Moon, a space-based radar must comply with internationally agreed spectral allocations. These limit both the available bands and the bandwidths, which impact system design and may constrain certain performance objectives, such as resolution.

Since it is expensive to get to orbit, SBRs, like other space-based systems, must be designed to minimize mass and to maximize efficiency and longevity. Mass, power, and lifetime emerge as driving themes that dictate conservative design, generous margins during system implementation, and redundancy often realized by dual-string hardware in most if not all subsystems other than the antenna.

Organization of the Chapter. The chapter sections are organized by measurement theme, taken in a broad sense. These themes are Earth-orbiting synthetic aperture radar (SAR), radar altimetry (which in the SBR context almost always implies observation of the Earth's oceans and larger surface water bodies), planetary radars (where "planet" includes planetoids such as large moons), scatterometers (whose data associate a geophysical parameter such as oceanic wind speed to the observed calibrated radar backscatter properties of the illuminated surface), and sounders (which includes both atmospheric and subsurface radar systems). Each section includes an overview of all relevant SBRs, noting key turning points or watershed innovations in the theme's history. Selected examples have been chosen for more in-depth review. Online web sites are suggested for each cited instrument; these web sites were accessible at the date of publication of this book.*

18.2 SYNTHETIC APERTURE RADAR (SAR)

In its most general form, an imaging radar is a device designed to provide a two-dimensional portrayal of the radar backscatter returning from the field illuminated in range and azimuth. Space-based microwave imagers are synthetic aperture radars (with the exception of certain early Soviet ocean-observing real-aperture systems). As with all imaging systems, SAR image products are rated according to their resolution, where "higher" is "better." Higher resolution always implies wider bandwidth in both range and azimuth. Azimuth bandwidth derives from the doppler signatures set up by the motion of the radar with respect to the illuminated field. Resolution by itself is not sufficient to determine the image quality of importance to most applications.

* The field of space-based remote sensing radars is subject to rapid change. This chapter provides the view from the early 21st century. Readers are encouraged to seek currently topical information through online resources. Keywords, such as the names of the mission, nationality, and radar, are usually sufficient to locate several references. Alert: Not all online resources are accurate; the reader is advised to seek out more than one and to verify information by cross-comparison.

SAR images are degraded by a multiplicative self-noise known as *speckle*, which is a direct consequence of the coherence required by the radar-processor combination to form the synthetic aperture and the resulting enhanced resolution. Speckle can be reduced only through supplemental incoherent processing, multi-looking in SAR jargon. Additional looks require proportionally more bandwidth. It follows that large two-dimensional bandwidth (range and azimuth) is the driving requirement for this class of radar.

Space-based SAR systems have motivated fruitful specializations in quantitative applications in a wide variety of areas, comprehensively reviewed in the *Principles and Applications of Imaging Radar*.⁵ Topics such as SpotSAR, ScanSAR, polarimetry, and interferometry that have influenced radar system and mission design are outlined in closing paragraphs of this section.

Flight Systems. The concept of SAR, introduced in 1951 by Carl Wiley,⁶ was reduced to practice in subsequent years, first through simulations, then through airborne proof-of-concept systems.⁷ Quill, the first space-based SAR (see Table 18.2), was launched only a decade later. (That was a remarkable achievement, considering that in the modern era, it often takes nearly 20 years to go from concept to launch of a new SAR, even though the principles and technology for these SBRs are by now well established.) Quill was rudimentary, but did succeed in generating data sufficient to form images. The nominal 100-m resolution was spectacular for its time, given that the best resolution that could be expected from an otherwise comparable real-aperture SBR would be on the order of kilometers. Nevertheless, the results did not meet the needs of the sponsor, and so the notional second and third missions were never launched. Quill was the only American SBR whose data were optically recorded onboard, eventually returned to Earth by ejected capsule, and then collected by an airborne retrieval maneuver.

TABLE 18.2 Synthetic Aperture Radars (Earth-viewing)

Satellite/SAR	URL	Country	Launch	Res (m)	Band	Polarization
Quill	1	USA	1964	(>100 m)	X	
Seasat	2	USA	1978	25	L	HH
SIR A; B	3	USA	1981; '84	40; ~25	L	HH
SIR C	4	USA; G, I	1994, '94	~30	L&C; X	Various to quad; HH
Kosmos 1870	5	USSR	1987	15–30	S	HH
Almaz	6	USSR	1991	15–30	S	HH
ERS-1	7	ESA	1991	25	C	VV
J-ERS-1	8	Japan	1992	30	L	HH
RADARSAT-1	9	Canada	1995	8, 25, 50, 100	C	HH
ERS-2	10	ESA	1995	25	C	VV
Priroda	11	Russia/Ukraine	1996	50	S, L	HH, VV
SRTM	12	USA; G, I	2000	~30	C, X	HH, VV
ENVISAT	13	ESA	2002	10, 30, 150, 1000	C	VV or HH, dual
IGS-1B	14	Japan	2003+	1, +	X	Multimode
PALSAR	15	Japan	2006	2.5–100	L	Various to Quad
JianBing-5	16	China	2006	3–20	L	Multi-polarimetric
TerraSAR-X	17	Germany	2007	1, 3, 15	X	Various
RADARSAT-2	18	Canada	2007	1, 3, 25, 100	C	Various to Quad
COSMO	19	Italy	2007	1, 3, 25, 100	X	Multi-polarimetric
TecSAR	20	Israel	2007	1–8	X	Multimode

TABLE 18.2 Synthetic Aperture Radars (Earth-viewing) (*Continued*)

Satellite/SAR	URL	Country	Launch	Res (m)	Band	Polarization
Kondor-E	21	Russia	2007	1, +	S	Multimode
HJ-1-C	22	China	2007	1, +	S	Multimode
SAR-Lupe	23	Germany	2007	0.12, +	X	Multimode
Arkon-2	24	Russia	2008	1–50	S, L, P	Multimode
RISAT	25	India	2008	1–50	C	Various to Quad
Tandem-X	26	Germany	2009	1, 3, 15	X	Various to Quad
Radarsat-C	27	Canada	—	1, +	C	Various to Quad
MAPSAR	28	Brazil/Germany	—	3–20	L	Single, dual, quad
Sentinel-1	29	Europe	—	4–80	C (L)	Various to Quad

1. http://www.skyrocket.de/space/index_frame.htm?http://www.skyrocket.de/space/sat_mil_usa.htm
2. <http://www.astronautix.com/craft/seasat.htm>
3. http://directory.eoportal.org/pres_SIRShuttleImagingRadarMissions.html
4. <http://southport.jpl.nasa.gov/>
5. <http://www.astronautix.com/craft/almazt.htm>
6. <http://www.russianspaceweb.com/almazt.html>
7. <http://earth.esa.int/ers/>
8. http://www.nasda.go.jp/projects/sat/jers1/index_e.html
9. <http://www.space.gc.ca/asc/eng/satellites/radarsat1>
10. http://en.wikipedia.org/wiki/Space-Based_Radar
11. <http://www.astronautix.com/craft/priroda.htm>
12. <http://www2.jpl.nasa.gov/srtm/>
13. <http://envisat.esa.int/object/index.cfm?fobjectid=3772>
14. http://www.space.com/spacenews/archive03/spyarch_040903.html
15. <http://www.eorc.jaxa.jp/ALOS/about/palsar.htm>
16. <http://www.sinodefence.com/strategic/spacecraft/jianbing5.asp>
17. http://www.caf.dlr.de/tsx/start_en.htm
18. http://www.space.gc.ca/asc/eng/satellites/radarsat2/inf_over.asp
19. http://directory.eoportal.org/pres_COSMOSkyMedConstellationof4SARSatellites.html
20. <http://www.iai.co.il/Default.aspx?docID=32812&FolderID=14469&lang=en&res=0&pos=0>
21. <http://www.npmash.ru/space/en/space1.htm>
22. http://www.eohandbook.com/eohb05/pdfs/missions_alpha.pdf#search=%22China%20HJ-1C%20satellite%20radar%22
23. http://directory.eoportal.org/pres_SARLupeConstellation.html
24. http://industry.esa.int/ATTACHEMENTS/A112/nfm2005_04.pdf#search=%22Japan%20space%20radar%20IG-S-R1%22
25. http://directory.eoportal.org/info_RISATRadarImagingSatellite.html
26. http://directory.eoportal.org/info_TanDEMXTerraSARXaddonforDigitalElevationMeasurement.html
27. <http://www.mdacorporation.com/news/pr/pr2006031301.htm>
28. <http://elib.dlr.de/43957/>
29. <http://www.gmes.info/>

Seasat. The generally acknowledged space-based synthetic aperture radar pioneer was the 1978 Seasat SAR (Figure 18-1). That L-band system⁸ persists as the design paradigm for Earth-observing space-based SARs. Seasat illustrates several characteristics of many civilian Earth-observing SARs, including the size and aspect ratio of the antenna (10.74 m by 2.1 m), its relatively steep angle of incidence (~22°), its swath width (100 km), and use of a linear FM (chirp) modulated pulse waveform (634:1 compression ratio). Seasat SAR's average radiated power was relatively small (55 W) although its peak power was appreciable (1 kW). The antenna was passive, consisting of eight flat microstrip panels, radiating and receiving HH polarization. There was no onboard recorder, so data were downlinked, but only, of course, when in radio visibility of one of the four ground stations (in the United States, Canada, and the United Kingdom) that were equipped to receive the data. Telemetry was

analog (20 MHz, offset video), to be converted on the ground to either optical media (transparent film strips) or digitized (5-bit quantization). Imagery was generated (but not immediately[†]) by either optical or digital processing methods. The Seasat satellite suffered a massive short circuit in its primary power system (in the solar panel slip-ring assembly), which ended its mission in October 1978 after only three months of operation.

SIR SAR Series. The Shuttle imaging radars, SIR-A (which flew on the first Shuttle that carried a science payload), SIR-B, and SIR-C/X-SAR were essentially technology (and science) demonstrations missions,^{2,9} each lasting about one week or less. In sequence, these radars had increasingly more capability in terms of incidence, frequency, and polarization. SIR-C/X-SAR operated at three bands: C and L (USA) and X (contributed through an international partnership with Germany and Italy). Data from SIR-C continues in demand, thanks to its fully polarimetric multiband coverage of a wide variety of scenes.¹⁰ The Shuttle Radar Terrain Mapper¹¹ (SRTM) was an outgrowth of SIR-C, using a small receiving antenna (at X and C band) mounted on a 60-m long extendable strut, to collect simultaneous backscatter subsequently processed into topographic maps. This was the first demonstration of single-pass space-based interferometric SAR capability (InSAR). Data were collected over a very large fraction of the global landmass.

Kosmos. Although not classified in the strict sense, Kosmos came to view largely after the launch of its technical successor, Almaz (Russian and Arabic for *diamond in the rough*). Preceding these Soviet SARs were a series of real-aperture radars, known as *Okean* (and by other names). Almaz was a very interesting radar, in that it provided unique S-band SBR imagery of the Earth's surface. The technology behind this and related Russian systems continued to be developed, culminating in the Kondor-E radar and, through a bilateral technology exchange program, the HJ-1-C SAR of China.¹² Both of these radars use the 6-m parabolic reflector developed originally for Priroda, the final module for the Russian MIR complex. Travers, the radar aboard Priroda, was an experimental demonstration mission. There are at least three members of the X-band national asset SAR fleet, including TecSAR¹³ (Israel) and the IGS-R series (Japan). The first IGS-R was launched in 2003. The 2005 launch of a sequel failed.

ERS-1 and ERS-2. The C-band SARs from the European Space Agency (ESA) introduced operational space-based SAR capability.¹⁴ Since the launch of the first European Radar Satellite (ERS-1), ESA SARs have maintained a continuous record of outstanding performance. ERS-1 and its followers have had onboard data recording capability. ERS-1 and ERS-2 had in common ~25-m resolution at 4 looks, 100-km swath width, and ~23° incidence, all in the pattern of the Seasat SAR. The two ERS SARs were virtually identical. ERS-1 and ERS-2 enjoyed about one year of simultaneous operation, organized by ESA to chase each other so that their joint repeat visit was only one day. This lead to the accumulation of a unique data set, especially valuable for coherent change detection measurements¹⁵ (two-pass InSAR). The ERS SAR instrument was a subset of a combined radar group, the Active Microwave Instrument (AMI), comprised of a scatterometer and a wind/wave mini-SAR mode, as well as the SAR itself.

[†] The first digitally processed images from the Seasat SAR required 40 hours for a quarter-frame (50 km square) on a mainframe computer.

(The scatterometer mode is described in Section 18.5.) The wind/wave mode, based on the SAR, was designed to grab 10-km square snapshot images of the ocean surface, which could be processed (onboard or later in a ground facility) to estimate wind speed and direction from the radar brightness and wave pattern in the data. This mode was motivated by a requirement to gather SAR-quality data over a large area within tight data volume limits. One consequence of the ocean-viewing requirements was that VV[‡] emerged as the favored polarization, since vertically polarized oceanic backscatter tends to be larger at C band at steep incidence[§] than horizontally polarized oceanic backscatter. ERS-1 and -2 also carried radar altimeters (Section 18.3). The ESA series of satellites use midday sun-synchronous orbits because their payloads include optical sensors. The resulting half-orbit eclipse contributes to their per-orbit SAR operational limit of ten minutes.

J-ERS-1. The SAR aboard the Japanese Earth Resources Satellite¹⁴ (J-ERS-1) was similar to Seasat, being at L band, with an H-polarized 11.9 m by 2.4 m antenna. Its 38° incident angle,^{*} which is larger than that of Seasat, was enabled by its lower altitude and larger antenna aperture. Its 1.1 kW peak power was comparable to that of Seasat. One consequence of the larger antenna vertical dimension is the 75-km swath, which is narrower than that of Seasat. J-ERS-1 was crippled by antenna and connector problems, so that its sensitivity (noise-equivalent sigma-zero NEqσ⁰) was only –14 dB, 6 dB shy of its –20 dB design. As a result, J-ERS-1 image products were far noisier than those of Seasat, whose sensitivity was –23 dB. In spite of that handicap, however, J-ERS-1 data (at 23-cm wavelength) provided the first synoptic coverage of the tropical forests of Brazil and neighboring countries. These data established an early “gold standard” for tropical forest surveys, since L band is so much better suited to this application than shorter wavelengths. J-ERS-1 had 18-m resolution at 3 looks, about 50% “better” than Seasat, based on comparison of their respective SAR image quality factors (Section 18.4). J-ERS-1 operated for eight years, considerably longer than its two-year design life.

RADARSAT-1 Shown in Figure 18.2, RADARSAT-1 marked a major milestone in space-based SAR. It was the first system to offer the user a choice of resolutions, incident angles, and swath widths.¹⁷ The evolution of these characteristics merits a brief review. The Canadian requirements spanned a variety of applications, from oceanic surveillance (vessels and oil platforms as well as sea state), land- and sea-ice, agriculture, and forests, among many others. The sea-ice application had high priority, which drove the choice of polarization. Horizontal was chosen, because that

[‡] It is common in radar remote sensing that their polarizations are abbreviated as an alphabetic pair, in this case indicating vertical polarization on both transmit and receive.

[§] Space-based SARs tend to look toward the surface at angles that are much closer to vertical than do airborne SARs. The most commonly used terminology is incidence (the angle at the illuminated surface between the local vertical and the incoming illumination). The angle of incidence is the complement of the grazing angle, the customary nomenclature for airborne radars. Incidence differs from elevation (the angle at the spacecraft between vertical and the direction from the spacecraft to the scene), where the difference is due to the Earth’s curvature.

* Alert! The Japanese SARs usually specify the look angle as the elevation angle at the spacecraft, although calling that angle “incidence.” Thus, most of the literature cites 35° for J-ERS-1’s incidence, which can lead to confusion if the value of this parameter is important in a given application. The same caveat applies to PALSAR, described in a subsequent paragraph.

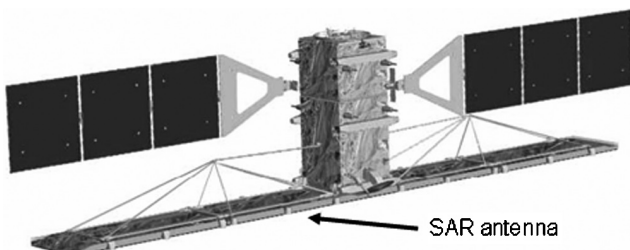


FIGURE 18.2 RADARSAT-2 is outwardly similar to its predecessor. The solar panels are parallel to the along-track axis of the antenna, indicative of a dawn-dusk sun-synchronous orbit. (*Courtesy of the Canadian Space Agency*)

offered an advantage when attempting to distinguish new ice from calm sea at C band and moderate incidence. The applications diversity implied a span of preferred incidence from $\sim 20^\circ$ to more than 50° . In response, the antenna was required to steer its beam in elevation, which evolved into seven different standard elevation beam patterns, electronically steered and shaped. As might be expected, no applications theme would accept degraded resolution. To satisfy that demand, the radar design adopted three bandwidths, so that the nominal ground-range resolution would be maintained at ~ 25 m over all baseline incident angles. As a corollary, the wider bandwidth at shallower incidence would result in finer range resolution. The antenna design was based on horizontal runs of 32 waveguides, each center-fed. Ferrite phase-shifters, one for each waveguide, controlled the transmit and receive beam shape and boresight in elevation. The electronic beam-selection enabled RADARSAT-1 to incorporate ScanSAR.[†] Thus, the resolution options for RADARSAT-1 range from 8 m by 8 m (single look) 45-km swaths (fine mode), to 100 m by 100 m (8 looks), 510 km swaths (ScanSAR Wide). Incidence ranges from 10° to 60° , including the extended modes. There are seven standard modes, each having its own elevation beam; these modes have nominally 25 m by 28 m (4 looks), 100-km swaths. The $\text{NEq}\sigma^0$ is -20 dB or better and mode-dependent.

By the end of 2006, RADARSAT-1 had completed its 11th year, logging more than 60,000 orbits and collecting enough data to map the entire surface of the Earth an equivalent of 130 times. The Canadian Ice Service relies on RADARSAT-1 data for its routine operations, which require more than 3000 frames of data per year. Since the SAR is the only RADARSAT-1 payload instrument, a sun-synchronous, dawn-dusk orbit was chosen to maximize illumination of the solar panels, which allows 20 minutes of SAR operation per orbit. RADARSAT-1 looks to the right side of the orbit plane, which gives it access to the Canadian Arctic up to the North Pole. Twice during its mission, the spacecraft was yawed 180° for several weeks, which enabled full coverage of Antarctica. The resulting data were merged to yield the first high-resolution imagery of the whole continent,¹⁸ and over several regions, repeat-pass coverage supported interferometric SAR measurement of Antarctic glacial flow rates. RADARSAT-2 is an enhanced version¹⁹ of RADARSAT-1. Table 18.3 charts a summary of its many modes.²⁰

[†] Discussed later in this section.

TABLE 18.3 Rsat-2 Modes

Mode	Width W	Access	Resolution	Looks	$1/Q_{SAR}$	$W Q_{SAR}$
<i>Selective polarization</i>						
Standard	km	km	$m, Rg \times Az$	$Rg \times Az$		
Wide	100	250–750	25×26	1×4	162	0.62
Fine	150	250–650	30×26	1×4	195	0.77
ScanSAR Wide	50	525–750	8×8	1×1	64	0.78
ScanSAR Narrow	500	250–750	100×100	4×2	1250	0.40
ScanSAR Narrow	300	250–720	50×50	2×2	625	0.48
<i>Single polarization</i>						
Low incidence	170	125–300	40×26	1×4	260	0.65
High incidence	70	750–1000	18×26	1×4	117	0.60
<i>Polarimetry</i>						
Standard QuadPol	25	250–600	25×8	1×4	50	0.50
Fine QuadPol	25	400–600	9×8	1×1	72	0.35
<i>Selective Single Pol</i>						
Multi-look Fine	50	400–750	8×8	2×2	64	3.12
Ultra-Fine	20	400–550	3×3	1×1	9	2.2
<i>Experimental</i>						
MODEX (GMTI)						
Very High Resolution				3×1	1×1	

ENVISAT. The advanced SAR²¹ (ASAR) aboard ESA's Envisat takes RADARSAT-1's versatility one step further, with the addition of two polarizations, H and V, on either transmit or receive. Its 10 m by 1.3 m active array antenna comprises 320 transmit/receive modules. In other regards, its modes reflect the basic RADARSAT-1 design (due, in large part, to the participation by key radar specialists from Canada—a member of ESA's Earth Observation Program Board—on the ASAR conceptual design team). The transmit and receive polarizations are independent of each other, so that at full resolution, the polarization choices are HH, VV, or HV. Note that this dual-polarization mode is actually *alternating-polarization*, in which the polarization states are switched between transmissions or receptions, but the pulse-repetition frequency is not increased. Such a “dual-polarized” pair, by definition, cannot be mutually coherent since it corresponds to interleaved samples of the backscatter, time-multiplexed at less than the Nyquist rate. As a consequence, the phase difference between complex samples at each pixel is not available. The ASAR alternating polarization mode provides dual-polarized images that are similar to those that have been available from many airborne systems for decades, although not available from an SBR (except for SIR-B and SIR-C) until ENVISAT.

PALSAR. In contrast to the incoherent polarimetric options of ASAR, the Phased-Array L-band Synthetic Aperture Radar (PALSAR) aboard Japan's ALOS[‡] (launched in January 2006) includes full quadrature[§] polarimetry.^{22,23} The PALSAR modes include standard single-polarization mapping modes, a ScanSAR mode, a variety of dual- and quadrature-polarized modes, and experimental modes, including SpotSAR. Early mission calibration and validation studies verified that the radar is performing as intended. More on PALSAR appears later in this section.

[‡] Advanced Land Observation Satellite, JAXA, Japan.

[§] Discussed later in this section.

JianBing-5. Known alternatively as Remote Sensing Satellite-1, Jianbing-5 is China's first synthetic aperture radar mission. The spacecraft mass is 2700 kg, launched into a sun-synchronous orbit at ~600 km altitude. Mission objectives include polarimetric diversity and interferometry. The two baseline multi-look resolutions are 3 m (40-km swath) and 20 m (100-km swath), over a variety of incident angles. Its antenna is an active phased array.

TerraSAR-X. TerraSAR-X is the first civilian dedicated space-based SAR at X band. Its 4.8 m by 0.8 m antenna is a two-dimensional active array of 384 T/R modules. It has a variety of modes, from ScanSAR (15-m resolution over 100-km swaths) to SpotSAR (1-m resolution over a 5-km by 10-km image frame). Its strip mapping mode is baselined at 3-m resolution across 30-km swaths. The array is partitioned in the along-track direction, which can be exercised in a two-aperture along-track interferometric mode for GMTI experiments, among other applications. Full quadrature polarization is one of the mode options. The only payload instrument is the radar, so the spacecraft is designed for a sun-synchronous dawn-dusk orbit, 11-day repeat. Several years after the launch of TerraSAR-X, it will be joined by a companion, Tandem-X, which is meant to be a functional copy.²⁴ These two will co-orbit as a closely coordinated pair to support a variety of bistatic and interferometric applications.

Other Space-based SARs. Space-based SAR continues to undergo considerable expansion on an international front. This section provides an overview of programs known (at the time of publication of this Handbook) to have progressed through Phase A, which is evidence of funding that is sufficiently serious that most are likely to culminate in the launch and operation of a flight system. The architecture of these emerging systems is dominated by one of two antenna paradigms: active two-dimensional phased arrays or reflectors. Most missions are multimode in resolution (hence swath and coverage), and polarimetry (ranging from incoherent dual-polarization to full-quadrature polarimetry). At least four of these initiatives imply several satellites, either in constellation or in series. All together, something in excess of 20 new SARs are being launched in the first decade of the 21st century, from at least eight different countries. Highlights of several of these systems are summarized in the following paragraphs.

COSMO-SkyMed. Italy has a series of four COSMO-SkyMed X-band SAR satellites. The COSMO SARs have multipolarization active phased-array antennas that support a variety of modes including 1-m SpotSAR, strip map, ScanSAR, and 500-km wide swath. The COSMO bus is based on the design built and flight-proven for Canada's RADARSAT-2.

TecSAR. The first space-based SAR from Israel, TecSAR is a featured element of their national satellite technology development program.²⁵ Launched by India, TecSAR's nominal strip-map mode is multi-look 3-m resolution at X band. Major additional objectives include large area coverage as well as high resolution, which imply ScanSAR and SpotSAR modes, respectively. The 1-m SpotSAR resolution constrains the design, one consequence of which is the symmetrical body-mounted 3-m diameter umbrella-style mesh reflector (0.5 kg) driven by one of ten feed horns slightly offset from the focal point. This unity-aspect ratio antenna is a notable departure from the rectangular antennas so typical of most space-based SAR precedents.

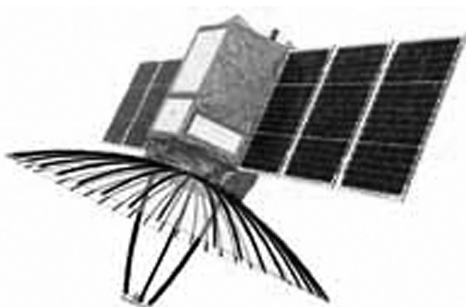


FIGURE 18.3 TecSAR features a symmetrical reflector antenna, in contrast to the classic high aspect-ratio “billboard” style pioneered by Seasat. (*Courtesy of IAI, Israel*)

ScanSAR coverage (8-m resolution, 40-km swath, to 20-m resolution, 100-km swath, incidence-dependent) is executed by sequential selection of the appropriate feeds. The feed horns are H- or V-polarized, so that polarimetric diversity is also supported by this arrangement. Mission design includes spacecraft steering to support squinted aspects relative to the reference side-looking orthogonal viewing. The high-power stage is comprised of ten channeled TWTAs,* eight of which are required in combination, leaving two as redundant backup. The radar mass is 100 kg (including the reflector and feeds); satellite dry mass including the radar is ~300 kg, which at the time set the standard as the smallest SAR satellite in Earth orbit. The power subsystem delivers up to 1.6 kW during imaging operations. The spacecraft orbit is 143° inclination, ~550 km altitude, 36-day repeat period. Since this is not a sun-synchronous orbit and since the antenna pattern (to first order) is symmetric, the spacecraft may be rotated about the radar’s line-of-sight to help sustain near-full illumination of the two solar panel arrays in all sun-orbit plane configurations. Radar data are recorded in a 256 Gbit solid-state unit following 6-to-3 block-floating-point quantization. Spacecraft design life is five years.

HJ-1-C. HJ-1-C is the first of five SAR satellites in China’s small satellite program²⁴ announced in 2002 for environment and disaster monitoring. The architecture of these systems is closely parallel to Russia’s *Kondor-E* series, since they are both outgrowths of a bilateral development program based on the architecture of the Priroda S band radar. The HJ-1-C’s antenna is a reflector that has an effective aperture of 6 m by 2.8 m following deployment. In strip-map mode, the HJ-1-C has a multi-look 5-m resolution over a 40-km swath, and 20-m resolution in ScanSAR mode at 100-km swath width. SpotSAR mode is supported by controlled yaw maneuvers of the spacecraft. All of the spacecraft in the series (five radars and six optical systems) use sun-synchronous orbits at ~500 km altitude. The radar’s mass is ~200 kg.

SAR-Lupe. Germany has five identical X-band satellites, distributed in three 500-km high orbits, inclined at about 80°. The aspect ratio of their 3.3 m by 2.7 m

* Traveling-wave tube amplifier. See Chapter 10 for more discussion.

antennas suggests that the dominant objective is fine resolution, which necessitates a relatively narrow range swath. Published specifications note that the intended resolution in the slip-SAR[†] mode is 0.12 m over a 5 km by 5 km image frame. These innovative SBRs are relatively small, at least by Earth-observing satellite SAR standards. Their 770 kg mass (total dry mass of the spacecraft and the radar) is less than the mass of RADARSAT-2's antenna! The SAR-Lupe design also is cost-conscious, based on rigid (nondeployed) reflector antennas ("borrowed" from a commercial communications satellite production line) that are inherently more efficient and less massive than an active array. The radar electronics are directly descended from a commercial product line.

RISAT. The Radar Imaging Satellite, or RISAT, is India's first space-based SAR,²⁷ following extensive programs in optical remote sensing satellites and airborne imaging radar development. RISAT's deployable antenna (6 m by 2 m) is an active phased array comprised of 288 C-band (5.35 Ghz) TR modules, each capable of 10 W peak power. The average output power (200 W) requires an average input dc power of 3.1 kW. Each TR module is connected to separate distribution networks feeding H- and V-polarized elements, which support polarization diversity as well as elevation beam steering. There are two parallel receive channels (dedicated to the H- and V-polarized antenna elements). RISAT has five modes, each of which may operate at a variety of incident angles. The modes are: fine-resolution strip-map-1 (3-m resolution, 30-km swath, dual-polarization); fine-resolution strip-map-2 (12 m at 30 km, quadrature-polarization); medium resolution ScanSAR (25 m at 120 km, dual-polarization); coarse resolution ScanSAR (50 m at 240 km, dual-polarization); and high-resolution SpotSAR (better than 2 m, 10-km square image frame, dual-polarization). The SpotSAR mode requires yaw/pitch steering of the spacecraft to $\pm 13^\circ$. Coverage to either side of the ground track requires a roll maneuver of the spacecraft to direct the antenna pattern to the opposite side of nadir, an approach that is similar to that of RADARSAT-2. The variety of resolutions is supported by four bandwidths (225 MHz, 75 MHz, 37.5 MHz, and 18.75 MHz) through a programmable digital chirp generator. The received data are downconverted to baseband, digitized to 8 bits (I and Q), and quantized (by block-floating point means) to fewer bits (6 to 2), at the user's option within mode-dependent limits. All subsystems (save for the antenna) are dual-redundant. Nominal PRF is $3250 \text{ Hz} \pm 450 \text{ Hz}$. Data rates span 142 Mbits/s to 1478 Mbits/s, depending on mode. The on-orbit mass of the spacecraft will be $\sim 1750 \text{ kg}$, of which the SAR payload (including the antenna) claims $\sim 950 \text{ kg}$. Onboard data storage capacity is 240 Gbits; downlink maximum data rate is 640 Mbits/s (X band, dual circularly polarized). The RISAT orbit is sun-synchronous, dawn-dusk, at $\sim 609 \text{ km}$ altitude, and 13-day revisit period.

MAPSAR. The Multi-Application Purpose SAR²⁸ is a joint Brazilian-German enterprise aimed primarily at assessing and monitoring Brazil's natural resources. After several years of trade studies, L band was selected (1.3 Ghz). The radar is built around a near-symmetrical reflector (7.5 m by 5 m) with ten feeds, offset from the focal point so that the beam can be electronically scanned in elevation. Spatial resolution and swath span 3 m to 20 m, and 20 km to 55 km, respectively, mode-dependent.

[†] Slip-SAR is a modified ScanSAR mode, in which the antenna pattern is dragged along the surface at a slower rate than in the conventional strip-map mode. The result is larger doppler bandwidth, hence enhanced azimuth resolution, and also a wider imaged area than a pure SpotSAR can support.

The high-resolution specification results from an external constraint, the maximum 85 MHz bandwidth stipulated by international spectral allocation agreements. There is provision for all polarimetric configurations. The sun-synchronous orbit will be controlled to assure reliable 37-day revisit baselines to support interferometry. Nominal instrument mass is 280 kg.

PALSAR. Although based on JERS-1 heritage, PALSAR²⁹ is an excellent early example of multimode space-based SARs. PALSAR's 132 modes (Figure 18.4) include standard single-polarization mapping, ScanSAR, a variety of dual- and quadrature-polarized modes,[‡] and experimental or demonstration modes including SpotSAR. The L band (23 cm) baseline frequency (1270 MHz) has two bandwidths, 28 MHz (fine-beam single-polarization mode), and 14 MHz (dual-, quad-pol, and ScanSAR modes). The span of mid-swath incident angles is (7.9°–60°). (Note that the Japanese usually cite these angles as “off-nadir” (9.9°–50.8°), which refers to their elevation with respect to vertical in spacecraft coordinates, rather than their intersection relative to a local vertical at the Earth’s mean oblate spheroidal surface.)

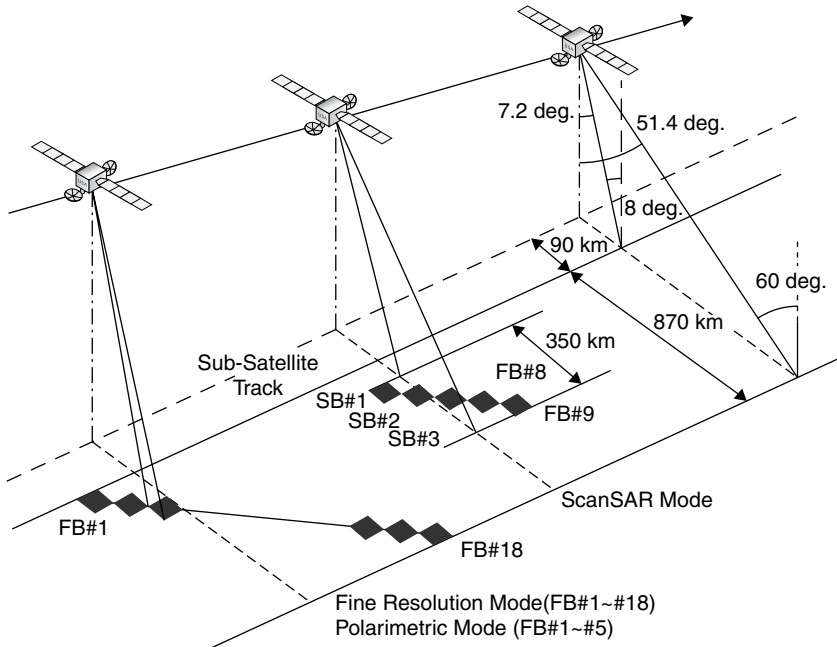


FIGURE 18.4 Overview of PALSAR’s viewing geometries. Each of these beam positions supports a variety of polarization combinations, leading to a very large number of available modes. The solar panel is orthogonal to the orbit plane, indicative of a midday sun-synchronous orbit. (*Diagram courtesy of JAXA, Japan*)

[‡] The several forms of polarimetric diversity common in remote sensing systems are reviewed later in this section.

Modern space-based SARs owe their large mode variety to active electronically steered antenna arrays. PALSAR's antenna consists of 80 solid-state T/R modules distributed on four panels whose deployed dimensions are 3.1 m by 8.9 m, vertical and horizontal, respectively. Spacecraft velocity and antenna length dictate a lower bound on pulse repetition frequency, which for PALSAR spans 1.5 kHz–2.5 kHz, depending on mode. Peak transmitted power is ~ 2 kW, twice that of the Seasat SAR. The resulting sensitivity (noise-equivalent sigma-zero) is very good, -30 dB or better for most modes. PALSAR's host ALOS spacecraft is yaw-steered to maintain azimuth antenna boresight pointing at zero doppler, which increases the likelihood of pass-to-pass interferometric coherence and simplifies (somewhat) SAR image formation processing. The nominal data rate in most modes is 240 Mbit/s, which is downlinked via Japan's Data Relay Test Satellite (DRTS). The ScanSAR mode requires only half that rate, 120 Mbit/s, which can be downlinked directly to ground stations. ALOS has an onboard 96 Gbyte solid-state recorder to buffer data output from the radar, as well as from the rest of the payload.

PALSAR's voluminous variety of modes is a curse as well as a blessing. Mission management must cope with data collection in each of these modes, as well as phasing the resulting data burden to share the communications link with the two other high data-rate instruments in the ALOS payload. The standard policy for the early years of PALSAR's on-orbit scheduling is to focus on six "default" modes—four "operational" and two "semi-operational." The resulting terms are (1) fixed "standard" off-nadir angle of 41.5° for a great majority of the data takes; (2) polarization options to be single-pol HH and dual-pol HH+HV; (3) quad-pol at 21.5° (off-nadir) for R&D demonstrations over preselected "supersites"; and (4) five-beam ScanSAR in HH polarization. In addition, the following constraints apply: only one mode is exercised during one 46-day repeat cycle; preferred operations are during the hours of darkness in the ascending passes for most modes, excepting lower data-rate ScanSAR data takes during descending passes (in coordination with the optical sensors) and also excepting extraordinary InSAR and marine applications at nonstandard incidence; and recurrent repeat-pass coverage of selected sites in groups of eight or more 46-day cycles in support of InSAR objectives.

Space-based SAR Design Issues. The options for space-based SAR design^{30,31} are more limited than for airborne systems, due primarily to the constraints imposed by viable orbits, including especially sensor velocity, radar range (R), and system cost. The following paragraphs review the major themes.

PRF Constraints. The rules that govern the pulse repetition frequency (PRF) of a space-based SAR are the same as those applicable to airborne systems, although they play out rather differently. The fundamental requirement is that the PRF f_p be sufficiently high to sample unambiguously the doppler spectrum of width B_{Dop} , and also sufficiently low so that there is time between transmissions to receive the data backscattered from the intended swath of slant range (time-domain) width T_R . Thus

$$B_{\text{Dop}} < f_p < 1 / T_R \quad (18.2)$$

In practice, sufficient margin must be included in both the upper and lower limits to account for the length of the transmitted pulse, and for the fact that neither the doppler spectrum nor the antenna's elevation pattern have sharp cutoffs.

The lower bound often is recast as

$$B_{\text{Dop}} = \frac{2\beta V_{\text{SC}}}{\lambda} = \frac{2V_{\text{SC}}}{D_{\text{Az}}} < f_p \quad (18.3)$$

which states that the PRF must be sufficiently high such that there are two transmissions per antenna aperture length D_{Az} as the radar moves along its trajectory. (Here V_{SC} is spacecraft velocity along its orbit, β is the width[§] of the azimuth antenna pattern, and λ is the radar wavelength.) This form is intuitively satisfying, since the single-look azimuth resolution is approximately one-half of the antenna's along-track width, hence this inequality requires that each resolved along-track range line must be sampled at least once. Usually the PRF lower bound is set so that there is a margin of 25% or more with respect to this constraint.

In an airborne SAR, the PRF constraint is derived to satisfy the doppler bandwidth, from which follows the maximum range that the radar can operate without introducing ambiguities. However, by default, the minimum range for a space-based SAR is its orbital altitude, usually 600 km or higher. The typical slant range to the intended scene may be 800 km and more. Thus, the upper bound on the PRF should not be set by the range to the scene, but rather by the range width of the area to be imaged. As a consequence, the resulting high PRF will generate a sequence of pulses at any moment that are distributed between the radar and the scene. The space between pulses must be larger than the intended swath width. For example, in certain modes RADARSAT-1 generates seven pulses “in flight” simultaneously. At the beginning of such a data collection, backscatter from the intended scene would arrive only after the seventh pulse had been transmitted.

In many airborne systems, the PRF is chosen to be rather higher than the limit imposed by the range to the intended target space. In such cases, the extra PRF contributes to improved SNR, but at the cost of increased average data rate. Data rate can be decreased by “pre-summing”—coherently adding n adjacent returns. The consequence, of course, is that the effective PRF is reduced by the same factor n . This practice is seldom acceptable for space-borne SARs, because it leads to azimuth ambiguities unless the doppler spectrum is limited prior to PRF reduction.

Ambiguities. The PRF generates a two-dimensionally sampled space when the data are decomposed into “slow time” (in the azimuth direction) and “fast time” (in the range direction). In azimuth, the PRF creates aliased versions of the data illuminated by the main beam of the antenna. The spectra of these aliases are located at multiples of the PRF to either side of the doppler centroid of the main beam. Of course, when sampled they are folded back into the Nyquist passband. These aliases are azimuth ambiguities, which are suppressed—hence not visible—in a well-designed system supported by a well-tuned processor. When they do appear, azimuth ambiguities are relatively easy to identify (Figure 18.5) because they are weaker (ghost) duplicates of image features that were collected through the main beam and, therefore, at earlier or later positions along the image strip. The azimuth shift of the ambiguities relative to the central image is an integral multiple of $\Delta X = R\lambda f_p / (2V_{\text{SC}})$, which is the spatial

[§] For a uniformly illuminated aperture, the -3 dB beamwidth is $\beta = 0.88 \lambda / D_{\text{Az}}$. It is customary for analysis of SAR systems to approximate this expression by $\beta \sim \lambda / D_{\text{Az}}$ and to interpret β as the width of the rectangle that has the same peak value and area as the antenna pattern.

offset corresponding to the PRF. Azimuth ambiguities, especially from point targets, have the same doppler FM rate as scatterers within the main beam, and so their focus is preserved through the processor.

In the range direction, one of the consequences of having many pulses in flight at once is that there are echoes from several different ranges that arrive back at the radar at the same relative delay within the range gate as the reflections from the intended swath. If these extra echoes are sufficiently strong, the resulting image artifacts are range ambiguities. Range ambiguities are not as easy to identify as azimuth ambiguities, because they arise from ranges outside of the nominal swath, hence not otherwise imaged. Range ambiguities by definition arise from ranges that are different from those for which the processor is set, so that range-ambiguous point targets tend to be defocused.

The principal means of suppressing ambiguities is to confine the main beam of the antenna so that the potential sources of azimuth or range ambiguities are not illuminated, or at least are illuminated only very weakly. This requirement imposes a minimum area constraint on the SAR's antenna. The lower and upper bound PRF constraints of B_{Dop} and $1/T_R$ lead to

$$D_{\text{El}} D_{\text{Az}} > 4RV_{\text{SC}}(\lambda/c) \tan \theta_{\text{Inc}} \quad (18.4)$$

where the antenna area is the product of its length D_{Az} and height D_{El} , and θ_{Inc} is the mean incident angle in the imaged swath. The range-velocity product in this expression is determined by the parameters peculiar to the particular planet (or moon) about which the SAR is to operate (Table 18.1). As a consequence, an antenna of area 1 m^2 at the Moon would have be 10 m^2 for the same radar at Mars and nearly 40 m^2 for operation in Earth orbit.

It always is tempting to push this constraint, since most space-based SARs use as much of the ambiguity-free space as can be tolerated. In practice, the antenna area usually is chosen to be at least a factor of two larger than this minimum would suggest. Ambiguities are proportional to the strength of the offending backscatter, and as such, they contribute to the multiplicative noise* ratio (MNR) of the system. Antenna sidelobes and ambiguities are further suppressed by appropriate weighting in the processor. The trade-off is lower MNR, at the expense of broader impulse response width (IRW). Typical designs provide ~20% excess range and doppler bandwidth relative to those implied by the required range and azimuth resolutions to accommodate such weighting.

Nadir Return. A potentially troublesome range ambiguity arises from the surface directly below the spacecraft. This nadir return is always relatively strong, particularly if there are specular backscattering components. Since any realistic antenna pattern has a non-zero sidelobe directed toward nadir, the resulting reflection could appear in the image. The main strategy is to avoid the ambiguity by choosing the PRF so that the nadir return arrives at the same time that the radar is transmitting. This timing places a further constraint on the pulse repetition frequency. It turns out that the nadir return may not be avoidable if other constraints override the available PRF options. This occurs, for example, if the driving requirement is ScanSAR, which has its own set of constraints on PRF.

* Multiplicative noise, a standard specification in synthetic aperture radar, includes unwanted contributions such as ambiguities and quantization noise that are proportional to the strength of the received signal.

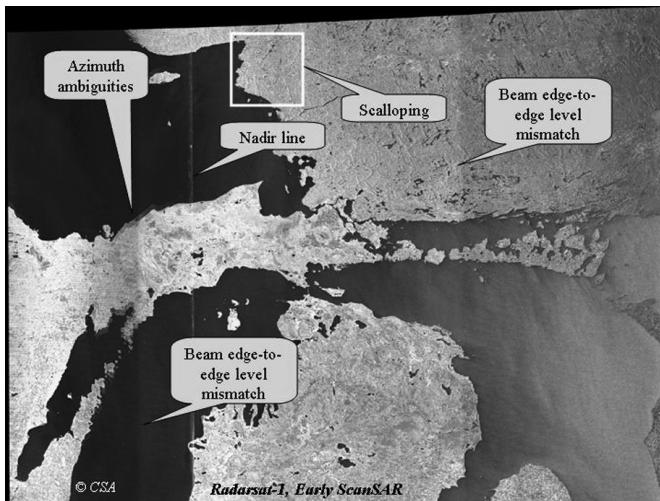


FIGURE 18.5 Example of artifacts as they appeared in early RADARSAT-1 four sub-swath ScanSAR imagery. The direction of flight is vertical in this presentation, near-edge range at the left of the frame. (*Courtesy of the Canadian Space Agency and the Canada Centre for Remote Sensing*)

Antennas and Transmitters. Antennas for the pioneering space-based SAR systems were exclusively passive, such as the L-band patch array on Seasat or the slotted waveguide arrays used on ERS-1/2 and Almaz. The first exception to this rule was RADARSAT-1, designed around an array of 32 horizontal slotted waveguides, each of which was center-fed through a phase shifter so that the elevation beam pattern could be selected and shaped electronically. More ambitious (read “massive and expensive”) systems tend to use two-dimensionally active electronic scanned arrays (ESAs). These are populated by transmit/receive (T/R) modules, often incorporating two polarizations (H and V). Examples include RADARSAT-2, ENVISAT’s ASAR, PALSAR, COSMO, TerraSAR-X, and RISAT. It is argued that active arrays set the stage for “graceful failure” since the loss of a few T/R elements would have little effect on the net performance of the system. In parallel, an alternative SAR antenna paradigm stresses simplicity and lower mass (and lower cost) over two-dimensional electronic beam steering. These are reflectors, of which China’s HJ-1-C, Germany’s SAR-Lupe, Israel’s TecSAR, and Brazil’s MapSAR are good examples. If a reflector is driven by multiple feeds, then one may still effect beam steering, although with rather less beam shape variety and control than through an ESA.

Space-based radar transmitters naturally fall into two classes, intimately coupled with the antenna’s architecture. If the antenna is active, then the transmitter (as well as the front end of the receiver) is distributed over the array. In this case, several hundred T/R elements, of a few watts peak power each, add up to many hundreds of peak radiated power. Phase control of the elements is a critical parameter, usually requiring adaptive temperature compensation to assure coherency of the radiated wavefront. The alternative is almost always limited to traveling wave tube amplifiers (TWTAs), although recent developments in high-power solid-state devices is influencing SBR SAR design. Radars built around TWTAs have established impressive longevity records, witness RADARSAT-1 and ERS-2, both of which remained in operation for more than ten years.

Data Rate. Data rate is proportional to the product of pulse repetition frequency f_p , the number of range samples N_R (which is proportional to slant-range swath, plus the uncompressed pulse length, and inversely proportional to range resolution), the number of quantization bits N_S retained in each sample of the data, and a factor of 2 that accounts for the in-phase (I) and quadrature (Q) components since both the amplitude and the phase of the signal stream are required. Once resolution and swath are established, the number of bits per sample is the only parameter open to choice. Excellent results may be obtained for N_S , as small as 2 bits (per I and per Q) by adapting the quantization thresholds to the mean signal level. (Refer to Section 18.4 for more on this topic.) Quantization noise, which is larger for fewer bits, is proportional to signal strength; hence it is a factor in the MNR budget. Exacting applications such as interferometry are better served by more bits per sample, subject to the rate and volume limits of the data handling subsystems.

Processing. Although similar in principle to airborne systems, processing for space-based SARs differs in several key regards. The highlights are reviewed here. For more complete coverage, see the standard references.^{30,32} A simplified introduction to the key parameters may be helpful.³³

The natural starting point is the range equation, from which several properties emerge that are unique to the spherical geometry of radars in orbit. In the narrow-beam side-looking case, and neglecting the effects of Earth rotation, the radar-to-target range variation generates a phase time-history over a synthetic aperture length of T seconds from a point reflector at minimum slant range R_0

$$\Theta(t) = -\frac{4\pi}{\lambda} \left(R_0 + V_{\text{SC}} V_{\text{Beam}} \frac{t^2}{2R_0} \right) \quad (18.5)$$

where V_{Beam} is the velocity on the surface of the illuminating footprint of the azimuth antenna pattern. The time derivative of the phase yields the scatterer's doppler history

$$f_D(t) = -\frac{2}{\lambda} \frac{V_{\text{SC}} V_{\text{Beam}}}{R_0} t \quad (18.6)$$

in which the FM rate is proportional to the effective velocity $V_{\text{Eff}} = (V_{\text{SC}} V_{\text{Beam}})^{1/2}$. This is in contrast to the airborne case for which the FM rate of the azimuth doppler modulation is proportional to the square of the aircraft velocity. Why the difference? Rather than a straight line, which is the baseline situation for an airborne system, the synthetic aperture of a space-borne SAR is formed along an arc. This imposes a small but significant increase in the effective length of the synthetic aperture and also modifies the FM rate. As a consequence, the nominal single-look azimuth resolution from a space-based SAR is $r_{\text{Az}} = (V_{\text{Beam}} / V_{\text{SC}}) D_{\text{Az}} / 2$ rather than the famous "one half of the aperture length" of airborne SARs. Note that V_{Beam} is always smaller than the spacecraft velocity, and decreases with increasing spacecraft altitude and incident angle. Alert: In certain SAR processing literature, the effective velocity for the orbital case is denoted "radar velocity," a rather misleading and inappropriate term.

The average data rate from space-based SARs in Earth orbit is on the order of 100 Mb/s, (megabits per second) with higher resolution and polarization diversity systems generating several times that. The drivers are the spacecraft velocity (~7.5 km/s), range resolution, and swath width. Many users would like to have immediate access to processed data, which leads to the question of onboard processing. Space-based

SAR systems as a rule do not implement image formation onboard for several reasons, including high data rates. Processing from raw SAR data to imagery increases data volume substantially, thus increasing the downlink data transfer burden. Perhaps more persuasive, once processed into detected images, the options are limited for specialized application-specific post processing.

In contrast to airborne systems, the dynamics of most spacecraft are such that no motion compensation is required for space-based SARs (unless extremely fine resolution is to be generated). However, determining the doppler centroid of the azimuth spectrum with respect to zero doppler emerges as a dominant issue. If the azimuth antenna boresight is perfectly orthogonal to the inertial orbit plane, the Earth's rotation imposes a doppler shift onto the received data.³⁰ From low Earth orbit (LEO), the magnitude of this shift is on the order of 3° , and (to first order) varies sinusoidally with latitude, with maximum magnitude at the equator, and with zero at the extreme N and S latitudes. The effect can be offset by yaw-steering the spacecraft so that the antenna's boresight is always directed toward zero doppler. This orients the vertical plane of the azimuth boresight to be orthogonal to the nadir track on the surface, rather than to the orbit plane. Whereas SAR data from both arrangements can be processed into satisfactory imagery, more demanding applications such as radar interferometry are better served by yaw-steered systems. Yaw steering imposes negligible additional demands on the spacecraft attitude control system, since it requires maneuvers of only $\pm 3^\circ$ over each orbital period. Note that a SAR looks down as well as to the side, so that vertical velocity components in the satellite's orbit also lead to doppler shifts in the data. In principle, a doppler shift from a vertical velocity component also could be offset by attitude adjustments of the spacecraft, although this strategy is not in general practice. Doppler centroid estimation is a central function implemented in all processing algorithms for SBR SAR data.

Data Products. The notional data product from a space-based SAR is imagery, usually visualized as a black-and-white mapping of the scene illuminated by the radar. By definition, the digital numbers at each pixel in such an image array are real and non-negative. In theory, these numbers correspond to the magnitude-squared of the focused and detected backscattered field. In practice, most image products (such as those from the European Space Agency's SARs) use magnitude, because the resulting imagery has an acceptable appearance and the size of the data file is smaller than if in $|\text{magnitude}|^2$. If several data sets over the same scene are combined, often these are individually color coded, leading to multicolor image products. Each constituent data set might be from a different polarization, wavelength, or observation time.

It is common parlance to refer to imagery as mappings of the normalized backscatter power $\sigma^0(x,y)$. Alert: In fact, this is seldom *if ever* true. Backscattered power is proportional to $|\text{magnitude}|^2$, not magnitude. Hence, the user must assure that the data are indeed magnitude-squared before applying tools, such as speckle filters, that are designed for σ^0 dimensionality. Second, σ^0 implies that the data are calibrated, not only with respect to the radiometric parameters of the radar and processor, but also with respect to the local incident angle at the pixel location (x,y) . Although data from ERS-1/2 are corrected to account for the mean incidence within the imaged swath, there is no attempt to correct for slopes locally within the swath to the pixel level. An alternative is to denote the (magnitude-squared) digital numbers as β^0 , which indicates simply radar power per pixel.³¹ This has become standard practice with RADARSAT-1 data, for example.

Standard image products usually are “multi-look.” In jargon common in the space-based SAR field, “looks” refer to statistically independent versions of the same scene. When these are added together, the net result is to reduce the speckle noise, while reinforcing the imaged features. Each such look is formed from a spectral band that does not overlap spectra corresponding to the other looks. Thus, for a given bandwidth, increasing the number of looks reduces speckle, but at the cost of compromising resolution. (More on this trade-off may be found in Section 18.4.)

In contrast to conventional post-detection imagery, focused SAR data may be presented as single-look complex (SLC) products. These data retain the full resolution of the radar, and most important, retain the relative phase of the backscattered field. By definition, SLC files are in amplitude and phase, often represented as an array of in-phase (I) and quadrature (Q) signed number pairs, at each pixel. SLC data are required for SAR interferometry, polarimetry, and coherent change detection.

Pushing Ambiguity Limits. The baseline single-look SAR azimuth resolution is proportional to one over the doppler bandwidth generated by the azimuth beamwidth of the side-looking antenna. The corresponding length of the synthetic aperture is equivalent to the along-track spread of the antenna pattern, which, of course, is proportional to range. Let this be the canonical case. Azimuth resolution may be sharpened only by increasing doppler bandwidth, which can be done in one of two ways: increasing the antenna’s beamwidth or increasing the spread of aspect angles within which the antenna illuminates a given portion of the scene. The latter is the basis for Spotlight SAR,[†] in which the antenna is steered to dwell on the intended area as the radar passes, thus creating a wider total doppler bandwidth (and a longer synthetic aperture). The trade-off is that adjacent areas along-track may not be imaged at all. (Increasing azimuth resolution by broadening the antenna pattern, either by reducing the aperture length or spoiling the beam, has the disadvantage of reducing the antenna’s gain, which usually is not desirable for space-based SARs. In addition, the PRF must be larger than the instantaneous doppler bandwidth, thus reducing the allowable unambiguous range swath.)

Going the other direction—smaller doppler bandwidth—leads to more coarse azimuth resolution. The doppler bandwidth of the original signal history from a given backscatterer may be reduced by the simple expedient of generating a shorter synthetic aperture than the canonical case. This logic leads to the “burst mode,” which figures prominently in two forms in space-based SARs. Burst mode along a single imaged swath implies a reduced data rate, which may be necessary to meet the stringent data-rate requirements confronting planetary or lunar missions. Alternatively, the intervals between bursts may be used to illuminate several different range swaths, thus expanding the area that may be imaged unambiguously. This is the principle behind the ScanSAR mode.

Ambiguity Space Trade-offs. It is easy to show that these resolution and coverage options are consistent with the principles that govern range and azimuth ambiguities. The fundamental rule is that the image space (illuminated by the antenna) must be “underspread” if ambiguities are to be avoided.³⁴ The underspread condition is that

$$T_R B_{\text{Dop}} < 1 \quad (18.7)$$

[†] Alternatively known as SpotSAR.

where T_R is the (slant) range swath depth of the antenna pattern and B_{Dop} is the corresponding doppler bandwidth. To first order, the azimuth resolution is given by

$$r_{\text{Az}} = \frac{\beta RN_L}{T_{\text{Az}} B_{\text{Dop}}} \quad (18.8)$$

where β is the azimuth beamwidth, R is slant range, N_L is the number of looks (here assumed to be taken in the azimuth domain), and $(T_{\text{Az}} B_{\text{Dop}})$ is the azimuth time-bandwidth product, comprised of the illumination time of the target, and its doppler bandwidth. Substituting for doppler bandwidth in the underspread condition leads to the constraint

$$\frac{T_R \beta RN_L}{T_{\text{Az}} r_{\text{Az}}} < 1 \quad (18.9)$$

which shows how resolution and target illumination time may be traded against each other while still respecting the fundamental ambiguity constraint. The following four cases are important in practice.

Strip Map. The standard approach is strip mapping, in which the ambiguity-free space is (nearly) filled with the allowable swath, resolution, and number of looks. Of course, (azimuth) resolution can be increased within the allowed space at no loss of swath width if the number of looks is decreased in proportion.

SpotSAR.^{35,36} If (azimuth) resolution is the driving objective, then r_{Az} may be reduced as long as the integration time T_{Az} is increased in proportion. Given that the beamwidth of the antenna is fixed, the integration time can be increased only if the beam is pointed to maintain illumination of the desired target, much as a spotlight from a moving vehicle dwells on an area of interest. The usual consequence of fine resolution in SpotSAR mode is smaller range swath and an azimuth size that is limited above by the width of the antenna's footprint. The required steering rate is relatively slow, typically a few degrees over a few seconds, implemented either by moving the antenna beam or by yaw-steering the spacecraft. Note that the radar's PRF needs to be only above the Nyquist limit set by the antenna beamwidth, not by the total span of doppler frequencies collected. Range resolution is improved in the usual way, by increasing the radar's bandwidth, for which the Stretch technique is often helpful. A variation of this mode (SlipSAR) is to drag the antenna footprint rather than to stare at one area, thus trading poorer azimuth resolution than a pure SpotSAR would deliver to gain increased azimuthal coverage.

How far can this be pushed? Under the assumption that a target's scattering is coherent over a full 180° sector, it can be shown³¹ that the ultimate azimuth resolution is $\lambda/4$. By the way, such phenomenal results have been approached in the field of seismology.

*Burst Mode.*³⁷ If average data rate is the driving consideration, then the integration time T_{Az} may be reduced below the canonical limit set by the azimuth antenna beamwidth. This is accomplished by turning off the transmitter after enough pulses have been collected to satisfy the azimuth resolution requirement. Each such burst has an instantaneous doppler corresponding to the antenna beamwidth (which determines the Nyquist PRF limit), but a shorter synthetic aperture length. Burst mode is standard

operating procedure for planetary or lunar radars, for which high image resolution is not required and the spacecraft-to-Earth data link is severely limited. While in burst mode, it is customary to use each burst as a single-look data take, setting the burst repetition frequency so that the desired number of looks is collected during the synthetic aperture length of the azimuth beam pattern. The challenge is to calibrate the antenna pattern such that the framelets from all bursts may be combined to assemble a continuous image along track. Mismatches appear as “scalloping”—systematic brightness modulations at boundaries between each of the framelets.

ScanSAR^{38–40} If swath width is the driving requirement, then azimuth resolution can be traded for range coverage. The trick is to multiplex several burst-mode data sets, where each set of bursts corresponds to a different range sub-swath. In this form of burst mode, the transmitter is always “on”; the burst range sub-swath allocation burden falls onto the antenna. ScanSAR requires rapid elevation beam steering, such as through a phased array (e.g., TerraSAR-X), or selection of one among several range-offset feeds facing a reflector (e.g., HJ-1-C). In addition to suppressing scalloping, good ScanSAR imagery requires that the several range sub-swaths be knitted together such that the crossovers between antenna patterns are not evident. RADARSAT-1 was the first mission to implement (then to perfect) operational ScanSAR, which has been adopted as a standard mode on many space-based SARs. Swath widths achieved are as much as five times the nominal strip-map width, which is considerably larger than the conventional ambiguity constraint would allow. Normally, the trade-off in azimuth resolution is balanced with a corresponding compromise in range resolution, leaving excess range bandwidth that may be converted into looks. Starting from a 100-km swath 25-m × 25-m 4-look system, a reasonable ScanSAR mode could be 500-km swath, 100-m × 100-m × 8-looks, with no increase in average data rate or transmitted power.

Note that all of these ambiguity-space trades start with the canonical case. The trade-offs are relative to that starting position. A radar having an inherently small range swath, for example, would require ScanSAR to expand the range swath to a few tens of km, which may still be much larger than the same radar could cover without ambiguities in a strip-map mode.

Multiple Channels: Interferometry and Polarization. Phase comparison between two or more mutually coherent data sets leads to rich new possibilities, especially including interferometry⁴⁵ and polarimetry.⁴¹ This is particularly relevant to space-based SARs, which have been and will continue to be rich sources of quantitative microwave measurements of a wide variety of surface features, enabled by these multichannel capabilities. The following paragraphs provide only a glimpse into these topics; the discussion is meant to whet the appetite of the reader and to provide leads to the voluminous literature.

Interferometry. Interferometry by radar (Figure 18.6) implies measurements that are based on phase differences sensed through two different observations of the same phenomena.^{42–45} Phase differences arise from microwave-scale changes that are due either to differential viewing aspect or to elements of motion in the scene. In general terms, the sensitivity of phase measurements depends to first order on (1) the radar’s wavelength, (2) the spatial or temporal baseline of the contributing data sets, and (3) the scale of spatial or temporal differential signals. The interferometric baseline increases with range and with platform velocity. It follows that for space-based radars,

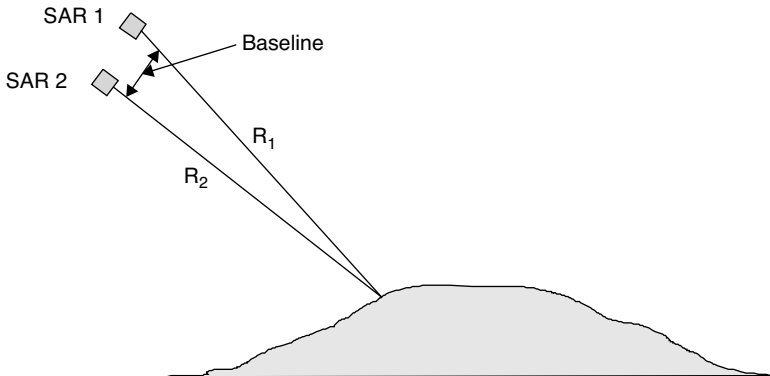


FIGURE 18.6 Radar interferometry expresses the interference created between two mutually coherent backscattered fields. The phase difference interferogram (modulo 2π) corresponds to the relative elevation of the illuminated terrain (*after removal of the systematic slant-range and Earth-curvature signatures*).

conventional interferometric SAR measurements from one spacecraft platform usually are not practical, since the implied spatial or temporal separations of the measurements are much larger than one satellite could support. (An alert reader may note the obvious exception to this rule, SRTM described previously, which mounted its second interferometric antenna on a 60-m extendable strut.)

Satellite orbits tend to be well-known, and follow very similar trajectories over subsequent repeat periods. It follows that the space-based environment offers an attractive alternative: repeat-pass interferometry, originally suggested by Goldstein.⁴⁶ If the pass-to-pass observations are separated in the vertical plane, then interferometry leads to relative terrain height estimation.⁴⁷ If two observations have a time delay corresponding to the repeat period of the orbit (typically 10 to 45 days), then sub-wavelength movements (in the line-of-sight direction of the radar) may be measured.⁴⁸ The technique can be extended to multiple passes with proportionate increase in the temporal baseline, leading to quite remarkable results. Repeat-pass techniques are well suited to mapping topographic relief and to long-term coherent change detection for mapping glacier movement or terrestrial subsidence. If shorter time scales are of interest, to detect moving vehicles, for example (GMTI), then a shorter interferometric baseline is required, which implies two (or more) SBRs in relatively tight co-orbiting formation.

The basic SAR interferometric environment is one in which there is a pair of mutually coherent images that have embedded phases that depend on the details of viewing geometry and scene structure. The coherently combined images are known as an interferogram, which typically contains fringes that express the interactions between the phase structure of the two data sets. Signal processing is designed to estimate these phase differences, and to deduce geophysical parameters of interest from the resulting measurement.⁴⁹

The interferometric signal model is simple in concept. For any neighborhood in the scene, the input signal pair may be described by

$$s_1(t) = \Gamma_1 a \exp[-j\varphi] \quad (18.10)$$

and

$$s_2(t) = \Gamma_2 a \exp[-j\varphi + j\Delta\varphi(r, t_2 - t_1)] \quad (18.11)$$

where the subscripts on the reflectivity Γ suggest that the two signals may be obtained at two different points in time as well as from two different spatial perspectives. The objective is to estimate the relative phase difference $\Delta\varphi$, usually found through the cross-correlation

$$E[s_1(t_1)\bar{s}_2(t_2)] = R_{12}(t_1, t_2)a \exp[-j\Delta\varphi(r, t_2 - t_1)] \quad (18.12)$$

which is presented as it would be calculated using complex image data. Here, $E[\cdot]$ is the expectation (averaging) operator. The phase difference $\Delta\varphi$ may be due either to geometric or to temporal differences between the two observations. Successful interferometry depends on the cross correlation $R_{12}(t_1, t_2)$ of the scattering functions Γ_{t_1} and Γ_{t_2} . The normalized cross-correlation function is the *mutual coherence function*

$$\gamma_{12}(t_1, t_2) = \frac{R_{12}(t_1, t_2)}{\sqrt{E[|s_1|^2]}\sqrt{E[|s_2|^2]}} \quad (18.13)$$

in parallel to that encountered in physical optics.⁵⁰ Gamma is a quantitative mapping of the coherence between the two observations. In general, scene coherence decreases with shorter wavelength and longer time between observations.

Mutual coherence is an essential ingredient for radar interferometry. Coherence implies two constraints: spatial and temporal. The spatial constraint applies to the spacing between the orbital passes. Ideally, the radar wavelength projected onto each area of the surface must be the same from both orbits. Since the two orbits are separated, each area is observed at a slightly different incident angle. This implies that the effective wavelength projected onto the ground plane is slightly different for the two cases. Interference is supported only if the range bandwidth of the radar signal is sufficient to span the projected wavelengths, which becomes more demanding as the orbit separation increases.⁵¹ Fortunately, the range pulse has sufficient bandwidth (usually more than 15 MHz) so that mutually coherent range bandwidths can be chosen from the data at the time of processing. Loss of mutual coherence through increasing orbit spacing is known as *baseline decorrelation*.⁵² One may show for reasonably level terrain that the upper bound constraint on the difference $\Delta\theta_{\text{Rad}}$ in elevation angle between the two orbits is $\Delta\theta_{\text{Rad}} = \lambda \tan\theta_{\text{Rad}} / 2r_R$, where r_R is slant range resolution, which is inversely proportional to range bandwidth. (*Alert:* In the SAR interferometric literature, it is customary to use elevation angle, defined as the angle between the radar line of sight and the Earth radius vector, as seen from the radar.) For typical large time-bandwidth product signals, the elevation angle constraint implies that correlation of the pair of return signals is maintained for orbital separations on the order of a kilometer. For absolute elevation maps to be derived, however, precise knowledge to the level of one meter is required of the spatial separation between observation tracks.

Temporal coherence applies primarily to the scene. In order for the two signals to act as an interferometric pair, their respective phase structures must be relatively stable over the time interval between satellite observations. In short, there must exist mutual coherence between the two scattering signals, even though they are observed at different times. This requirement is readily satisfied for short interopportunity intervals, such

as from the three-day repeat orbit first used with Seasat data to prove the concept and for stable terrain features, such as unvegetated rocky mountain slopes. It is not necessarily satisfied for scenes, such as ice or vegetation, that may undergo changes in the details of reflection and scattering between observations.

In certain natural and most urban scenes, there will be many corner-reflector-shaped features whose phase remains stable over very long time scales. These so-called permanent (or persistent) scatterers⁵³ support differential interferometric measurements that may span many repeat visits of the radar, leading to remarkable sensitivity to slow-motion phenomena. For example, multiframe DInSAR[‡] analysis of RADARSAT-1 data has led to maps of New Orleans subsidence rates,⁵⁴ which vary from ~3 mm/y to more than 15 mm/y, with a sensitivity on the order of 2.5 mm/y.

Any approach to phase difference measurement is subject to the fundamental 2π ambiguity characteristic of phase estimation algorithms.^{55,56} In many radar situations, knowledge of the physical constraints of the situation, coupled with phase unwrapping algorithms, is sufficient for the purpose.

Polarimetry. For any given polarization of the transmitted wave, the reflectivity process in general will give rise to a diversity of polarizations in the backscattered wave. To observe these, the radar must be dual-polarized. Similarly, the reflectivity is a function of the polarization of the transmitted wave. Thus, if the scattering function itself is to be fully characterized, two orthogonal polarizations must be transmitted as well. Increasingly, polarimetric diversity is being implemented in space-based SARs.^{41,57} Implementation of a fully polarimetric radar always implies greater data channel capacity, more transmitted power, and less range swath coverage. Of course, the antenna—the radar’s “polarization gateway”—must be able to receive, and possibly also to transmit, on more than one polarization.

In general terms, there are four options available for polarimetric diversity in a space-based SAR. These are:

- (1) **Single (monostatic) polarization** Typical of all dedicated spacecraft SARs (until the launch of ENVISAT) with either HH or VV polarizations. This customary notation indicates horizontal or vertical (linear) polarizations on both transmission and reception for these single-polarized radars.
- (2) **Dual polarization** The traditional definition is transmission on one polarization (usually linear, such as H), and reception on the like-polarized and the cross-polarized components (such as H and V). In a traditional dual-polarized radar, the relative phase between the two polarized data sets is discarded. In Earth-oriented remote sensing radars, typical combinations include HH and HV, for example, or HH and VV (which requires two separate transmit polarizations). The ASAR aboard ENVISAT is the first space-based example of this type of polarization diversity. If the four (linear) polarization possibilities are exploited noncoherently, then the backscattering function of the scene may be characterized by the three backscatter coefficients ($\sigma_{HH}^0, \sigma_{VH}^0, \sigma_{VV}^0$), which, of course, are devoid of phase. (Note that reciprocity implies that $\sigma_{HV}^0 = \sigma_{VH}^0$.)
- (3) **Coherent dual polarization** A dual-polarized radar that retains the relative phase between the two received polarizations is a significant departure from traditional dual-polarized systems. The modifier “coherent” helps to distinguish

[‡] Differential interferometric synthetic aperture radar.

such radars from their more common counterparts described in the preceding paragraph. Coherent dual polarization has not been exploited in orbital SARs (although it is standard practice in Earth-based radar astronomy through facilities such as the Arecibo radar telescope⁵⁸). Experience has shown that there is relatively little added value in the phase between the like-polarized and cross-polarized returns under the condition of H or V transmit polarization. However, an innovative alternative is to transmit circular polarization and receive coherently two orthogonal linearly polarized components. (See Section 18.4 for further discussion.)

- (4) **Full or quadrature polarization** This is the richest option because it allows full characterization of the complex matrix of the backscatter at all resolved points in the scene. It has been developed extensively in theory and in practice with data from airborne systems and SIR-C. Japan's PALSAR is the first operational space-based system to incorporate a quad-pol mode.

Primary interest in fully polarimetric radars derives from the enriched scattering observation possibilities revealed through replacement of the scalar form of reflectivity by its complex vector counterpart.^{41,57,59} Thus, when either H or V polarizations are incident on a scattering element, both polarizations are backscattered according to

$$\begin{bmatrix} E_H^B \\ E_V^B \end{bmatrix} = \begin{bmatrix} S_{\text{HH}} & S_{\text{HV}} \\ S_{\text{VH}} & S_{\text{VV}} \end{bmatrix} \begin{bmatrix} E_H^T \\ E_V^T \end{bmatrix} \quad (18.14)$$

where the superscript *B* denotes the field components reflected back toward the radar. The new terms of interest represent the scene's 2×2 scattering matrix, an array of four complex numbers. Each element in this backscattering matrix expresses the magnitude and phase imposed onto the backscattered field (superscript *B*) in response to the illumination from the transmitted field (superscript *T*), according to their respective polarizations. Thus, the scattering matrix is a quantitative description of the transformation of polarization state upon reflection, as well as the magnitude and phase of each reflection coefficient. It is often true that the field polarizations are not changed during propagation, the irrotational assumption. In this case, the polarizations of the backscattered waves are equivalent to those that arrive at the radar. This property characterizes most of the polarimetry literature, at least in remote sensing applications, and is reflected in these paragraphs. (The principal exception to this rule is Faraday rotation, which may be a significant factor for longer wavelength systems, such as P band and to a lesser extent L band.)

For irrotational propagation, the portion of the backscattered field captured by the radar is determined by the polarization vector of the receiving antenna, $[E^R]$. The signal voltage v_{rec} entering the system may be written in vector-matrix form as

$$v_{\text{rec}} = [E_H^R \quad E_V^R] \begin{bmatrix} E_H^B \\ E_V^B \end{bmatrix} \quad (18.15)$$

This is the starting point for SAR quadrature polarimetry. Essentially, a quad-pol SAR is managed so that the transmitter generates both orthogonal polarizations. The resulting quad-pol data set can be transformed to represent all possible combinations of transmit and/or receive polarizations. Pitfalls await the unwary, however, including tricky coordinate conventions,⁵⁹ an initially confusing variety of "standard" forms for

representing the data, and several alternative methods for data analysis. Once mastered, however, quad-pol SAR data is the undoubted gold standard for quantitative scene characterization by an imaging radar.

A space-based quad-pol capability implies a significant cost. The driving requirement is that the data must be mutually coherent. That is relatively easy for the receiver, which only needs to have two channels that capture simultaneously the phase and amplitude of two orthogonal polarizations of the backscattered field. On the other hand, only one polarization can be transmitted at a time. Illuminating the scene with two polarizations requires the transmitter to be toggled between orthogonal polarization states. This multiplexed transmission scheme implies that the radar's PRF must be doubled to satisfy the minimum Nyquist sampling rate simultaneously for each pair of transmissions. Doubled PRF implies that the average radiated power must be doubled and the unambiguous range swath is halved, both in comparison to the standard case of transmitting only one polarization. Note that the average data rate is the same as the dual-polarized case, since twice as much data are collected by a quad-pol mode for each resolved point in the scene, but the swath width is smaller by a factor of two.

Considerable progress continues to be made in the development of tools for quantitative analysis⁶⁰ of polarimetric SAR data. When in combination with interferometric data,⁶¹ the field is known as PolInSAR, for which dedicated specialist meetings are convened frequently. An important methodology is target decomposition,⁶² through which specific backscatter classes (such as double-bounce, Bragg, or volume) of a scene may be separated from other types, thence subjected to interferometric analysis. Using such techniques, it is possible to estimate the topography of the surface beneath a vegetated canopy, for example.

Applications. SARs are the largest class of space-based remote-sensing radars, primarily as a result of their practical utility. Many applications are energized by radar's natural ability to operate at night or through cloud, fog, smoke, and haze, and its inherent sensitivity to changes within the scene at wavelength scales. Radar imagery has proven to be valuable for a wide variety of applications, from oceanographic observations (the theme that motivated Seasat) to measurement of millimeter-scale displacement (such as the subsidence of urban areas or the swelling of volcanoes prior to their eruption). Canada's requirement to maintain near-continuous monitoring of its northern and coastal ice is met primarily by thousands of frames of RADARSAT data per year. India is the second largest consumer of space-based imaging radar data, used for agriculture and forest management, and for measuring changes in its alpine glaciers. Countries such as Brazil graced with tropical forests rely on space-based radar imagery to maintain surveillance and to compile annual statistics of deforestation. Since radar imagery is a reliable method of mapping slicks on the ocean's surface, it is the principal means of monitoring oil spills that may result from a grounded tanker or a vessel illegally pumping its bilges in a coastal area. The imaging radar reference⁵ cited earlier provides an excellent review of many of these applications.

18.3 ALTIMETERS

In its most general form, an altimeter is a radar device designed to measure the vertical distance between the radar and the surface below. In airborne applications, the resulting "altitude" is a measure of the clearance beneath the aircraft. Whereas the

main objective of a space-based altimeter is also to measure the distance between the radar and the surface, the most common application is determination of the local sea level relative to the Earth's geoid,[§] rather than the height of the spacecraft. The reference for this measurement—the orbital height of the spacecraft—must be known by other means to within a few centimeters. Sea-surface height is a function of many geophysical parameters, such as current flow, an El Niño event, and variations in the ocean's depth. Relatively small changes (on the order of cm) in mean sea-surface height may correspond to substantial differences in the corresponding geophysical parameters. It follows that range measurement *accuracy* and *precision* are the driving requirements for this class of radar. The accuracy of an altimeter's height measurement depends to first order on knowledge of the spacecraft's height along its orbit and on correction of the propagation delays suffered by the radar's round-trip waveform. The precision of an ocean-viewing altimeter is proportional to the radar's range resolution and inversely proportional to the square root of the number of statistically independent measurements (looks) combined for each data point. Ocean-viewing altimeters, in general, have large SNR. Thus, bandwidth and looks become the driving requirements on system design. The emphasis in this section is on altimeter precision.

Sea-surface height measurements have become essential for a wide variety of applications in oceanography, geodesy, geophysics, and climatology.⁶³ With the exception of near-polar ice, Earth-orbiting oceanographic altimeters have seen relatively little application over nonaqueous surfaces.

A satellite-based altimeter systematically circles the Earth, generating surface height measurements along its nadir track. These measurements accumulate, providing unique synoptic data that have revolutionized our knowledge and understanding of both global and local phenomena, from El Niño to bathymetry. SBR altimeter data also provide measurements of significant wave height and wind speed. Although one might consider altimeters to be relatively simple one-dimensional (range measurement) instruments, their phenomenal accuracy and precision requires elegant microwave implementation and innovative signal processing.

Overview. The surface-height measurement objectives of space-based altimeters can be grouped into four broad categories: large-scale dynamic sea-surface topography, dynamic mesoscale^{*} oceanic features, static mesoscale sea-surface topography, and ice—sea ice as well as continental ice sheets. Each of these measurement themes implies narrowed constraints on choice of orbit and on the top-level instrument and mission design. Satellite altimeters dedicated to determining the ocean's large-scale dynamic surface topography are characterized by absolute sea-surface height (SSH) 1-sec-averaged measurement accuracy on the order of centimeters along tracks of more than 1000 km, and orbits that retrace their surface tracks every 10 to 20 days. In contrast, mesoscale missions focus on sea-surface height signals of less than ~300 km in length. Rather than absolute SSH accuracy, these shorter-scale applications require precision sufficient to sustain surface slope measurement accuracy on the order of 1 microradian (one mm sea-level change over a 1-km distance). For geodetic signals that are expressed through static sea-surface topographic variations, orbits are required that generate dense track-to-track spacing. Observation of oceanic and

[§] The average sea level in the absence of dynamic perturbations of the surface elevation due to tides and currents.

* In the field of oceanography, mesoscale features have scales of several hundred kilometers, as opposed to the much larger basin scale (the North Atlantic ocean, for example).

polar ice sheets requires that the altimeter have robust range and spatial resolution, accuracy, and precision regardless of the non-zero average surface slope in both the along-track and cross-track direction of the continental glaciers. Suitable orbits for ice sheet missions must have near-polar inclination and multiyear relative accuracy of a few centimeters.

Whereas the methodology of these instruments is to determine the distance between the radar and the surface, like any radar, an altimeter actually measures round-trip delay, not distance. At the accuracy required of a space-based oceanographic altimeter, the deceptively simple proportionality of range to delay-time must take into account the small but significant retardation of the radar's microwaves as they propagate. The cm-level SSH accuracy required of these instruments is much smaller than the ranging errors introduced by delays through the ionosphere and the atmosphere. The delays imposed by the ionosphere are a function of frequency. In practice, these can be estimated and then corrected if the altimeter measures round-trip range at two different frequencies. The delays imposed by the atmosphere are comprised of two components: the dry atmosphere and water-vapor. The dry atmosphere component is well-known and stable at long spatial scales; in practice, the resulting delay is compensated by recourse to model predictions. Delays due to water-vapor in the atmosphere are variable down to scales of several hundred kilometers (and much smaller when traversing a storm front). Standard practice is to measure the integrated water vapor contribution in the vertical column below the altimeter by a microwave radiometer, for which two or three frequencies are required.

Measurement errors are dominated by the accuracy of orbit height determination and by the intrinsic precision of the instrument. Figure 18.7 shows a summary history of these factors. The data show that 2-cm instrument accuracy is the state-of-the-art for conventional altimeters. The delay-doppler instrument (see below) would further improve instrument precision⁶⁴ to 1 cm.

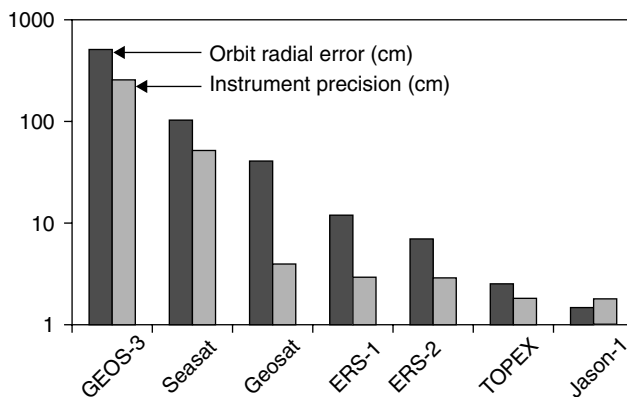


FIGURE 18.7 History of precision orbit determination (POD) and intrinsic instrument precision of the leading radar altimeters of the past 30 years. Vertical axis in cm. Modern POD accuracy relies on GPS and the French DORIS system. Precision is limited by the altimeter's degrees of freedom (incoherent waveform averaging). (after Dudley Chelton, Oregon State University, personal communication)

Centimeter-scale range accuracy is supported in the oceanographic application by averaging over the range response of many returns. The range resolution of each return waveform is typically on the order of 0.5 meters. These waveforms are accumulated and averaged pulse-to-pulse, whose shape converges on the flat-surface impulse response^{65,66} (Figure 18.8). Sea-surface height (SSH) is derived from the time delay to the midpoint of the waveform's leading edge rise. One thousand or more such waveforms averaged over one second correspond to a mean range estimate whose standard deviation is on the order of centimeters (which, in practice, degrades with increasing significant wave height). One-second averages are standard for operational altimeters, which implies an along-track resolution on the order of 7 kilometers, determined primarily by satellite velocity. Averaging is “the name of the game” in radar altimetry.⁶⁷ For example, global data sets from instruments such as TOPEX and Jason-1 have been analyzed to estimate the rate of mean sea-level rise to an accuracy of 1 millimeter per year.

In addition to sea-surface height, the satellite radar altimeter's waveform supports two other oceanographic measurements: significant wave height (SWH) and surface wind speed (WS). Over a quasi-flat sea, a pulse-limited altimeter's idealized mean

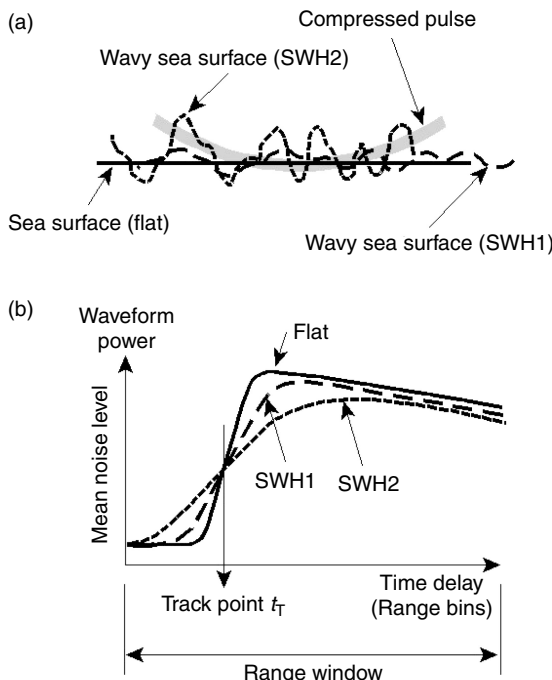


FIGURE 18.8 (a) The altimeter's pulse (typically 0.5 m long after compression) sequentially encounters oceanic surface waves (of height up to 20 m or more). (b) Sea-surface height (SSH) corresponds to the midpoint of the waveform's leading edge, significant wave height (SWH) to the slope of the leading edge, and wind speed (WS) to the (inverse) backscattered power. The waveforms depicted here are idealized; useful “smoothness” requires 1000 or more incoherently averaged radar returns.

waveform is a step function, whose rise time is equal to the compressed pulse length and whose position on the time-delay axis is determined by the altimeter's height. If the sea surface is modulated by waves, the altimetric depth of the surface increases, which reduces the slope of the waveform's leading edge. Hence, SWH is proportional to the waveform rise time. If the sea surface is disturbed by the wind, the resulting fine-scale roughness decreases the power of the pulse reflected back to the altimeter. Hence, for wind speeds of more than about two knots, WS is inversely related to mean waveform power. In practice, the inflections of the idealized flat-surface response function waveform are softened by the pulse weighting, and the waveform is attenuated over time by the weighting of the antenna pattern.

To extract SWH and WS from waveform data, finely tuned algorithms have been developed and validated against in situ buoy measurements.⁶³ For example, the TOPEX K_u band altimeter measures SWH to within ± 0.5 m up to more than 5.0 m and WS within ± 1.5 m/s up to more than 15 m/s. These figures correspond to averages over 1 second, or about 7 km, along the sub-satellite path of the altimeter's footprint, which typically is 3 km–5 km wide, determined by mean sea state.

Flight Systems. Key attributes of satellite radar altimeters are summarized in Table 18.4. Since 1973, oceanic height measurement accuracy has improved, due primarily to more effective means of estimating and correcting systematic errors. Performance also has benefited from innovative onboard hardware and algorithms and more precise determination of the radial component of the orbit. The Jason-1 altimeter represents the state-of-the-art in absolute sea-surface height measurement accuracy (as of the year 2007).

S-193 and GEOS-3. The first satellite radar altimeter was the proof-of-concept S-193 instrument⁶⁸ that flew on three Skylab missions. Its objectives were to verify predicted waveform response to wind and waves, to measure the radar cross section of the sea at vertical incidence, to measure inter-pulse correlation properties, and to observe the effect of off-nadir antenna orientation (a scatterometer experiment). Geos-3 provided the first geodetic and geophysical results of significance within the National Geodetic Satellite Program, including the first maps of sea-level variability and the

TABLE 18.4 Altimeters

Spacecraft	Country	Year	Repeat	Inclination	Altitude	Spacing	H2O correction		Accuracy
							days	degrees	km
Skylab (3)	USA	1973	No	~48	435	n/a	K _u	–	50 m
GEOS-3	USA	1975–8	No	115	845	~60	K _u	–	50
Seasat	USA	1978	~17, 3	108	800	160, 900	K _u	Yes	20
Geosat	USA	1985–1989	GM, 17.05	108	800	~5, 160	K _u	–	10
ERS-1	ESA	1991–1996	3, 35, 176	98.5	785	900, 80, 15	K _u	Yes	7
TOPEX / Poseidon	USA/ France	1992–2005	9.916	66	1336	315	C, K _u	Yes	2
ERS-2	ESA	1995–	.35	98.5	785	80	K _u	Yes	5
GFO	USA	1998–	17.05	108	800	160	K _u	Yes	5
Jason-1	France	2001–	9.916	66	1336	315	C, K _u	Yes	1.5
Envisat	ESA	2002–	.35	98.5	785	80	S, Ku	Yes	7
Jason-2	France	2008	9.916	66	1336	315	C, Ku	Yes	1.5
Altika-3	India (Fr)	2009	.35	98.5	785	80	Ka	Yes	1.8
CryoSat-2	ESA	2009	369	92	720	n/a	Ku	–	5
Sentinel-3	Europe	2010	.35	98.5	785	80	C, Ku	Yes	5

marine geoid.⁶⁹ Geos-3 and the S-193 altimeters used conventional pulse-compression techniques. As suggested in the table, neither of these two early altimeters included a water-vapor radiometer, and each used only one frequency, so that they had no in-built means to correct for ionospheric or atmospheric propagation delays.

Seasat's Altimeter. Seasat's was the first to use full deramp[†] pulse compression,⁷⁰ which opened the way for the very small range resolution required for many oceanographic applications. The deramp technique (described below) has been adopted by all radar altimeters since then. Seasat was designed to measure global ocean dynamic topography, as well as wave height and surface wind speed.

Geosat. This altimeter's design⁷¹ was patterned closely after that of the Seasat altimeter. Geosat was a U.S. Navy military satellite whose primary mission was to map the Earth's marine geoid to then-unprecedented accuracy, for which a non-repeat orbit was required. Since its public release in 1995, the data set from the first 18-month geodetic mission has become the backbone of the global bathymetric chart that is the industry standard.^{72,73}

Geosat's secondary mission was to observe dynamic mesoscale oceanographic phenomena, for which it was maneuvered into an exact repeat orbit (period 17.05 days).⁷⁴ Geosat's geodetic mission and exact-repeat mission are known as GM and ERM, respectively. As a spacecraft, Geosat was one of the few Earth-observing missions to rely on the purely passive gravity-gradient means of attitude control,⁷⁴ as evidenced by the extended (vertical) boom in Figure 18.9. The attitude was stable to less than 1°, to which the altimeter's pulse-limited range measurement was robust.

Geosat Follow-On (GFO). GFO was designed to replicate as much as possible the Geosat exact-repeat mission, in support of operational requirements for the U.S. Navy. GFO represents the current state-of-the-art in small dedicated radar altimeter missions. It includes a dual-frequency water-vapor radiometer (WVR) at 22 and 37 GHz, data from which are used to reduce the corresponding propagation uncertainty to 1.9 cm.

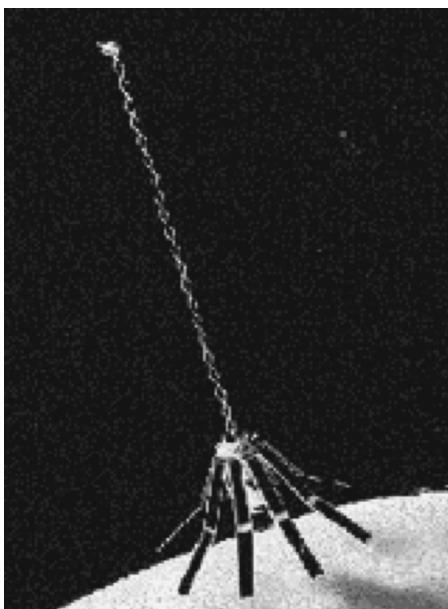


FIGURE 18.9 The Geosat radar altimeter: The nadir-directed antenna (a reflector) is hidden inside of the solar arrays. This spacecraft maintained verticality by gravity-gradient (hence the long boom and counterweight). The data were impervious to randomly oriented yaw angles (about the vertical axis). (Image courtesy of Johns Hopkins University Applied Physics Laboratory)

[†] Full deramp (or simply deramp) is standard terminology in space-based radar altimetry. It is known more commonly to most radar engineers as the Stretch technique.

The radar's mass is 45 kg (including full redundancy and the WVR); its prime power consumption is less than 100 W. Total spacecraft dry mass[‡] is about 300 kg.

TOPEX/Poseidon. In the late 1980s, program planning for satellite radar altimeter missions split into two themes, determined by the relative priority of their measurements. If the altimeter were the prime payload instrument, then the orbit and mission design could be optimized accordingly. This theme was followed by TOPEX/Poseidon (T/P), a joint United States (NASA) and French (CNES) mission. TOPEX was designed to measure and map the dynamic ocean topography with sufficient accuracy to determine large-scale circulation patterns.⁷⁵ TOPEX' most famous contribution is early observation and near-real-time monitoring of El Niño events, whose height signature over the equatorial eastern Pacific ocean typically is an increase on the order of 10–20 cm with respect to the mean. Poseidon, contributed by France, was a small proof-of-concept instrument that had a solid-state transmitter. Poseidon was the precursor of the Jason altimeters and the SIRAL instrument aboard CryoSat.

The T/P orbit repeat period was chosen carefully to satisfy adequate observation of the dominant aliased tidal constituents. All solar tidal constituents would be ambiguous with other height signals if the repeat period were an integral number of days. For T/P, the time of day for each subsequent observation slips by about two hours. The T/P repeat pass footprint location accuracy is better than ± 1 km, a requirement that is bounded by the cross-track gradient of the oceanic geoid. The T/P instrument package included a three-frequency radiometer. TOPEX was the first altimeter to use two frequencies (time-multiplexed) to estimate and compensate for propagation delays⁷⁶ imposed by ionospheric electrons. Designed for an initial three-year mission, subsequently stretched to five years, T/P provided valuable data for an impressive thirteen years. T/P was formally decommissioned in December 2005.

As is true for most radars, the received waveform produced by an individual pulse from TOPEX was corrupted by coherent self-noise known as speckle. The standard deviation of speckle is reduced by summing (averaging) many statistically independent waveforms together. Statistical independence between sequential returns observed by a radar altimeter depends primarily on the radar pulse repetition rate, the antenna size, the spacecraft velocity, and on the sea surface conditions.⁶⁷ The antenna was a 1.5-m reflector that served both altimeter bands and also the radiometer. Selected parameters associated with the altimeter's design are listed in Table 18.5. The pulse-to-pulse

TABLE 18.5 TOPEX Parameters

Parameter	Value	Units
LFM rate	3.125	MHz/ μ s
Pulse duration	102.4	μ s
Pulse BW (radiated)	320	MHz
Time \times bandwidth	32768	(dimensionless)
Pulse resolution	0.469	m
Carrier (K_u band)	13.6	GHz
Carrier (C band)	5.2	GHz
IF frequency	500	MHz
Stretch bandwidth	3	MHz
Range time span	400	ns

[‡] Total mass, not including consumables such as fuel for propulsion or attitude control.

statistical independence requirement evaluated for the TOPEX indicates that the maximum PRF should be 2.5 kHz, yet it was 4.5 kHz in practice. The pulse rate above the threshold improved the additive SNR, but did not contribute to speckle reduction. The PRF statistical independence limit decreases with increasing significant wave height.

Jason-1. Jason-1 followed in the footsteps of TOPEX, figuratively and literally. After the launch of Jason-1 into the T/P orbit, TOPEX was maneuvered into a “tandem” phasing so that the measurements of the two altimeters could be cross-calibrated. Jason-2 is essentially identical to Jason-1.

ERS-1, ERS-2, and ENVISAT. If the altimeter is not the primary payload, then the resulting mission and orbit are likely to be determined by other requirements, which may compromise altimetry. The European Space Agency’s satellite altimeters on ERS-1 and ERS-2, as well as the advanced radar altimeter²¹ RA-2 on ESA’s ENVISAT, are of second priority with respect to the other instruments on their respective spacecraft. Their sun-synchronous orbits are less than optimum for most altimetric applications, due primarily to the fact that four of the eight dominant tidal constituents are sun-synchronous.⁶³ These orbits are also at lower altitudes than the T/P orbit, which implies that orbit maintenance maneuvers must be more frequent, thus compromising precision orbit determination. During a portion of its mission, the orbit of ERS-1 was rephased to a long repeat period (176 days). That long repeat period generated a relatively dense surface sampling grid useful for estimating sea ice cover, geodesy, and bathymetry. The ERS-2 mission did not vary its repeat period. The consequence of these orbit properties is that the resulting data are not well suited to measuring the annual rate of sea-level rise, which is a key climate-related variable.

CryoSat. This was the first Earth Explorer Opportunity Missions, which was part of the European Space Agency’s Living Planet Programme. The mission concept⁷⁷ was selected in 1999 and subsequently launched in October 2005. Unfortunately, the launch vehicle malfunctioned. ESA and its member states authorized a replacement. The CryoSat orbit has a high-inclination (92°) and a long-repeat period (369 days, with a 30-day subcycle), designed to provide dense interlocking coverage over the polar regions. Its aim is to study possible climate variability and trends by determining the variations in thickness of the Earth’s continental ice sheets and marine sea ice cover. CryoSat is described in more detail in a subsequent section.

AltiKa. AltiKa differs from other ocean-viewing altimeters in this section, due primarily to its use of K_a band (35.75 GHz) rather than K_u band. The first instrument (from France) is part of the payload on India’s Oceansat-3. AltiKa⁷⁸ is single-frequency since at K_a band the retardation due to the ionosphere is sufficiently small that it does not have to be measured and compensated. However, the ~0.84 cm wavelength is vulnerable to atmospheric moisture; it is predicted that as much as 10% of the data will be compromised by rain. The 33 kg instrument requires an input power of 80 W. The offset-fed reflector antenna is 1 m in diameter, resulting in a beamwidth less than half that of its K_u band counterparts. Several advantages are claimed for the smaller beamwidth, including operation closer to land. On the other hand, the narrower beam implies that the waveform is more sensitive to spacecraft attitude errors. AltiKa’s 500 MHz bandwidth leads to a pulse-limited footprint about 30% smaller than usual.

The PRF is 4 kHz, approximately twice that of most conventional altimeters, slightly larger than the pulse-to-pulse statistical independence condition of 3.75 kHz.

Orbit Considerations. Given an arbitrarily good radar altimeter, its orbit becomes the dominant factor that may limit sea-surface height measurement accuracy.⁷⁹ Orbit selection for an ocean altimeter requires consideration of the impact of an orbit's inclination, repeat period, and altitude. For example, if the objective is absolute sea-surface height accuracy over larger spatial scales and long time scales, then a higher altitude orbit having a relatively moderate prograde inclination, and relatively short non-sun-synchronous repeat period is the only sensible starting point.

An altimeter's revisit period is ten days or more, in contrast to tides with approximately 1 or 2 cycles per day driven primarily by lunar and solar gravity. As a result, all tidal signals sensed by an altimeter are undersampled. Altimetric data retain the resulting aliases, which over the course of a year or so can be identified, quantified, and calibrated out. An altimeter's orbit must be chosen so that the tidal aliases do not get confused with signals of geophysical interest.

The T/P Orbit. The state-of-the-art (at least in accuracy and large-scale circulation studies) is Jason-1, operating in the orbit originally designed for TOPEX/Poseidon. The orbit parameters include repeat period 9.9156 calendar days (unfortunately, often stated as 10 days); inclination 66°; repeat track separation at the equator (316 km); and altitude 1336 km. The radial component of precision orbit determination (POD) is on the order of 2 cm for T/P, and Jason-1 results show POD to a level of 1.5 cm. Although these parameters reflect the fruits of multiple years of trade studies by many individuals,⁶³ at least one unwanted characteristic remains. The K1 tidal alias is very nearly two cycles per year, thus appearing close to geophysical signals associated with seasonal effects. K1 cannot be ignored, as it is the largest diurnal constituent and is second in magnitude only to the dominant lunar constituent.

The constraint on the exactness of an orbit's repeating ground track is determined to first order by the fine structure in the local geoid expressed at the ocean's surface.⁷⁵ For example, cross-track surface slopes (gradients) in the geoid may be as large as 2×10^{-4} near the deeper oceanic trenches. In such an extreme case, a cross-track drift of only 1 km would give rise to a 20-cm change in sea-surface height (SSH). In response, algorithms have been developed that correct SSH data for the effects of the larger cross-track geoid gradients. It also is standard practice to constrain an altimeter's cross-track drift to less than 1 km. Repeat tolerance usually is the condition that motivates active orbit maintenance maneuvers.

Non-Repeat Orbit. The precedent for this is Geosat⁷¹; its first 18 months were devoted to geodesy for which a non-repeat orbit is optimal. Geodetic missions map gravity anomalies reflected in subtle local tilts of the mean ocean surface. These are static mesoscale features of spatial scales less than about 300 km, determined by the topographic features, composition of the sea bottom, and stationary oceanic currents. Data from Geosat have been used to derive the standard bathymetric charts available for the global oceans.^{72,80}

Geosat ERM Orbit. The only other family of dedicated missions is that in the Geosat (1985–1989) Exact Repeat Mission (ERM) orbit, the same orbit used by GFO. This orbit has a period of 17.0505 calendar days (sometimes inappropriately

abbreviated to 17 days), 108° inclination, (consequently 160 km track-to-track spacing at the equator), and 784 km altitude.[§] From the Geosat orbit, half of the principal tidal constituents alias into unwanted frequencies (near zero, one, or two cycles per year). In particular, the dominant tidal constituent, the common twice-daily lunar tide, is aliased to 317 days, which is close to the annual cycle.⁸¹ Precision orbit determination is good to only about 7 cm, which is relatively large, due in no small measure to failure of the primary onboard GPS navigation subsystem.

Sun-Synchronous Orbit. Sun-synchronous satellites host European Space Agency (ESA) altimeters on ERS-1, ERS-2, and RA-1 on ENVISAT. All share the same orbit: 35.00 calendar days repeat period; 98.5° inclination; and 781-km mean equatorial altitude. Radial knowledge of these sun-synchronous orbits is good to about 5 cm, based on the Delft model.⁸² As sun-synchronous altimeters, the largest solar constituent (twice daily) aliases to zero, and all tidal constituents that are primarily dependent on solar forces alias to frequencies close to zero.

Theoretical Foundations. The following paragraphs provide a summary of the key characteristics of a space-based radar altimeter. Examples are drawn from the design of TOPEX.^{83,84}

Pulse-limited Altimeters. Figure 18.10 illustrates the pulse-limited condition.⁸⁵ The radius r_p of the area delimited on a quasi-flat surface by a pulse of length τ seconds on the Earth of mean radius R_E seen from a relative altitude of h kilometers is

$$r_p = \sqrt{c\tau h/\alpha_R} \quad (18.16)$$

where $\alpha_R = (R_E + h)/R_E$ is a consequence of the spherical observation geometry. For typical satellite radar altimeters, the pulse-limited footprint over a quasi-flat surface is on the order of two kilometers in diameter. The pulse-limited area A_p is

$$A_p = \pi r_p^2 = (\pi c\tau h)/\alpha_R \quad (18.17)$$

As the pulse continues to impinge and spread over the surface, the resulting pulse-limited annuli all have areas equal to that of the initial pulse-limited footprint. Hence, the received power tends to maintain the level corresponding to the peak of the initial response (Figure 18.10). The pulse-limited areas expand in response to increasing large-scale surface roughness, which in the oceanographic context is expressed as significant wave height (SWH). The height accuracy of a pulse-limited altimeter is much less sensitive to (small) angular pointing errors than is the case for a beam-limited altimeter.

Adaptive Tracking. A satellite-based radar altimeter needs to measure the distance accurately, but only for an essentially planar surface, oriented orthogonally to the radar's line-of-sight. Conservative design suggests that the measurement should be concentrated near the reflection from that surface. Hence, ocean-viewing altimeters have a small range window whose position tracks the delay and strength of the

[§] The Geosat ERM orbit was chosen for political as much as for technical reasons. It followed the Seasat orbit (1978) that had established a well-known precedent.⁷⁰

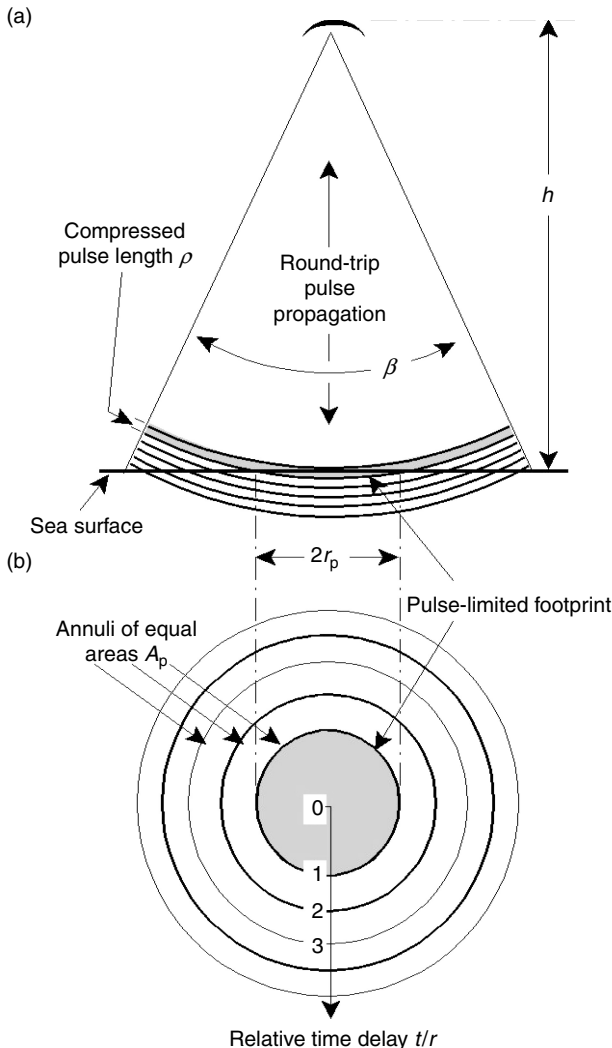


FIGURE 18.10 The pulse-limited condition: Over a nominally level flat surface, the altimeter's short pulse (a) reflects first from an area that may be much smaller than the footprint illuminated by the antenna pattern (b).

surface reflection.⁷⁰ The ocean's surface has a significant wave height of less than 20 m or so. Radar backscatter is primarily specular, typically spanning 3 dB to 20 dB, to cite parameters used in the testing of the TOPEX altimeter. In practice, range-gate delay and backscatter tracking are met with two servo-regulator feedback loops (Figure 18.11). The first loop is a second-order height tracker consisting of range position (alpha tracker) and range rate (beta tracker). The second loop is the receiver gain control (AGC). Altimeter height measurement is given by the setting of the

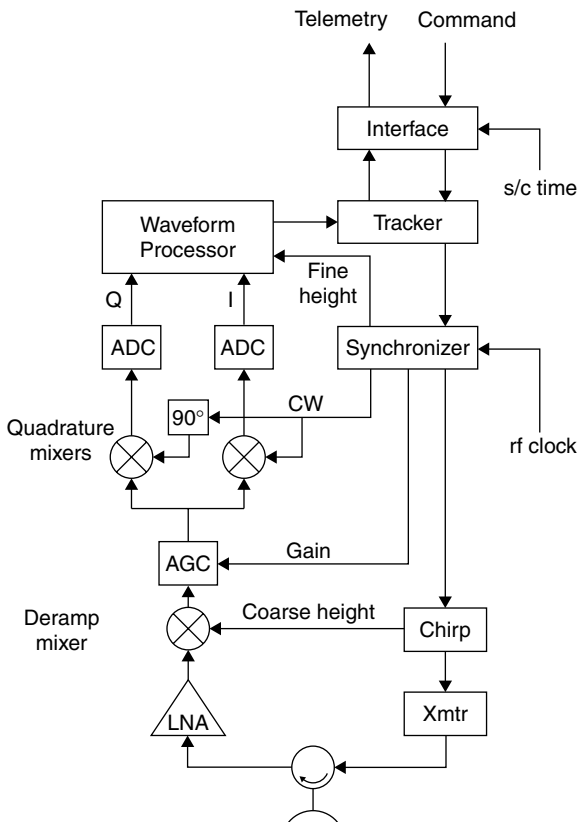


FIGURE 8.11 A generic signal flow diagram for an ocean-viewing radar altimeter. Principal feedback loops include range-gate tracking, both coarse (the alpha loop) and fine range-rate tracking (the beta loop), and mean signal power (the AGC loop).

range delay coarse and fine values, corrected by the remaining height error measured from the waveform's position in the tracker. Surface wind speed and significant wave height⁶³ are derived from the AGC values and the waveform's shape, respectively.

The precision of an individual height measurement is determined by the combination of range resolution and incoherent waveform averaging. If a single simple short pulse were transmitted, then the height resolution would equal the pulse length. The principal disadvantage of a short pulse is that it contains little energy. The inherent resolution of a pulse is inversely proportional to its bandwidth. Space-based radar altimeters use some form of modulation on the transmitted signal to maintain a large bandwidth within a longer pulse, thus increasing the transmitted energy at no loss of resolution.

Deramp on Receive. Satellite-based radar altimeters present an elegant embodiment of the Stretch technique,⁸⁶ which is known as *full deramp* in the field of space-based radar altimetry. This method was first employed by MacArthur in the Seasat altimeter,⁷⁰ and has been adopted as the standard technique since then for this type of radar. The distinguishing feature of this technique is a clever trade between the two key

parameters in a large time-bandwidth product (TBP) signal. After reception, demodulation is applied that transforms the “short time, large bandwidth” nature of the original pulse to “long time, small bandwidth” signals. Since the same TBP is maintained, the original resolution is preserved. The method is ideal for altimetry, since the range depth of the ocean’s surface is very much smaller than the time available in the pulse repetition period. Clearly, the full deramp technique offers a considerable savings in system bandwidth at all subsequent stages and at no cost in range resolution. The figures cited in Table 18.5 show that the ratio of waveform bandwidth to RF bandwidth for TOPEX is on the order of 0.05%. The TOPEX altimeter design is described more completely in the open literature.^{83,84}

Geosat: Geodetic Mission. Radar altimetric data are the basis for state-of-the-art gravimetric variations expressed at the ocean’s surface, and consequently, oceanic bathymetry.* The principal objective of a geodetic satellite radar altimeter⁷³ is to measure the (along-track) slope of the sea surface caused by gravity deflections over spatial scales less than a few hundreds of kilometers (Figure 18.12). These slopes are derived from the SSH measurements summarized above, but this application has its own unique implications for system design. The highlights are reviewed in the following paragraphs.

Sea-surface slope⁸⁷ is derived by taking the difference between two neighboring height measurements, where the slope tangent equals “rise over run.” The key word for these measurements is *precision*: the standard deviation (noise) of the sea-surface height measurement about its mean value. Height measurement precision is determined by the radar altimeter’s post-processing range resolution and by the amount of averaging available for each estimate. Note that a precision measurement may still have poor accuracy, if its mean value is biased away from the correct value. When comparing two neighboring height measurements, any constant bias is cancelled by subtraction as long as the error is the same for both measurements. The sea-surface slope measurement problem is challenging because the desired slope signals are as small as one microradian, equivalent to a 6 mm height differential (rise) for each 6 km along-track separation (run).

In addition to height precision, geodetic altimetry requires smaller along-track resolution than a conventional altimeter and an orbit that accumulates dense cross-track coverage. The altimeter’s footprint resolution should be smaller than about 6 km,

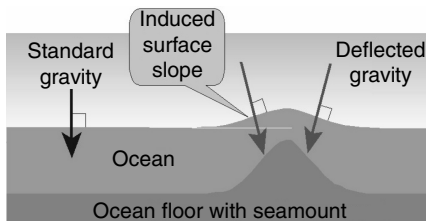


FIGURE 18.12 When averaged and stripped of dynamic (current-driven) features, the mean ocean surface is a direct expression of the local gravity gradient. State-of-the-art radar altimeters can measure the resulting slopes to a 1-microradian precision.

* Literally, measurement of the distance between the mean ocean surface and the local sea floor.

which corresponds to the minimum half-wavelength scale of the observable perturbations in the ocean's mean surface due to spatial variations in the Earth's gravity. The orbit should not repeat for ~ 1.2 years to yield an average ground track spacing of 6 km, again in respect of the gravity signal at the ocean's surface. The orbit's inclination should be near 50° – 63° to resolve north and east slopes nearly equally and to cover the lower latitudes where existing data are inadequate. Note that oceanographic radar altimeter missions (TOPEX/Poseidon, Jason-1, ERS1/2, ENVISAT, and Geosat ERM/GFO) are normally placed into exact-repeat orbits (10 to 35 days), and as a consequence, have widely spaced (80 km to 315 km) ground tracks. Such orbits cannot resolve the short-wavelength two-dimensional surface slopes required for useful geodesy.

Since absolute height accuracy is not required, geodetic radar altimeters can be relatively basic instruments.⁸⁸ They do not need to compensate for propagation delays; hence they need only one frequency, and they do not necessarily need a water vapor radiometer (WVR). Indeed, a simple instrument is preferred; it has been shown that efforts to correct for path delays usually add noise to slope estimates.⁸⁹ Geodetic measurements provided by the Geosat and ERS-1 (both single-frequency altimeters with no WVR) furnished the best resolution oceanic geodesy and bathymetry available up through at least 2010 for the open ocean. Their resulting bathymetric resolution is limited to about 25 km north-south and poorer resolution of east-west slope components. These results reflect the less-than-optimum resolution, waveform precision, and orbit inclination of those two altimeters. Geodetic resolution at the ocean's surface can be no finer than about 6 km (half a wavelength), a limit that is determined by the average depth of the ocean.

CryoSat: Ice Sheet Mission. Pulse-limited space-based radar altimeters work best over relatively mild topographic relief of mean slope zero, such as the ocean's surface. Over ice sheets or terrestrial surfaces, performance is degraded. Unwanted characteristics include footprint dilation over rougher terrain, height errors in proportion to surface mean slope, and the tendency of the minimum range measurement to hop from one elevated region to another (without the control or knowledge of the data analyst). Beam-limited techniques, of which laser altimeters are extreme examples, circumvent these problems, but may imply their own set of disadvantages.

A major potential application of radar altimetry is to monitor the height of extensive ice sheets, as found in Greenland or Antarctica. Approximately 95% of these land-ice surfaces have slopes less than $\sim 3^\circ$, which, although small, is sufficient to trick a conventional altimeter into very large height errors. For example, an unknown 1° slope would lead to a 120-m surface height error, which is unacceptable if cm-level interannual changes are the objective.

The CryoSat altimeter⁹⁰ is the first space-based radar altimeter designed to operate over ice (Figure 18.13). Its payload instrument is the SAR/Interferometric Radar ALtimeter (SIRAL), which has three modes: Conventional, SAR, and Interferometric. The Conventional mode (pulse-limited, described in the forgoing paragraphs) reflects its Poseidon heritage. The SAR mode is based on the delay-doppler architecture,⁹¹ which offers advantages in precision, resolution, and along-track surface slope tolerance. The Interferometric mode⁹² is designed to measure the cross-track surface slope component. Both of these advanced altimeter modes have been demonstrated with the D2P airborne altimeter.⁹³

Unlike previous radar altimeter missions, CryoSat will downlink all altimetric data with essentially no onboard processing. Data from each of the three modes are

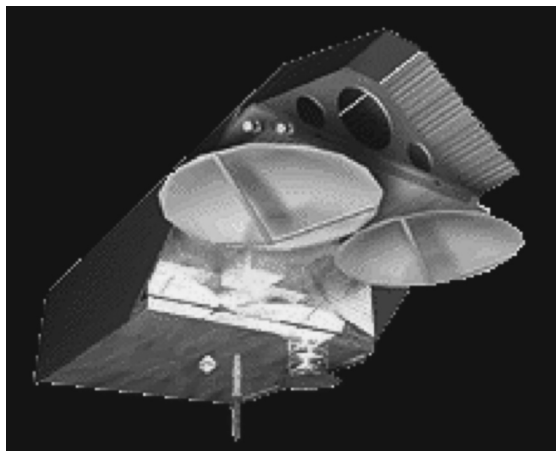


FIGURE 18.13 The CryoSat satellite and its SIRAL altimeter: The two antennas (Interferometric mode) are athwart the velocity vector, so that the differential phase (modulo 2π) of the first return indicates the cross-track position of the minimum-range reflecting surface, which, in effect, is a measure of the cross-track component of the mean surface gradient. (Courtesy of European Space Agency)

processed in ground-based facilities, since the more complicated waveforms from icy surfaces require iterative development of suitable processing algorithms by investigators prior to retrieving the desired information. The conventional mode is used for the open ocean (for calibration and sea-surface height reference purposes) and the central continental ice sheets that are relatively level. The interferometric mode is reserved for the more steeply sloping margins of the ice sheets. The synthetic aperture mode is used primarily over sea ice, where its sharper spatial resolution and precision support measuring the difference between the sea level and the top surface of floating ice (freeboard). Because the density of ice is relatively well-known, such freeboard measurements can be inverted to estimate ice thickness.⁹⁴

18.4 PLANETARY RADARS

The history of planetary imaging radars is summarized in Table 18.6. Venus has been the most popular destination,⁹⁵ largely because it is cloud-covered (hence its surface is not observable by optical means), its mass and size are similar to those of Earth, and spectral observations have shown that its atmosphere is ~98% CO₂, suggesting that a greenhouse effect could have overwhelmed what might have been a more hospitable planet. A popular theme for planetary exploration by radar is the search for evidence of water (especially water-ice).^{96,97} Data from radar missions are available through NASA's Planetary Data System.⁹⁸

Flight Systems. *Venera-8* performed the first simple radar measurements of Venus from a spacecraft. *Venera-8* carried a pulse-modulated radar altimeter, which returned 35 readings during its descent from orbit to its demise on the surface of Venus.

TABLE 18.6 Planetary Radars

Mission	URL	Planet	Year	Radar
Venera -8;9/10 (USSR)	1	Venus	1972, 75	Radar altimetry
Pioneer Venus Orbiter (PVO) (USA)	2	Venus	1978–92	ORAD: Altimeter (also coarse imagery); 17 cm
Venera 15/16 (USSR)	3	Venus	1983–84	SAR and altimeter; 8-cm wavelength
Magellan (USA)	4	Venus	1990–94	SAR: 12.6 cm (125 m, 75 m pixels), 95% coverage
Clementine (USA)	5	Moon	1994	Bistatic scatterometer experiment; 6 cm
Cassini (USA)	6	Titan	2004	TRM: 2 cm, SAR (resolution 0.35–1.7 km) and altimeter
Chandrayaan-1 (India)	7	Moon	2008	Forerunner Mini-RF (USA): 12-cm SAR, scatterometer
Lunar Reconnaissance Orbiter LRO (USA)	8	Moon	2008	Mini-RF: SAR (12 cm and 4 cm), imager and interferometer

1. [1. http://www.mentallandscape.com/V_RadarMapping.htm](http://www.mentallandscape.com/V_RadarMapping.htm)
2. [2. http://heasarc.nasa.gov/docs/heasarc/missions/pvo.html#instrumentation](http://heasarc.nasa.gov/docs/heasarc/missions/pvo.html#instrumentation)
3. [3. http://en.wikipedia.org/wiki/Venera_16](http://en.wikipedia.org/wiki/Venera_16)
4. [4. http://www2.jpl.nasa.gov/magellan/](http://www2.jpl.nasa.gov/magellan/)
5. [5. http://filer.case.edu/~sjr16/advanced/20th_close_clementine.html](http://filer.case.edu/~sjr16/advanced/20th_close_clementine.html)
6. [6. http://saturn.jpl.nasa.gov/spacecraft/instruments-cassini-radar.cfm](http://saturn.jpl.nasa.gov/spacecraft/instruments-cassini-radar.cfm)
7. [7. http://www.lpi.usra.edu/meetings/lpsc2006/pdf/1704.pdf#search=%22chandrayaan-1%20radar%22](http://www.lpi.usra.edu/meetings/lpsc2006/pdf/1704.pdf#search=%22chandrayaan-1%20radar%22)
8. [8. http://lunar.gsfc.nasa.gov/missions/scandinst.html](http://lunar.gsfc.nasa.gov/missions/scandinst.html)

The capsule's trajectory was estimated by doppler radio readings and aerodynamic calculations, and by subtracting this from the absolute radar altitude readings, a ground profile could be measured. Readings span a vertical range of 45.5 km down to 0.9 km, during which time the capsule drifted horizontally for a distance of about 60 km. Analysis of the return pulses yielded estimates of elevation variations of the over-flowed surface. *Venera-9/10* (1975) demonstrated the first bistatic planetary radar observations. The *Venera-9/10* orbiters mapped 55 strips of the surface of Venus, ranging from 400–1200 km long and 100–200 km wide. A 32-cm wavelength radio wave was beamed at the surface by the telemetry antenna, and both the direct and reflected signals were recorded by Earth-based receivers. The first analysis of these data gave one-dimensional measurements of terrain shape, with a resolution of 20–80 km.

Pioneer Venus was host to 17 experiments (with a total mass of 45 kg), including a radar altimeter (ORAD), which also produced rudimentary surface maps as the radar beam was scanned in the plane orthogonal to the orbit by the spacecraft's 5 RPM spin-stabilization. The radar package required an average 18 W input power and had a mass of 9.7 kg. Peak transmitted power was 20 W. The X band and S band communications system used a despun antenna (~1 m diameter dish). The radar altimeter provided many years of data with a height accuracy of 150 m, which was the best available information on Venus' surface figure until *Magellan*. The altimeter's waveform strength and shape were analyzed to estimate surface electrical conductivity and meter-scale roughness properties.⁹⁹ The spacecraft's 24-hour orbit was highly elliptical (~200 km periapsis and ~22,900 km apoapsis[†] for most of the mission). Radar data were collected only below 4700 km altitudes, with a resolved footprint on the surface of 23 km along track and 7 km across track.

[†] *Periapsis* and *apoapsis* are, respectively, the points along an elliptical orbit that are closest to and farthest from the gravitational center of the system.

Venera 15/16, simultaneous “twin” missions, were the first space-based SAR mappers of another planet. They imaged the area from the north pole down to about 30°N latitude over 8 months of operations.¹⁰⁰ Their radars had two modes, imaging and altimetry, operating at 8-cm wavelengths. Imaging resolution was ~1 km. Each 4000 kg spacecraft was a cylinder 5 m in length. The synthetic aperture radar antenna was a 6 × 1.4 meter parabolic cylinder reflector, powered by an 80-watt traveling wave tube amplifier. Rather than pulse or chirp modulation, *Venera* used a continuous transmission modulated by a coded sequence of 180° phase shifts. The received signal was digitized into 2540 complex numbers (4 bits I, 4 bits Q). A radar look was taken every 0.3 seconds and stored in a RAM memory buffer. To keep up with this data rate, recording alternated between two onboard tape recorders. Data were downlinked each orbit (~9 MBytes) and then processed in ground-based facilities. Each imaging pass generated 3200 radar images that were combined into a survey strip of 120 km wide by 7500 km long. These were subsequently combined into mosaics. The spacecraft included a 1-m diameter parabolic dish antenna for the radar altimeter. After the orbits were accurately determined, the altimeters were switched to high-resolution mode. A 31-element phase modulation was used, with a height ambiguity of 7.15 km. In later phases of processing, doppler frequency analysis narrowed the effective footprint to 10 km by 40 km. The altimeter operations (interleaved with those of the imager) resulted in the first radar altimetric map (of the northern 1/3) of Venus comprised of more than 400,000 individual measurements. The communications system used a dedicated 2.6 m radio dish antenna. The *Venera* spacecraft were in approximately ~24-hour polar orbits with a periapsis ~1000 km, at 62°N latitude, and apoapsis ~65,000 km.

Magellan mapped over 98% of the surface of Venus (Figure 18.14) with imaging resolution an order of magnitude better than the earlier *Venera* missions.¹⁰¹

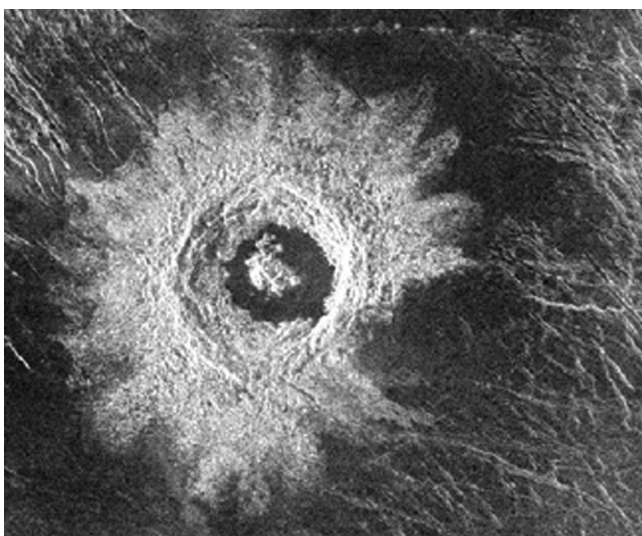


FIGURE 18.14 The impact crater Golubkina on the surface of Venus imaged by *Magellan* (S band, HH-polarized). The 30 km (19 mile) diameter crater is characterized by terraced inner walls and a central peak, typical of large impact craters on Earth, the Moon, and Mars. Rough ejecta give rise to strong radar return, a blessing for those interested in planetary geology. (*Courtesy of NASA*)

Altimetry and radiometry data also measured the surface topography and electrical characteristics. *Magellan*'s elliptical orbit was inclined at 86°, which allowed virtually full access to the surface by the side-looking SAR. By the end of the mission, *Magellan* had returned more data than all prior planetary missions combined. The radar operated in three modes—imager, altimeter, and radiometer—interleaved during each pass.¹⁰² The X band data downlink supported data rates of 268 kbit/s or 115 kbit/s. The 3.7-m diameter high-gain antenna was used for both the radar and for telecommunications. Spacecraft mass was 1035 kg; the radar mass was 335 kg. Input power was 210 W at 28 VDC. *Magellan* operated at S band (2.385 GHz), radiating a peak power of 325 W. Nominal pulse length was 26.5 μsec, with PRF (4400 Hz–5800 Hz) selectable to accommodate the wide variations in range and incidence necessitated by the elliptical orbit. It achieved 150-m resolution in SAR mapping mode, 30-m height resolution in altimeter mode, and 2°C in radiometer mode. All *Magellan* data are available through the Planetary Data System.⁹⁸

Cassini, a multimode radar mapper¹⁰³ leveraged from *Magellan*'s heritage, was included in the 12-instrument payload of the Cassini-Huygens Mission, which was launched in October 1997 and started its four-year tour of Saturn and its moons in July 2004. The motivation for the *Cassini* mapper was the same as that for *Magellan*, namely, to make measurements of the surface of Titan through its dense cloud cover. During its extensive tour of the Saturnian system, the Cassini-Huygens mission was to complete 35 flybys of Titan, of which 29 will be at the closest approach of less than 4000 km, of which 15 will have minimum altitudes of ~1000 km. The first close flyby was in November 2004, from which the first radar images of the surface were collected. The radar antenna uses the 3.66 m H-polarized high-gain telecommunications antenna, a strategy similar to that pioneered on *Magellan*. Seven beams, each at different frequency, width, and boresight orientation, are required to support multiplexed altimetry and scatterometry as well as imaging and radiometry. The radar's mass is ~40 kg, and its input power requirement is ~110 W. Peak data rates are on the order of 360 kbit/s. All modes operate at K_u band (13.8 GHz). In its most favorable lower altitude imaging geometry, ground range and azimuth resolutions are on the order of 0.5 km, at 4 looks. At higher altitudes, more looks are gathered to partially offset the degraded resolution. The radar's noise-equivalent σ^0 ranges from ~−25 dB at low altitude, to ~−8 dB at 4000 km altitude. In contrast to the scheme used on *Magellan*, smaller angles of incidence and lower bandwidth are used for the higher altitudes. The lower bandwidth helps to reduce the mean noise level, whereas the shallower incident angle helps to maintain range resolution with smaller radiated pulse bandwidth.

Clementine, one of the first “faster better cheaper” missions, had primary objectives including laser altimetry and optical surface mapping of the Moon as well as technology demonstration. The main payload instrumentation was comprised of four optical cameras, including one with a laser altimeter. Major new information about the Moon was provided from *Clementine*'s data collected during its 71 days in lunar orbit.

Clementine is relevant to this chapter because of a unique bistatic radar experiment conducted with the S band (13.19 cm) RF data system. The lunar south pole was illuminated by *Clementine*'s communications antenna (6 watts, circularly polarized), and the reflections from the specular point were tracked by an antenna of the Deep Space Network (DSN) over four passes. The observed reflected signal characteristics were consistent with normal lunar regolith[‡] on three passes, but data from the fourth pass

[‡] Found virtually everywhere on the Moon's surface, *regolith* is a layer of granular rocky material covering solid rock.

seemed to show an enhanced strength that corresponded to the specular point passing across the floor of the crater Shackleton.¹⁰⁴ Such enhanced reflections, especially in the “unexpected” sense of circular polarization, are indicative of volumetric radar response from very cold frozen volatiles such as water-ice,¹⁰⁵ best illustrated by Earth-based radar observations of Jupiter’s icy moons. The subsequent claim that water-ice had been discovered at the Moon precipitated wide interest. When independent analyses of the *Clementine* data failed to reproduce the original result,^{106,107} considerable controversy was generated as well. Discovery and/or verification of polar ice deposits on the Moon emerged as a major objective of NASA’s exploration program,¹⁰⁸ and if proven, would be an essential resource for habitable outposts at the Moon.

Radar Exploration for Planetary Ice. Volumetric ice gives rise to two unusual radar responses. When illuminated by a circularly polarized field, the predominant backscatter from most natural surfaces has the opposite sense of circular polarization. In the case of volumetric ice, however, the backscatter has the same sense of circular polarization. The classical measure of this effect is the circular-polarization ratio (CPR), σ_{sc}/σ_{oc} , or “same sense over opposite sense” circularly polarized backscatter strengths.⁹⁷ The total reflected power from volumetric ice is relatively strong, at least for “clean” deposits. Both the polarization and radar brightness effects are explained by the coherent opposition backscatter effect¹⁰⁹ (COBE).

Water-ice was predicted many years ago to have accumulated over some two billion years in the floor of lunar craters or other features whose depth and latitude kept them in permanent solar shadow. The only source of heat for those regions would be background starlight and energy from the Moon’s interior, so that the ambient temperature would be no more than ~75 K. As water-ice enters such a cold space from comets, it accumulates. This process generally is accepted as an explanation of the radar-bright response from Mercury’s polar craters, for example, as observed by Earth-based radar telescopes. Due to the small axial tilt of the Moon, however, radar telescopes such as Arecibo have no similar opportunity to explore the floors of the lunar polar craters.

The problem is that relatively large CPR is not unique to volumetric ice deposits. Dihedral (two-dimensional) corners also reflect most strongly in the same sense as the incident circular polarization. Naturally occurring dihedrals, such as rough rock formations created by a large impact, could generate false water-ice signatures. To reduce the potential ambiguity of CPR and brightness measurements, the radar observations must be repeatable and should be correlated with other indicators.

Chandrayaan-1 and the *Lunar Reconnaissance Orbiter (LRO)* include in each of their payloads a “Mini-RF” radar.¹¹⁰ The version for Chandrayaan-1 is at S-band (12-cm wavelength), with 150-m resolution at 16 looks. The Mini-RF for LRO has two frequencies, S band (12 cm) and X band (4 cm), and two resolutions, 150 m at 16 looks, and 15 m at 8 looks. The LRO radar also includes an interferometric mode, which requires a continuous PRF, in contrast to the burst plan used for the other modes. Both have moderate incident angles (~45 degrees), moderate swath widths (4 km to 8 km), and operate from low altitudes (100 km and 50 km, respectively). Given the applicable small range-velocity product (Table 18.1), the antenna area needs to be only ~1 m² to satisfy the minimum area constraint (Eq. 18.4). These radars are indeed low mass, at about 8 kg and 12 kg, respectively, including in each case their antenna.

A major objective for both of these radars is to look for evidence of ice deposits in the permanently shadowed areas of the Moon’s polar regions. This requires that they must measure the circular polarization ratio (CPR). Hence, they transmit circular polarization, and they are dual-polarized on receive. Their antennas are comprised of passive arrays of H- and V-polarized elements, driven simultaneously 90° out of

phase so that the radiated polarization is circular (either left or right). The received linear polarizations are maintained through the remainder of the system to the image processor output products. This results in the hybrid-polarity architecture¹¹¹ that is outlined below.

Magellan: Innovative Venus Mapper. Magellan (Figure 18.15) had to face up to two driving mission restraints: cost and data rate. The first was set by NASA and the U.S. government budget authorities. The second was set by physics, conditional upon the data-rate capabilities of the Deep Space Network.¹¹² The lesson, of course, is that it is not enough to do good (read “big budget, SBR-based”) science, it must be done efficiently and relatively patiently. In the case of *Magellan*, however, these top-level restraints motivated a superb innovative radar design.

Cost. There were several consequences to the severe reduction in approved funds relative to funds requested for the original Venus Orbiting Imaging Radar (VOIR) mission. Rather than a conventional circular orbit, *Magellan* was redesigned for an elliptical orbit (Figure 18.16), which had considerably less associated costs and risk. Also, rather than the original large high-aspect-ratio antenna typical of space-based SARs, *Magellan* was obliged to use a spare circular communications antenna left over from a previous mission. Whereas these may sound like benign if not trivial modifications, they necessitated paradigm-shifting innovations by the SAR design team.

Antenna. The key element in any space-based SAR design is the antenna. It determines range swath coverage and required minimum transmitter power, and has a major influence on resolution and data rate. The Magellan antenna, a 3.7-m diameter dish, was a significant departure from the conventional highly asymmetric rectangular antennas that were then in favor for SARs.

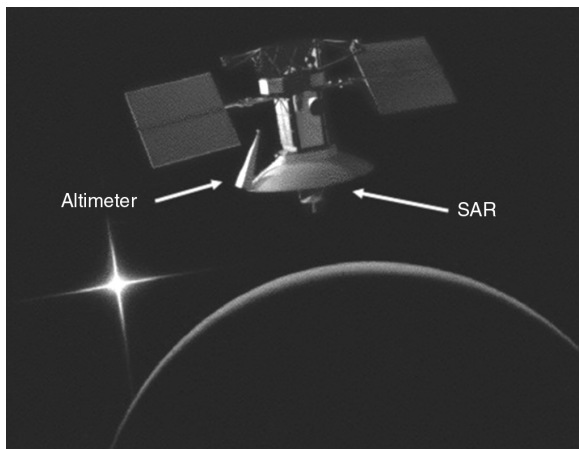


FIGURE 18.15 Artist's impression of Magellan observing the surface of Venus, backlit by the sun, featuring the radar (and high-gain communications) antenna and the smaller horn antenna for the altimeter (*Courtesy of NASA*)

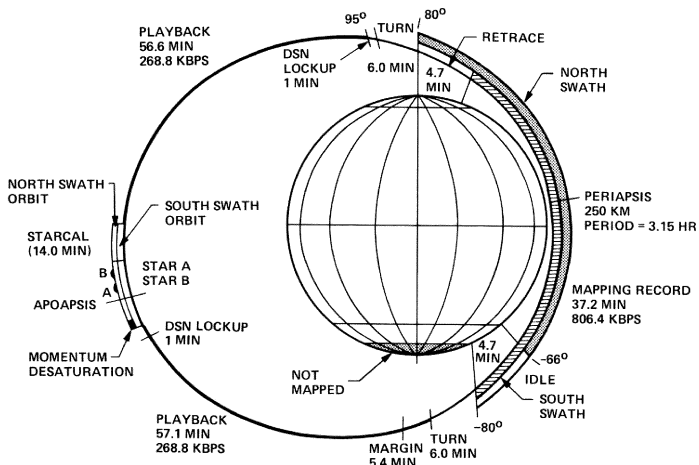


FIGURE 18.16 Details of *Magellan's* elliptical orbit, dominated by ~37 minutes of data take and 2 hours of data downlink during each 3.3-hour orbit period (*Graphic courtesy of NASA*)

The vertical dimension of the antenna (together with range, incidence, and wavelength) determined the width of the illuminated swath on the surface. This provided an upper bound on the imaged swath width, which, in the case of *Magellan*, was less than the swath actually illuminated. The imaged swath width was chosen to be somewhat wider than the orbit-to-orbit translation of Venus' surface due to planet rotation. The period of the elliptical orbit was selected to be about three hours, so that in succession each imaging pass overlapped and extended the surface imaged on previous passes.

In the along-track direction, the antenna size had far-reaching consequences. The theoretical (single-look) azimuth resolution available from the *Magellan* antenna could be about 1.6 meters (Section 18.2). This is on the order of 75 times smaller than the science requirement of 120 meters azimuth resolution. It followed that single-look 120-m data could be collected by operating the radar only 1/75 of the time. If N_L looks were required, then the implied operating duty factor would be $N_L/75$, larger by a factor of N_L . The result is the burst mode (Section 18.2), in which the radar operates at much less than 100% of the time. Burst mode is a standard strategy for SARs designed to explore the Moon or other planetary bodies, using antennas whose along-track dimension is much smaller than the azimuth resolution required of the data. The looks parameter N_L deserves special comment in the SBR context, summarized below.

The *Magellan* antenna was used as the high-gain antenna for data downlink as well as for the SAR. During the high-altitude segment of each orbit, the spacecraft was oriented to point the antenna toward Earth. The antenna had two feeds, one at S band (HH-polarization for the radar) and X band (circular-polarization for telemetry). After each pole-to-pole data collection, the telemetry transferred the accumulated data to one of the three Deep Space Network (DSN) receiving stations, so that, in consequence, the data dump kept pace with the data take, per orbit.

Orbit. For reasons directly attributable to principles of orbital mechanics, it was much less costly to go into an elliptical orbit at Venus rather than a circular one. The fact that it would be considerably more difficult to get decent imagery successfully

from an elliptical orbit was of little concern to the budget-masters, although the elliptical orbit constraint attracted more than a little attention from the SAR design team. The *Magellan* radar had to adapt to variations in relative altitude from approximately 250 km (near the equator) to more than 2000 km (over the poles). Quite reasonably one might expect that the resulting imagery—let alone the implied timing and scaling issues—would suffer as a consequence. Thanks to the mission design, however, *Magellan* image quality is surprisingly consistent, pole to pole. The reasons provide an important object lesson.

Since the Magellan radar was operated in burst mode, it was convenient (as well as necessary) prior to each burst to set the mode parameters, which, in general, varied from burst to burst. Critical parameters included PRF, range gate, burst length, burst period, and spacecraft roll. The parameter files were prepared in advance, based on the data collection geometry, and turned into commands to be generated by the radar mapping sequencing software. The result was a set of about 1000 unique configurations, each tied to specific segments of the orbit. In operation, suitable commands were pre-loaded into the onboard SAR control processor for each three-day mapping interval.

In order to offset the tenfold altitude change on SAR image quality, the SAR operating profile was designed to exploit a variety of incident angles. At the start of each imaging pass at high altitude, the incidence was slewed from steep near the pole, to shallow in the neighborhood of the equator, back to steep when approaching the opposite pole. This incidence variation helped to offset the large change in radar range to the imaged swath, but it meant also that the range resolution as expressed on the surface varied as a function of latitude. For a constant radar bandwidth, the effective surface range resolution at shallower incidence is improved over that achieved at steeper incidence. Fortunately, at steeper incidence, and hence at longer ranges, there was more time available to gather more looks.

Image Quality. Looks and resolution work together to determine the image quality (read “geophysical information potential”) of SAR imagery over natural terrain composed of distributed scatterers. The governing expression is the SAR image quality parameter^{31,113}

$$Q_{\text{SAR}} = \frac{N_L}{r_{\text{Rg}} r_{\text{Az}}} \quad (18.18)$$

where N_L is the number of (statistically independent) looks, and r_{Rg} and r_{Az} are the range and azimuth resolution, respectively, on the surface. Here the important generalizable lesson is that an increase in number of looks can be applied to offset a decrease in range resolution (within reason and in this kind of exploratory space-based SAR data). Note that both looks and resolution require support in bandwidth. It follows that Q_{SAR} is proportional to the product of the range and azimuth bandwidths, hence proportional to the (two-dimensional) information capacity of the radar in the Shannon sense. This principle was applied with great profit to the *Magellan* SAR design,¹¹⁴ as illustrated by Table 18.7. From that table, one can verify that the image quality of *Magellan* data varied by no more than $\sim \pm 2\%$ pole to pole, in spite of large variations in radar range, incident angle, and ground range resolution.

Data Rate. *Magellan* SAR data were relayed from Venus to Earth via the DSN. This major communication system imposed a working limit of about 270 kbit/s on the SAR data telemetry. Whereas this may seem rather large, it is minuscule by

TABLE 18.7 Image Quality: Magellan Resolution and Looks

Altitude (km)	Incidence (degrees)	r_R (m)	r_A (m)	Looks NL	$Q_{\text{SAR}} N_L / (r_R r_A)$
250	52	110	122	4.8	3.6×10^{-4}
500	39	137	121	6.0	3.6×10^{-4}
1000	28	181	121	8.5	3.9×10^{-4}
1750	21	247	120	11.6	3.9×10^{-4}
2100	19	270	120	13.5	4.0×10^{-4}

space-based SAR standards. For example, the digital data rate for the ERS-1/2 and RADARSAT Earth-observing SARs is on the order of 120 Mbit/s. Newer designs claim up to 400 Mbit/s. Since the *Magellan* objective was to image a substantial portion of the surface of the entire planet at 120-m resolution within the length of the primary mission, the DSN data-rate capability emerged as the toughest requirement on the entire system.

Raw SAR data rate is proportional to the image quality factor, swath width, space-craft velocity, and the number of digital bits per data sample. Of course, mean data rate can be relaxed if the data from any given pass can be collected and then played back at a slower rate. Although this strategy was exploited by the *Magellan* design, tolerance for which was set up by the elliptical orbit, it was not sufficient to solve the limited data-rate problem.

The only degree of freedom remaining in the data-rate budget was the number of bits retained for each sample in the raw SAR datastream. Working back through the DSN constraint, it turned out that there were only two bits available for *Magellan*'s raw SAR data.

Yes—a 2-bit SAR! And again, the unique characteristics of an orbital SAR made this an acceptable solution for the *Magellan* design. The key requirements for this paradigm are two: (1) an effective signal encoding that is very large and (2) an imaging environment that is dense and dominated by distributed random backscatter. Planetary SARs (and many Earth-observing space-based radars) easily satisfy these requirements. One measure of an imaging radar's extensive signal encoding is the product of its range and azimuth time-bandwidth products, or equivalently, its potential two-dimensional compression ratio. In the case of SAR data, this ratio is given by the area of the instantaneous pulse footprint (antenna width by projected pulse length) divided by the resolved cell area (the product of azimuth and range resolution). This ratio varied by mode for *Magellan*, but, in general, was well in excess of 10,000, which turns into a gain in dynamic range from the signal domain to the image domain of 40 dB.

The “2-bit method” was based on a Block-Adaptive Quantizer¹¹⁵ (BAQ). This in effect implemented an automatic gain control (AGC) that selected the most influential digital samples (bits) from the raw SAR datastream. As designed for *Magellan*, the data were digitized into 8 bits, in-phase and quadrature (I&Q). The analog-to-digital stage was followed by the BAQ operation, which selected the two most significant bits in each (I&Q) data pair, relative to a mean signal level that had been established from the previous burst of received data. The mean signal level varied very slowly burst to burst since adjacent bursts covered essentially the same scene elements. The mean signal level (AGC setting) was included in the header for each burst's data record to be used in subsequent SAR image formation.

Although the dynamic range of the raw SAR data out of a BAQ operator is severely limited, the potential dynamic range of the resulting image data is much larger: it is bounded above by the product of the input dynamic range and the two-dimensional compression ratio of the SAR data. Thus, the dynamic range capacity after processing for *Magellan* imagery was in excess of 40 dB. This was well illustrated in the many thousands of image frames formed from *Magellan*'s SAR data.

Hybrid-polarity Architecture. A leading high-level objective of a radar destined for the Moon, Mars, or any other planetary body is to maximize its measurement potential, while also minimizing its resource demands (principally power and mass). If sensitivity to frozen volatiles is a requirement levied on a planetary exploratory radar, then the system should be dual-polarized and must transmit circular polarization. As reviewed in Section 18.2, a dual-polarized radar maximizes its measurement capabilities only if it retains the relative phase as well as the magnitudes of the two received amplitudes, such as E_H and E_V in the linear polarization basis. It has been known since 1852 that a quasi-monochromatic EM field can be fully characterized by the four Stokes parameters.¹¹⁶ In terms of linearly polarized received data, the Stokes parameters are

$$\begin{aligned} S_1 &= \langle |E_H|^2 + |E_V|^2 \rangle \\ S_2 &= \langle |E_H|^2 - |E_V|^2 \rangle \\ S_3 &= 2 \operatorname{Re} \langle E_H E_V^* \rangle \\ S_4 &= -2 \operatorname{Im} \langle E_H E_V^* \rangle \end{aligned} \quad (18.19)$$

where * denotes complex conjugate, and the carats < > indicate an average taken over several samples. Clearly, the relative phase between the two polarizations is an essential factor for two of the four Stokes parameters. Data expressed through the Stokes parameters are well-suited to being exploited by matrix decomposition methodology.^{60,117}

For a given transmitted polarization, the values of these Stokes parameters are invariant with respect to the polarization basis of the receiver. It follows that the optimum architecture is hybrid-polarity¹¹⁸: circularly polarized on transmit and linearly dual-polarized on receive (Figure 18.17). This architecture requires less mass and offers greater efficiency than alternatives, while capturing all of the potential information in the backscattered field.

An antenna comprised of two linear arrays (such as H and V) will radiate a circularly polarized field if the sets of elements are driven simultaneously and 90° out of phase, as shown in Figure 18.17. In practice, the amplitude weighting and relative phasing of the arrays will seldom be perfect. As a result, the radiated field will be somewhat elliptical, rather than purely circular. The hybrid-polarity architecture is self-calibrating and, therefore, relatively robust in response to such imperfections. In brief, under the condition that $\sigma_{HH}^0 = \sigma_{VV}^0$ the mean signal level in the two receive channels should be equal. (In terms of the Stokes parameters, $S_2 = 0$). The H and V backscatter coefficients will always be equivalent when the radar's illumination is perpendicular to the surface. Hence, any hybrid-polarity radar can set up this condition by the simple expedient of looking down on a horizontal surface during a calibration exercise. Discrepancies in either amplitude or phase will be evident from such data collected over a random distributed scene. There is no need for a known point-target reference in the field of view. The Stokes parameters that correspond to such measurements are sufficient to characterize the relative H/V phase of the transmitted field, as well as that of the receivers.

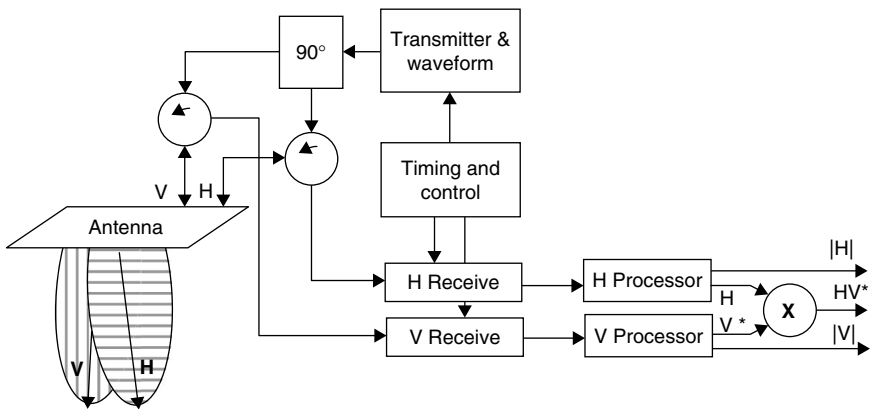


FIGURE 18.17 The hybrid-polarity SAR architecture first used by the Mini-RF lunar radars on *Chandrayaan-1* and *LRO*

18.5 SCATTEROMETERS

Space-based remote sensing scatterometers measure the normalized backscatter with sufficient precision and accuracy to deduce the value of one or more parameters of geophysical significance. For example, the power reflected from the ocean back to a radar is a function of surface roughness at the scale of the radar's wavelength, which, in turn, is a function of the local wind.¹¹⁹ Estimation of wind speed and direction over the open ocean is the most common application for these instruments. A wind scatterometer was adopted by EUMETSAT in the early 2000s as a required operational capability, with operational accuracies of ± 2 m/s in wind speed and $\pm 20^\circ$ in direction. In addition to open ocean observations, calibrated data from this class of SBR have been applied to a variety of large-area surface features, such as determination of sea ice coverage, mapping the boundaries between the principal ice zones of Greenland, or global estimation of tropical deforestation. In all such applications, the emphasis is on measurement of mean reflectivity over large areas, rather than mapping fine spatial detail. These radars typically have resolutions on the scale of 10s of kilometers, supported over swaths of 1000 kilometers or more.

In the ocean application, relatively small changes in radar backscatter may correspond to substantial differences in the retrieved wind information.^{§120,121} It follows that the dominant requirement for this class of radar is the accuracy and precision of the received power measurement.* However, the next step, vector wind retrievals—transforming the radar backscattered power into accurate estimates of wind speed and direction—is far from trivial. Indeed, the technique fails for the very low wind speeds that do not generate wavelength-scale surface roughness. In the limit,

§ http://www.eumetsat.int/groups/ops/documents/document/pdf_tm03_rev-scatterometer-w.pdf

* Note that both accuracy and precision are required. Radar backscatter by its very nature is a quantity having a large standard deviation that can be reduced only by extensive averaging. Because the geophysical interpretation of scatterometric data often depends on distinguishing between two similar values of σ^0 , the results depend critically on reducing the uncertainty in the estimated value as well as getting the average value right.

an oblique-viewing radar such as a scatterometer will generate virtually no backscatter from the sea surface in the absence of wind-driven waves, even if there is a substantial swell in the region.

Vector Wind Retrieval. The normalized backscatter coefficient σ^0 from a wind-roughened oceanic surface depends foremost on the radar's wavelength, the local angle of incidence, and the polarization, respectively. The wind parameters to be estimated are its speed, the relative angle in the horizontal plane between the wind direction, and the radar line-of-sight. The ocean's reflectivity is also a function of other factors, including surfactants (such as oil slicks, either natural or anthropogenic), the air-sea temperature difference, or the presence of large waves such as oceanic swell, but these are of less significance for the present discussion.

The reflection coefficient σ^0 is nonlinear with respect to the wind parameters. Figure 18.18 illustrates the response for one polarization, where the horizontal axis is the relative wind direction, and the vertical axis is the normalized radar cross section. The several curves each correspond to a specific wind speed. In general, upwind and downwind aspects provide stronger backscatter than cross-wind, and the upwind aspect usually is a bit stronger than downwind. Wind vector data have been collected by airborne scatterometers flying in circles (literally!) over instrumented test sites.¹²² There have been many attempts over the years to converge on a suitable mathematical model for this behavior, with reasonable success.¹²³ There are several vector wind retrieval methods in current use, including CMOD-4 and a neural network model.

The data clearly show that measurement of radar backscatter at only one aspect angle is not sufficient to determine wind speed and direction. The Seasat scatterometer used two look angles (separated by 90°), but the resulting retrievals had as many

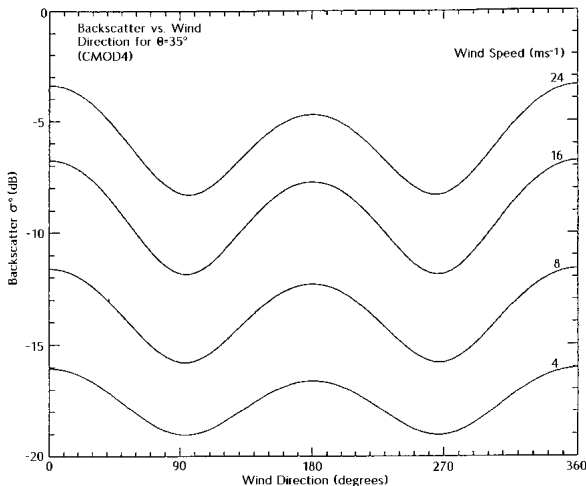


FIGURE 18.18 Typical backscatter strength (vertical axis) from a wind-driven sea surface, as a function of wind speed (modeled data) and the wind direction relative to the radar's look direction (horizontal axis). Similar families of curves correspond to the radar's polarization (usually HH or VV) and angle of incidence. Curves such as these are derived from a model (such as CMOD4) subsequently verified by extensive airborne measurements.

four potential solutions, which presented as directional ambiguities.¹²⁴ Space-based wind scatterometers are characterized by differing viewing geometries, each motivated by the need to suppress directional ambiguities, within the constraint of a physically (or financially) feasible implementation.

Measurement Precision. Clearly, σ^0 must be measured with an accuracy and precision of less than 1 dB if useful wind retrievals are to be derived. Accuracy depends on the radar's stability and its calibration. The challenge for space-borne scatterometry is to design the radar such that the precision—the normalized standard deviation of the σ^0 measurements—is sufficiently small. In the standard terminology of scatterometry, the classical parameter is K_p , the normalized standard deviation of the measurement.¹²⁵ In the case of a fan-beam scatterometer that employs doppler filtering, the governing expression is

$$K_p = \frac{(1 + 2 / SNR + 1 / SNR)}{\sqrt{NTB}} \quad (18.20)$$

where N is the number of statistically independent pulses summed into each σ^0 measurement, T is the transmitted pulse length, B is the doppler bandwidth of the measurement cell, and SNR is the signal-to-noise ratio. K_p usually is cited as a percent, where values of 5% or better are the objective. Note for high SNR that K_p converges to $1/\sqrt{NTB}$. At lower wind speeds K_p depends on SNR as well as on the number of statistically independent looks. The details of any expression such as this depend on the underlying statistical model, which is gaussian in this classic expression. However, the general principle is that the scatterometer must provide many independent looks to reduce the standard deviation of the σ^0 measurement, regardless of the statistical distribution of the ocean's backscatter.

Trends. Vector wind data have been adopted by operational meteorological agencies such as EUMETSAT. It is likely that space-based microwave assets will continue to be used for the foreseeable future to provide these data. The success of SeaWinds (discussed later in this section) suggests that the conical scan paradigm will be the basis for future vector wind scatterometer design.

That said, there are two space-based alternatives for measuring vector winds by microwave means, active and passive. Radars often are unpopular on spacecraft that host other instruments, of which some may be compromised by radio frequency interference (RFI) generated by a nearby microwave transmitter. Radars also require more power from their host spacecraft than passive systems. These and related considerations motivated the development of WindSat, a passive instrument that estimates near-surface vector winds by Stokes parameter analysis of the microwave emissivity from the ocean surface.¹²⁶ WindSat is one of two instruments aboard the *Coriolis* satellite, launched in 2003. The operational reliability of passive-vector wind data relative to scatterometric measurements remains an open issue.

Scatterometric data are being exploited for many purposes other than oceanic vector winds. Although the “images” generated by a space-based scatterometer may have only 50-km resolution, their wide swath and frequent revisit intervals are well suited to synoptic coverage of global-scale phenomena. The multi-year history of scatterometric radars provides an important data set for climate change studies as well as monitoring seasonal variations. Suitable applications include sea ice cover, large icebergs, continental ice sheets, vegetation, and soil moisture.^{127–130}

Flight Systems. *RadScat*¹³¹ (Table 18.8) was the name given to the radiometer/scatterometer portion of the S-193 Ku band instrument aboard Skylab. The top-level objectives of this experiment were (1) to provide the near-simultaneous measurement of microwave backscatter and emissivity of land and ocean on a global scale and (2) to provide engineering data for use in designing space radar altimeters. The equipment shared a common gimballed antenna. The scatterometer measured the normalized backscatter coefficient of ocean and terrain as a function of incidence ranging from 0° to 48°. Although only sparse coverage of selected sites was possible, the data were sufficient to demonstrate the potential of space-based radar measurement of surface wind vectors over the ocean. The S-193 zone of access was 48° forward and 48° to either side of the spacecraft ground track. For selected measurements, the beam was pointed in the along-track direction to fixed angles of 0°, 15.6°, 29.4°, 40.1°, and 48°, with sufficient dwell time at each angle to permit averaging to achieve approximately 5% precision. RadScat data collected over the Amazon rain forest suggested that the uniformity of the observed backscatter would be a stable calibration reference for space-based radars, which has since been validated as a standard technique.¹³²

SASS, the Seasat-A Satellite Scatterometer,^{133,134} was the first space-based radar designed specifically to measure oceanic winds. It was a multi-fan-beam instrument, comprised of two sets of two dual-polarized antennas (HH and VV), each ~3-m in length whose fan-shaped beams pointed to 45° and 135° to either side of the orbit plane. Incidence spanned 25° to 55°, covering a 500-km wide swath on each side. Calibration data taken over the rain forest were used to reduce antenna gain uncertainty to less than 0.4 dB. Since Seasat was not yaw-steered, the fore and aft footprints were misregistered due to Earth rotation, which reduced the useful swath at lower latitudes to about 400 km. The value of K_p varied from 1% to 3% over the ocean under moderate to high sea states, but degraded to 15% for lower wind speeds and to 50% for very low backscatter from non-oceanic surfaces. The accuracies of wind speed and direction over 4–16 m/s were ±2 m/s and ±20°, respectively. The data were not sufficient to avoid directional ambiguities, however. Nominal resolution was 50 km, determined by the intersection of the antenna pattern and iso-doppler contours. The radar operated at 14.6 GHz, radiating a peak power of 100 W at 17% duty factor from a traveling wave tube amplifier (TWTA). The waveform was modulated CW. The receiver front end was a tunnel diode amplifier, which maintained the noise figure to be less than 5.7 dB at all operating temperatures. Mean input power was 136 W dc; the instrument mass was 102 kg.

TABLE 18.8 Scatterometers

Name	Spacecraft	Country	Year	Antenna	Band	Polarization
RadScat	Skylab	USA	1973, 1974	Pencil beam	Ku	VV, HH
SASS	Seasat	USA	1978	Fanbeams	Ku	VV, HH
ESCAT	ERS-1	Europe	1992-6	Fanbeams	C	VV
ESCAT	ERS-2	Europe	1995-	Fanbeams	C	VV
NSCAT	ADEOS I	US/Japan	1996–1997	Fanbeams	Ku	VV, HH
SeaWinds	QuikSCAT	US	1999–	Conical scan	Ku	VV, HH
SeaWinds	ADEOS II	US/Japan	2002–	Conical scan	Ku	VV, HH
CNSCAT	SZ-4	China	2003	2 conical scan	Ku	VV, HH
ASCAT	MetOp-1	Europe	2006	Fanbeams	C	VV
Scat	Aquarius	USA	2009	3-beam push	L	VV, VH, HV, HH

WS aboard the ERS-1 and ERS-2 spacecraft of ESA denotes the scatterometer mode embedded in their C band AMI radar instrumentation.¹⁴ These scatterometers used three fan-beam antennas, whose footprints were oriented at 45°, 90°, and 135° with respect to the satellite track. The two outer antennas are 3.6-m long. Note that the spacecraft had to be yaw-steered to maintain this footprint geometry over the rotating Earth. The C band operating frequency, although a departure from space-based precedent, resulted from use of the same RF hardware as the SAR mode. As a consequence, simultaneous SAR and scatterometer operations were not possible. In contrast to K_u band, the C band data were less degraded by rain and proved to be more reliable for higher wind speeds.¹¹⁹ The antenna swaths spanned 500 km, from which the averaged data from the three-look directions were colocated into 50-km resolution cells, posted on a 25-km grid.

ASCAT, the Advanced Scatterometer¹³⁵ aboard MetOp-1, is essentially an improved version of the ERS-1/2 instruments. It is a stand-alone radar designed for operational use; it does not have to time-share onboard electronics as was the case with the scatterometer in the AMI suite. It covers swaths on both sides of the satellite ground track. The near edge of these 500-km swaths are offset 384 km from nadir, spanning 25°—65° incidence. The 0.57 dB radiometrically accurate data are averaged to achieve K_p from 3% (high up-wind speed) to 10% (low speed, cross-wind aspect). The resulting vectors for near-surface winds cover 4–24 m/s with accuracy ±2 m/s and ±20°. The radar operates at 5.255 GHz, radiating 10 ms linear frequency-modulated (LFM) pulses at 120 W peak power from combined GaAs FET devices. Only one antenna is active (for 0.2 s) at a time; the operation cycles around the six antennas in sequence. The instrument mass is 270 kg; input power required is 251 W. Thanks to onboard processing, the inherent data rate is reduced from 1.4 Mbit/s to an average of 60 kbit/s to the MetOp-1 payload data-handling system.

NSCAT, the NASA Scatterometer,¹³⁴ provided to Japan as part of the Advanced Earth Observing Satellite (ADEOS) payload, was an upgraded version of SASS. NSCAT used six dual-polarized stick antennas (3 m long), four of which were aimed at ±45° (H polarized) and ±135° (Vpolarized) from the surface track, and the two midbeam antenna patterns were aligned at 65° and 115° (each H and V polarized). The third beam on each side helped to remove the fourfold directional ambiguities that plagued SASS wind retrievals. Two 600-km wide swaths were covered, at 25-km resolution. In order to support 25-km along-track resolution, the radar's sequencer had to cycle through all antenna patterns within 3.74 s, resulting in a maximum dwell time of 470 ms within each of the eight footprints. Cross-beam resolution was determined by doppler analysis. However, since the mean doppler offset was a function of antenna orientation (as well as incidence), the return from each direction needed its own LO offset. The antennas' peak gain was 34 dB, directed toward maximum range. NSCAT's mass was 280 kg; required input power was 275 W. The RF system was built around redundant TWTAs, transmitting modulated 5-ms pulses at a PRF of 62 Hz, peak power 110 W.

SeaWinds marks a significant departure from the “stick antennas” of prior wind scatterometers, relying instead on a dish antenna¹³⁷ rotating at 18 RPM to sweep its two beams over a nadir-centered swath 1,800 km wide (Figure 18.19). The first SeaWinds mission was aboard QuikSCAT, mobilized by NASA and launched in June 1999 as a rapid response to the premature loss of ADEOS in June 1997. The second SeaWinds was embarked on Japan's ADEOS-II. Both instruments operate at K_u band (13.4 kHz), radiating 110 W, 1.5 ms pulses at 190 Hz PRF, split equally between the two antenna beams. The transmitter is a TWT, based on NSCAT heritage. The modulated pulse bandwidth is 40 kHz, which is maintained within an 80 kHz filter in the receiver. The received data must be compensated to offset the doppler shift, which varies



FIGURE 18.19 The Seawinds scatterometer, as embarked on Japan's ADEOS-II spacecraft. The radar drives the conically scanned reflector antenna, which takes up most of the real estate on the Earth-viewing face of the satellite.

sinusoidally over 1 MHz during each antenna rotation. Instrument mass is 191 kg; required input power is 217 W. These numbers illustrate the principal advantages of the architecture, providing greater coverage with less mass and power, in contrast to the stick-antenna architecture.¹³⁸ System sensitivity accommodates σ^0 in the range -37 dB to -2 dB. The antenna is a 1-m reflector (gain ~ 40 dB), with two feeds, resulting in a pair of pencil beams at 46° (H polarization) and 54° incidence (V polarization). The illumination geometry also is advantageous because the incidence is the same for all aspect angles. The beam-limited footprints are approximately 30 km by 40 km. Following onboard processing, the average data rate is 40 kbits/s. SeaWinds performance¹³⁹ is at least comparable to other wind scats, wind speed and direction accuracy being 3 m/s to 20 m/s at 2 m/s and 20° , respectively. Nominal surface resolution is 50 km; advanced processing¹⁴⁰ reduces this to ~ 25 km. Although the swath is 1800 km wide, the variety of aspect and polarization coverage limits the science-compliant wind vector retrievals to strips from 250 km to 800 km either side of the ground track.

Aquarius. The *Aquarius* mission is designed to map sea surface salinity, for which L band radiometric sensing of the ocean's emissivity is the primary measurement. However, emissivity is a function of the roughness of the surface,¹⁴¹ as well as its temperature and dielectric constant, which is the variable of interest. The *Aquarius* payload includes an L band (1260 MHz) scatterometer to measure surface roughness. The scatterometer and radiometer share the same 2.5-m diameter reflector illuminated by three offset feeds, which generate three side-looking beams (at 29° , 38° , and 45° , incidence), thus sweeping out strips of coverage as the spacecraft moves along its orbit. The scatterometer is fully polarized (HH, HV, VH, and VV). Peak transmitted power is ~ 250 W, pulse length is 1 ms, sufficient to support sea surface σ^0 over the range 0 dB to -40 dB. Resolution is modest, at ~ 150 km. The scatterometer and radiometer share electronics. Combined instrument mass is ~ 400 kg, and required prime power is ~ 450 W.

18.6 RADAR SOUNDERS

In its most general form, a radar sounder is a device whose transmissions are designed to penetrate the volume of a target medium, from which the waveform of the resulting backscatter indicates variations in dielectric contrasts as a function of depth.[†] As a sounder passes over an illuminated region, the sequence of ranging waveforms generates a profile, which is a two-dimensional reflectivity cross section of the surveyed volume. Penetration depth in general increases with wavelength and also with radiated power. On the other hand, reflectivity depends on the dielectric contrasts between internal layers; a material's dielectric constant is also a function of wavelength. It follows that space-based radar sounders must choose a frequency and bandwidth that balance the often conflicting requirements of penetration, reflectivity, and resolution, under the constraints of available power and antenna aperture.

The space-based radar sounders highlighted in Table 18.9 fall naturally into two groups: subsurface and atmospheric/ionospheric. It is evident that the subsurface sounders all are at relatively low frequency, in contrast to the atmospheric sounders at much higher frequency. The ionospheric sounding mode of MARSIS is a special case, elaborated below.

Subsurface Sounding–flight Systems. Subsurface sounding from a space-based radar is considerably more challenging than from a surface-mounted GPR (Chapter 21) or a very low altitude aircraft. Of course, once radar signals penetrate the surface, the usual volumetric attenuations and reflections occur. As with any GPR, large dynamic range is required, since the signals of interest may be weaker than competing returns by 50 dB or more. Radar sounding to appreciable depth is possible only in dry materials such as lunar regolith or in very cold low-loss ice.

TABLE 18.9 Radar Sounders

Instrument	URL	Spacecraft	Years	Objective	Frequency
ALSE	1	<i>Apollo-17</i>	1972	Lunar subsurface	5, 15, 150 MHz
MARSIS	2	<i>Mars Express</i>	2003–	Mars subsurface	1.8, 3, 4, 5 MHz
SHARAD	3	<i>MRO</i>	2005–	Mars subsurface	15 - 25 MHz
LRS	4	<i>SELENE</i>	2007	Lunar subsurface	5 MHz
PR	5	<i>TRMM</i>	1997–	Rain	13.8 GHz
MARSIS	6	<i>Mars Express</i>	2003–	Mars ionosphere	0.1–5.4 MHz
CPR	7	<i>CloudSat</i>	2006	Earth cloud profiles	94 GHz
DPR	8	<i>GPM</i>	–	Rain	13.6, 35.5 GHz

1. <http://nssdc.gsfc.nasa.gov/database/MasterCatalog?sc=1972-096A&ex=4>

2. <http://sci.esa.int/science-e/www/area/index.cfm?fareaid=9>

3. <http://mars.jpl.nasa.gov/mro/overview/>

4. http://www.jstfw.info/selene_sympo/en/text/overview.html

5. <http://trmm.gsfc.nasa.gov>

6. <http://sci.esa.int/science-e/www/area/index.cfm?fareaid=9>

7. <http://cloudsat.atmos.colostate.edu/>

8. <http://gpm.gsfc.nasa.gov/dpr.html>

[†] The term *sounder* usually associated with acoustic echo sounding, derives from many centuries of oceanic depth measurements using lead lines and the like. The logical extension from acoustic to electromagnetic methodology is a small step in comparison.

In addition to the usual GPR considerations, two space-specific issues arise, neither of which can be solved by the usual expedient of increasing the radar's transmitted power. The first problem is clutter. From orbital altitude, scatterers on the surface far from nadir may generate strong backscatter that appears at the same radar range as the signals reflected from depth, as suggested in Figure 18.20. The problem is compounded with increasing altitude and by the fact that at the long wavelengths required for deeper penetration, the size constraints on a spacecraft-mounted antenna dictate that the illumination pattern will have little or no directivity. Processing over groups of returns to reduce the effective width of the beam can be helpful. Doppler-based techniques are applicable to the along-track direction.¹⁴² However, the orbit's altitude-velocity parameter (Table 18.1) may be so large that the available ambiguity-free range-doppler window is too small to be useful. Narrowing the effective antenna pattern in the cross-track direction presents even more of a challenge.

The second problem is range sidelobes. From orbital altitudes and from a realistic spacecraft, it is not feasible to transmit a simple short pulse that has sufficient energy to generate useful reflections from depth. Long modulated pulses are the only practical method. Unfortunately, the specular component of surface reflection usually is very strong at the long wavelengths required for subsurface sounding. Pulse compression of the surface return generates range sidelobes which appear at depths that could easily overwhelm the weaker reflections from the internal structure. The standard strategy to mitigate this problem is rigorous sidelobe control, requiring severe pulse amplitude weighting and strict control of phase and amplitude linearity.

Due to the large footprint of a space-based sounder, and the need to salvage all possible contributions of signals from depth, it is standard practice to assume that the dominant in situ returns arise from specular scattering, hence from extended horizontal layers.¹⁴³ The contributing area is determined by the radius r_F of the first Fresnel zone, $r_F = \sqrt{h\lambda/2}$ in free space, where h is the altitude of the radar above the surface. The radius is somewhat larger within the medium, since the spherical wavefront is flattened due to the slower speed of in situ propagation.

ALSE. The Apollo Lunar Sounder Experiment^{144,145} was a combination imager and sounder, operating at wavelengths of 60 m, 20 m, and 2 m. The ALSE sounder

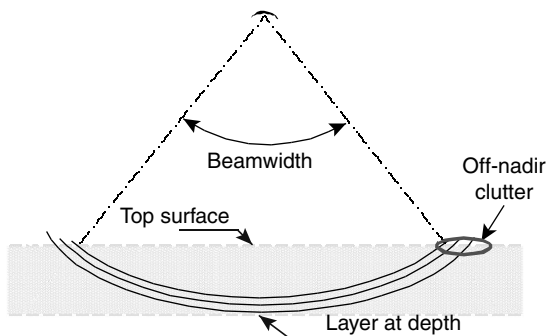


FIGURE 18.20 Two problems that challenge space-based subsurface sounding are (1) range-coincident competition between the desired return from depth and surface clutter and (2) range sidelobes from the very strong return from the top surface at nadir.

mode was designed to measure subsurface horizons in the lunar dielectric constant in both side-looking and down-looking viewing geometry. The instrument was based on synthetic aperture radar (SAR) principles. The data were recorded directly onto 70-mm photographic film, which was processed through a combination of optical and digital means following return of *Apollo 17* to Earth. (Optical processing was the state-of-the-art back in 1972 for SAR data.) Penetration depths proved to be approximately proportional to wavelength. The radar's waveform was constrained so that all sidelobes were at least 45 dB below the main-beam peak for all responses beyond three impulse widths of the compressed signal. Amplitude and phase linearity were constrained to be better than 0.1% and 0.001 radian, respectively. The transmitted pulses were linear FM, at 10% bandwidth in all three bands. Nominal free-space resolutions were 300 m, 100 m, and 10 m. Antenna gains were -0.8 dB, -0.7 dB, and +7.3 dB. These low numbers follow from the poor directivity of the antenna. Transmitted average power was 12 W, 4 W, and 1.5 W. Penetration depths were predicted to be 1300 m, 800 m, and 160 m, which turned out to be consistent with ALSE's performance.

MARSIS. The European Space Agency's *Mars Express* spacecraft includes the Mars Advanced Radar for Subsurface and Ionospheric Sounding instrument,¹⁴⁶ the first orbital sounder to fly since ALSE. MARSIS is a multifrequency down-looking radar that radiates 1-MHz pulses in one of four bands centered on the frequencies cited in Table 18.9. *Mars Express* is in an elliptical orbit; subsurface sounding operations are restricted to the lower 250 km to 800 km altitudes. Sounding is further limited by the ionosphere, which prevents effective radio wave propagation to the surface at frequencies below the plasma frequency f_0 , which at Mars is ~4 MHz on the sunlit side and ~1 MHz on the dark side. The ionosphere induces a frequency-dependent time delay on the signal according to the index of refraction n , where $n = [1 - (f_0/f)^2]^{1/2}$. The resulting dispersion distorts the radar modulation, which must be compensated before pulse compression. The 40-m dipole antenna oriented orthogonal to the orbit plane is only weakly directive, with a 2.1 dB gain. The two 20-m long elements were not unfurled until two years into the mission, due to concerns about their potential for damaging the spacecraft during deployment. The effective cross-track footprint is on the order of 25 km. The along-track footprint is about 5 km, which is the result of onboard coherent doppler processing. This strategy reduces the impact of off-nadir clutter arising from sources in the along-track direction. The technique improves the subclutter visibility by 10 dB or more. The radar's mass and input power are 17 kg and 64 W. Peak radiated power is 10 W. The system noise floor is about 50 dB below the mean surface return, which establishes the dynamic range that limits depth of penetration. MARSIS has performed as intended,¹⁴⁷ with early results from the polar layered deposits, for example.

SHARAD. The Shallow Radar sounder¹⁴⁸ was designed to complement MARSIS. In general terms, it has higher resolution at a higher frequency, designed to provide sharper differentiation of the upper several hundred meters of the surface of Mars. SHARAD transmits a 10-MHz linear FM signal centered at 20 MHz. Theoretical vertical resolution is 7.5 m in material having a permittivity of 4. The 10-m dipole antenna has a frequency-dependent two-way gain of -5.7 dB to +0.2 dB. The effective beam footprint (after doppler processing) is ~0.5 km along track and ~5 km across track. Nominal SNR with respect to the surface return is in excess of 50 dB. Instrument mass is ~17 kg, input power is ~45 W. SHARAD measurements started late 2006 only when the MRO orbit was circularized after six months of aerobraking.

SELENE. The Japanese lunar mission, SELENE,¹⁴⁹ includes a 5 MHz Lunar Radar Sounder (LRS)¹⁵⁰ as one of its 14 payload instruments. The orbit is circular at 100-km altitude. The radar transmits 200 μ sec linear FM signals that are demodulated using the stretch technique, similar to radar altimeters. Each pulse is amplitude-weighted by a sine function ($0, \pi$) to suppress sidelobes by \sim 30 dB from the surface return that otherwise would mask the desired returns from depth. The in situ resolution is nominally \sim 40 m within a medium of permittivity \sim 4. The radar dynamic range is \sim 50 dB to permit observation of subsurface profiles to a depth of several km. The antenna is comprised of two sets of dipoles, 30 m tip-to-tip, with an effective footprint of several tens of km. Peak output power is 800 W. Instrument mass is 24 kg and input power 50 W.

Atmospheric & Ionospheric Sounding–Flight Systems. The objective of this class of radar sounders is to generate a cross-section (profile) of the water or electron density in the orbit plane beneath the spacecraft. Atmospheric sounding by radar requires sensitivity to relatively weak backscatter, effective suppression (or avoidance) of the strong return from nadir, modest range resolution, and relatively narrow fields of view. These requirements lead to high power radars at K_u band or above, a simple pulse waveform, and substantial antenna area.

Radar sounders should not be confused with (passive) microwave radiometers—also called sounders, unfortunately—that are used by operational meteorological satellites to estimate atmospheric water distribution. A multifrequency radiometer generates coarse water vapor density profiles for which altitude is a function of frequency. Passive microwave sounding units have mass and power requirements on the order of 50 kg and 75 W, much less than their active radar counterparts.

TRMM. The Tropical Rainfall Measuring Mission was a joint undertaking between NASA and the Japanese Aerospace Exploration Agency (JAXA). The five-instrument payload includes the Precipitation Radar¹⁵¹ (PR), which was designed and built by JAXA (then NASDA), and was the first of its kind on a space-based platform. Its precessing 400-km orbit, inclined at 35° , supports temporally and spatially sparse atmospheric coverage over tropical land and sea. The radar provides a three-dimensional structure of rainfall from the surface to an altitude of 20 km. When combined with data from the passive microwave radiometer (TMI), PR data support improved accuracy of rainfall retrievals. The radar's K_u band (\sim 2 cm) frequency is about three times higher than most surface-based meteorological radars, but was selected to achieve a reasonably narrow 0.71° beamwidth from an antenna area constrained by spacecraft accommodation to be no more than 2.1 m by 2.1 m. Horizontal resolution at nadir is about 4.3 km. The antenna, a 128-element slotted waveguide phased array with 47 dB gain, is electronically scanned over $\pm 17^\circ$ across track, covering a swath 220-km wide, centered at nadir. Peak transmitted power is 500 W, generated from 128 solid-state power amplifiers (SSPAs), one for each waveguide. The 250-m range resolution is set by the unity time-bandwidth-product 1.6 μ sec pulse. The radar has sufficient sensitivity to respond to rain rates as small as 0.7 mm/hr. Instrument mass is 465 kg; required input power is 250 W.

The ionospheric sounding mode on MARSIS (described above) is aimed primarily at characterization of the Martian ionosphere¹⁵² during daylight conditions from altitudes below 1200 km. The radar is operated as a stepped-frequency instrument, sweeping 100 kHz to 5.4 MHz in 10.937 kHz intervals, over 7.38 seconds. From 500 km, the nominal SNR is 5.4 dB, increasing to 21.3 dB at 3.0 MHz.

CloudSat. Launched in April 2006, CloudSat includes as its primary payload the Cloud Profiling Radar¹⁵³ (CPR). CloudSat¹⁵⁴ flies in a sun-synchronous orbit in close formation with CALIPSO, which carries a cloud-profiling lidar, and in somewhat looser formation with Aqua, Aura, Terra, and PARASOL. Taken together, these six environmental satellites constitute the so-called A-Train. The average separation between CloudSat and CALIPSO is about 460 km, which corresponds to a one-minute delay between the radar and lidar cloud profiling measurements. The CPR was developed jointly by NASA and the Canadian Space Agency. It is a 94 GHz nadir-viewing real aperture radar, transmitting 3.3 μ sec pulses at a PRF of 4.3 kHz to fill a window from the surface to 25 km altitude with 500-m vertical resolution sounding data. The antenna diameter, limited by the launch vehicle shroud, is 1.95 m, which supports across-track and along-track resolutions of 1.4 km and 2.5 km, respectively. The larger along-track resolution reflects the 0.3-sec integration time of the returns. Antenna gain is 63 dB. Average data rate is 15 kbit/s. Dynamic range is 70 dB; minimum detectable volumetric return is -26 dBZ. The PR mass is 230 kg; input power required is 270 W. Peak power transmitted is 1.7 kW.

The CPR's high-power amplifier (HPA) is the first of its kind for a space-based radar, an extended interaction klystron.¹⁵⁵ The klystron is driven by 200 mW signals from a solid-state preamplifier. The klystron requires 20 kV, provided by a high-voltage power supply system that also is a space first. The HPA is fully redundant.

DPR. The dual-frequency precipitation radar is the active microwave instrument¹⁵⁶ for the Global Precipitation Measurement (GPM) Core Observatory. DPR is based on a K_u band instrument (KuPR) similar to its predecessor on TRMM, augmented by a K_a band (35.55 GHz) radar (KaPR). Their two phased array slotted waveguide antennas are sized and oriented so that their footprints are the same. Their respective steered beams are synchronized so that for the central 100-km swath within which they both have coverage, their vertical profiles are near-simultaneous. The KuPR and KaPR antennas are sized at 2.4 m \times 2.4 m and 1.4 m \times 1.0 m, respectively, each comprised of 148 slotted waveguides driven by individual solid-state power amplifiers. Peak transmitted powers are 700 W and 140 W. Mass and input power of the two radars are 450 kg and 330 kg and 384 W and 326 W. The only other instrument in the payload is a microwave radiometer. To provide coverage at more latitudes, the spacecraft has a higher inclination orbit than TRMM's 39°. The main advantages of the second frequency and increased power are to distinguish between rain and snow and to increase sensitivity to rain rates as low as 0.2 mm/hr.

REFERENCES

1. D. E. Barrick and C. T. Swift, "The Seasat microwave instruments in historical perspective," *IEEE Journal of Oceanic Engineering*, vol. OE-5, pp. 74–79, 1980.
2. D. L. Evans, W. Alpers, A. Cazenave, C. Elachi, T. Farr, D. Glackin, B. Holt, L. Jones, W. T. Liu, W. McCandless, Y. Menard, R. Moore, and E. Njoku, "Seasat—A 25-year legacy of success," *Remote Sensing of Environment*, vol. 94, pp. 384–404, 2005.
3. M. D. Griffin and J. R. French, *Space Vehicle Design*, American Institute of Aeronautics and Astronautics, 2004.
4. V. J. Pisacane, *Fundamentals of Space Systems*, 2nd Ed, Oxford: Oxford University Press, 2005.
5. F. M. Henderson and A. J. Lewis (eds.), *Principles and Applications of Imaging Radar*, New York: J. Wiley & Sons Inc., 1998.

6. C. A. Wiley, "Synthetic Aperture Radars—A paradigm for technology evolution," *IEEE Transactions on Aerospace and Electronic Systems*, vol. AES-21, pp. 440–443, 1985.
7. H. Jensen, L. C. Graham, L. J. Porcello, and E. N. Leith, "Side-looking airborne radar," *Scientific American*, vol. 237, pp. 84–95, 1977.
8. R. L. Jordan, "The Seasat-A synthetic-aperture radar system," *IEEE Journal of Oceanic Engineering*, vol. OE-5, pp. 154–164, 1980.
9. R. L. Jordan, B. L. Huneycutt, and M. Werner, "The SIR-C/X-SAR synthetic aperture radar system," *Proceedings of the IEEE*, vol. 79, pp. 827–838, 1991.
10. A. Freeman, M. Alves, B. Chapman, J. Cruz, Y. Kim, S. Shaffer, J. Sun, E. Turner, and K. Sarabandi, "SIR-C data quality and calibration results," *IEEE Transactions on Geoscience and Remote Sensing*, vol. 33, pp. 848–857, 1995.
11. B. Rabus, M. Eineder, A. Roth, and R. Bamler, "The shuttle topography mission—a new class of digital elevation models acquired by spaceborne radar," *Photogrammetry and Remote Sensing*, vol. 57, pp. 241–262, 2003.
12. W. Yirong, Z. Minhui, and H. Wen, "SAR activities in P.R. China," in *Proceedings, 6th European Conference on Synthetic Aperture Radar*, Dresden, Germany, VDE Verlag, 2006.
13. Y. Sharay and U. Naftaly, "TECSAR: design considerations and programme status," *IEE Proc. Radar Sonar Navigation*, vol. 153, pp. 117–121, 2006.
14. E. P. W. Attema, "The active microwave instrument on-board the ERS-1 satellite," *Proceedings of the IEEE*, vol. 79, pp. 791–799, 1991.
15. R. Bamler, M. Eineder, B. Kampes, H. Runge, and N. Adam, "SRTM and beyond: Current situation and new developments in spaceborne InSAR," in *Proceedings, ISPRS Workshop on High Resolution Mapping from Space*, Hanover, Germany, 2003.
16. Y. Nemoto, H. Nishino, M. Ono, H. Mizutamari, K. Nishikawa, and K. Tanaka, "Japanese earth resources satellite-1 synthetic aperture radar," *Proceedings of the IEEE*, vol. 79, pp. 800–809, 1991.
17. R. K. Raney, A. P. Luscombe, E. J. Langham, and S. Ahmed, "RADARSAT," *Proceedings of the IEEE*, vol. 79, pp. 839–849, 1991.
18. K. C. Jezek, K. Farness, R. Carande, X. Wu, and N. Labelle-Hamer, "RADARSAT-1 synthetic aperture radar observations of Antarctica: Modified Antarctic Mapping Mission, 2000," *Radio Science*, vol. 38, pp. 8067, 2003.
19. A. Ali, I. Barnard, P. A. Fox, P. Duggan, R. Gray, P. Allan, A. Brand, and R. Ste-Mari, "Description of RADARSAT-2 synthetic aperture radar design," *Canadian J. Remote Sensing*, vol. 30, pp. 246–257, 2004.
20. P. A. Fox, A. P. Luscombe, and A. A. Thompson, "RADARSAT-2 SAR modes development and utilization," *Canadian J. Remote Sensing*, vol. 30, pp. 258–264, 2004.
21. C. Zelli, "ENVISAT RA-2 Advanced radar altimeter: Instrument design and pre-launch performance assessment review," *Acta Astronautica*, vol. 44, pp. 323–333, 1999.
22. S. R. Cloude, G. Krieger, and K. P. Papathanassiou, "A framework for investigating space-borne polarimetric interferometry using the ALOS-PALSAR sensor," in *Proceedings IEEE Geoscience and Remote Sensing Symposium IGARSS2005*, Alaska, IEEE, 2005.
23. M. Shimada, M. Watanabe, T. Moriyama, and T. Tadono, "PALSAR characterization and initial calibration," in *Proceedings IEEE International Geoscience and Remote Sensing Symposium IGARSS2006*, Denver, CO, IEEE, 2006.
24. A. Moreira, G. Krieger, D. Hounam, M. Werner, S. Riegger, and E. Settelmeyer, "TanDEM-X: A TerraSAR-X add-on satellite for single-pass SAR interferometry," in *Proc. International Geoscience and Remote Sensing Symposium IGARSS 2004*, Anchorage, Alaska, IEEE, 2004.
25. R. Levy-Nathansohn and U. Naftaly, "Overview of the TECSAR satellite modes of operation," in *Proceedings, 6th European Conference on Synthetic Aperture Radar*, Dresden, Germany, VDE Verlag, 2006.
26. Y. Wu, M. Zhu, and W. Hong, "SAR activities in P. R. China," in *Proceedings of EUSAR*, Dresden, Germany, ITG VDE, 2006.

27. T. Misra, S. S. Rana, V. H. Bora, N. M. Desai, C. V. N. Rao, and N. Rajeevjiyothi, "SAR payload of radar imaging satellite RISAT) of ISRO," in *Proceedings, 6th European Conference on Synthetic Aperture Radar*, Dresden, Germany, VDE Verlag, 2006.
28. R. Schroeder, J. Puls, F. Jochim, J.-L. Bueso-Bello, L. Datasvili, H. Baier, M. M. Quintino da Silve, and W. Paradella, "The MAPSAR mission: Objectives, design, and status," in *Proceedings of EUSAR*, Dresden, Germany, ITG VDE, 2006.
29. H. Kimura and N. Itoh, "ALOS PALSAR: The Japanese second-generation spaceborne SAR and its application," *Proc. Society of Photo-optical Instrumentation Engineers (SPIE)*, vol. 4152, pp. 110–119, 2000.
30. J. C. Curlander and R. N. McDonough, *Synthetic Aperture Radar: Systems and Signal Processing*, New York: John Wiley & Sons, Inc., 1991.
31. R. K. Raney, "Radar fundamentals: technical perspective," in *Principles and Applications of Imaging Radar*, F. Henderson and A. Lewis (eds.), New York: Wiley Interscience, 1998, pp. 9–130.
32. G. Franceschetti and R. Lanari, *Synthetic Aperture Radar Processing*, Boca Raton, FL: CRC Press, 1999.
33. R. K. Raney, "Considerations for SAR image quantification unique to orbital systems," *IEEE Transactions on Geoscience and Remote Sensing*, vol. 29, pp. 754–760, 1991.
34. P. E. Green, Jr., "Radar measurements of target scattering properties," In *Radar Astronomy*, J. V. Evans and T. Hagfors (eds.), New York: McGraw-Hill, 1968.
35. W. G. Carrara, R. S. Goodman, and R. M. Majewski, *Spotlight Synthetic Aperture Radar—Signal Processing Algorithms*, Boston: Artech House, 1995.
36. C. V. Jakowatz, D. E. Wahl, P. H. Eichel, D. C. Ghiglia, and P. A. Thompson, *Spotlight-Mode Synthetic Aperture Radar: A Signal Processing Approach*, Boston: Kluwer Academic Publishers, 1996.
37. R. Bamler, "Optimum look weighting for burst-mode and scanSAR processing," *IEEE Transactions on Geoscience and Remote Sensing*, vol. 33, pp. 722–725, 1995.
38. K. Tomiyasu, "Conceptual performance of a satellite-borne, wide swath synthetic aperture radar," *IEEE Transactions on Geoscience and Remote Sensing*, vol. 19, pp. 108–116, 1981.
39. R. K. Moore, J. P. Claasen, and Y. H. Lin, "Scanning spaceborne synthetic aperture radar with integrated radiometer," *IEEE Transactions on Aerospace and Electronic Systems*, vol. AES-17, pp. 410–421, 1981.
40. A. Luscombe, A. Thompson, P. James, and P. Fox, "Calibration techniques for the RADARSAT-2 SAR system," in *Proceedings of EUSAR 2006*, Dresden, Germany, VDE Verlag, 2006.
41. W. M. Boerner, H. Mott, E. Luneburg, C. Livingstone, B. Brisco, R. J. Brown, and J. S. Paterson, "Polarimetry in radar remote sensing: basic and applied concepts," in *Principles and Applications of Imaging Radar*, F. M. Henderson and A. J. Lewis (eds.), New York: John Wiley & Sons, Inc., 1998.
42. L. Graham, "Synthetic interferometers for topographic mapping," *Proc. IEEE*, vol. 62, pp. 763–768, 1974.
43. R. Gens and J. vanGenderen, "Review article: SAR interferometry—issues, techniques, applications," *Int. J. Remote Sensing*, vol. 17, pp. 1803–1835, 1996.
44. P. Rosen, S. Hensley, I. Joughin, F. Li, S. Madsen, E. Rodriguez, and R. Goldstein, "Synthetic aperture radar interferometry," *Proc. IEEE*, vol. 88, pp. 333–382, 2000.
45. R. F. Hanssen, *Radar Interferometry*, Dordrecht, The Netherlands: Kluwer Academic Publishers, 2001.
46. H. Zebker and R. Goldstein, "Topographic mapping from interferometric synthetic aperture radar observations," *J. Geophys. Res.*, vol. 91, pp. 4993–4999, 1986.
47. S. Madsen, H. Zebker, and J. Martin, "Topographic mapping using radar interferometry," *IEEE Trans Geoscience and Remote Sensing*, vol. 31, pp. 246–256, 1993.
48. A. Gabriel, R. Goldstein, and H. Zebker, "Mapping small elevation changes over large areas: Differential radar interferometry," *J. Geophys. Res.*, vol. 94, pp. 9183–9191, 1989.
49. D. Massonnet and K. Feigl, "Radar interferometry and its application to changes in the Earth's surface," *Rev. Geophysics*, vol. 36, pp. 441–500, 1998.

50. M. Born and E. Wolf, *Principles of Optics*, New York: Pergamon Press, Macmillan, 1959.
51. F. Gatelli, A. Guarneri, F. Parizzi, P. Pasquali, C. Prati, and F. Rocca, "The wavenumber shift in SAR interferometry," *IEEE Trans Geoscience and Remote Sensing*, vol. 32, pp. 855–865, 1994.
52. H. Zebker and J. Villasenor, "Decorrelation in interferometric radar echoes," *IEEE Trans Geoscience and Remote Sensing*, vol. 30, pp. 950–959, 1992.
53. A. Ferretti, C. Prati, and F. Rocca, "Nonlinear subsidence rate estimation using permanent scatterers in differential SAR interferometry," *IEEE Trans Geoscience and Remote Sensing*, vol. 38, pp. 2202–2212, 2000.
54. T. H. Dixon, F. Amelung, A. Ferretti, F. Novali, F. Rocca, R. Dokka, G. Sella, S.-W. Kim, S. Wdowinski, and D. Whitman, "Space geodesy: Subsidence and flooding in New Orleans," *Nature*, vol. 441, pp. 587–588, 2006.
55. D. Ghiglia and M. Pritt, *Two-dimensional Phase Unwrapping: Theory, Algorithms, and Software*, New York: Wiley, 1998.
56. R. Goldstein and C. Werner, "Radar interferogram filtering for geophysical applications," *Geophysical Res. Letters*, vol. 25, pp. 4035–4038, 1998.
57. J. J. van Zyl, H. A. Zebker, and C. Elachi, "Imaging radar polarization signatures: Theory and observation," *Radio Science*, vol. 22, pp. 529–543, 1987.
58. P. E. Green Jr., "Radar measurements of target scattering properties," in *Radar Astronomy*, J. V. Evans and T. Hagfors (eds.), New York: McGraw-Hill Book Company, 1968, pp. 1–78.
59. A. Guissard, "Meuller and Kennaugh matrices in radar polarimetry," *IEEE Transactions on Geoscience and Remote Sensing*, vol. 32, pp. 590–597, 1994.
60. C. Lopez-Martinez, E. Pottier, and S. R. Cloude, "Statistical assessment of Eigenvector-based target decomposition theorems in radar polarimetry," *IEEE Trans. Geoscience and Remote Sensing*, vol. 43, pp. 2058–2074, 2005.
61. S. R. Cloude and K. P. Papathanassiou, "Polarimetric SAR interferometry," *IEEE Trans Geoscience and Remote Sensing*, vol. 36, pp. 1551–1565, 1998.
62. S. R. Cloude and E. Pottier, "An entropy based classification scheme for land applications of polarimetric SAR," *IEEE Trans. Geoscience and Remote Sensing*, vol. 35, pp. 68–78, 1997.
63. L.-L. Fu and A. Cazenave (eds.), *Satellite Altimetry and the Earth Sciences*, San Diego: Academic Press, 2001.
64. J. R. Jensen and R. K. Raney, "Delay Doppler radar altimeter: Better measurement precision," in *Proceedings IEEE Geoscience and Remote Sensing Symposium IGARSS'98*, Seattle, WA, IEEE, 1998, pp. 2011–2013.
65. R. K. Moore and C. S. Williams, Jr., "Radar return at near-vertical incidence," *Proceedings of the IRE*, vol. 45, pp. 228–238, 1957.
66. G. S. Brown, "The average impulse response of a rough surface and its applications," *IEEE Antennas and Propagation*, vol. 25, pp. 67–74, 1977.
67. E. J. Walsh, "Pulse-to-pulse correlation in satellite radar altimetry," *Radio Science*, vol. 17, pp. 786–800, 1982.
68. J. T. McGoogan, L. S. Miller, G. S. Brown, and G. S. Hayne, "The S-193 radar altimeter experiment," *Proceedings of the IEEE*, vol. 62, pp. 793–803, 1974.
69. G. S. Hayne, "Radar altimeter mean return waveforms from near-normal incidence ocean surface scattering," *IEEE Antennas and Propagation*, vol. AP-28, pp. 687–692, 1980.
70. J. L. MacArthur, C. C. Kilgus, C. A. Twigg, and P. V. K. Brown, "Evolution of the satellite radar altimeter," *Johns Hopkins APL Technical Digest*, vol. 10, pp. 405–413, October–December 1989.
71. J. L. MacArthur, P. C. Marth, and J. G. Wall, "The GEOSAT radar altimeter," *Johns Hopkins APL Technical Digest*, vol. 8, pp. 176–181, 1987.
72. W. H. F. Smith and D. T. Sandwell, "Bathymetric prediction from dense satellite altimetry and sparse shipboard bathymetry," *J. Geophys. Res.*, vol. 99, pp. 21803–21824, 1994.
73. D. T. Sandwell and W. H. F. Smith, "Bathymetric estimation," in *Satellite Altimetry and Earth Sciences*, L.-L. Fu and A. Cazenave (eds.), New York: Academic Press, 2001, pp. 441–457.
74. APL, Special sections, "Geosat science and altimeter technology," *Johns Hopkins APL Technical Digest*, vol. 10, 1989.

75. D. B. Chelton, J. C. Ries, B. J. Haines, L.-L. Fu, and P. S. Callahan, "Satellite altimetry," in *Satellite Altimetry and Earth Sciences*, L.-L. Fu and A. Cazenave (eds.), San Diego: Academic Press, 2001, pp. 1–122.
76. J. Goldhirsh and J. R. Rowland, "A tutorial assessment of atmospheric height uncertainties for high-precision satellite altimeter missions to monitor ocean currents," *IEEE Transactions on Geoscience and Remote Sensing*, vol. 20, pp. 418–434, 1982.
77. D. J. Wingham, I. Phalippou, C. Mavrocordatos, and D. Wallis, "The mean echo and echo cross-product from a beamforming interferometric altimeter and their application to elevation measurements," *IEEE Transactions on Geoscience and Remote Sensing*, vol. 42, pp. 2305–2323, 2004.
78. P. Vincent, N. Steunou, E. Caubet, L. Phalippou, L. Rey, E. Thouvenot, and J. Verron, "AltiKa: a Ka-band altimetry payload and system for operational altimetry during the GMES period," *Sensors*, vol. 6, pp. 208–234, 2006.
79. M. E. Parke, R. H. Stewart, D. L. Farless, and D. E. Cartwright, "On the choice of orbits for an altimetric satellite to study ocean circulation and tides," *Journal of Geophysical Research*, vol. 92, pp. 11693–11707, October 15, 1987.
80. D. T. Sandwell and W. H. F. Smith, "Marine gravity anomaly from Geosat and ERS-1 satellite altimetry," *J. Geophys. Res.*, vol. 102, pp. 10039–10054, 1997.
81. R. D. Ray, "Applications of high-resolution ocean topography to ocean tides," in *Report of the High-Resolution Ocean Topography Science Working Group Meeting*, D. Chelton (ed.), Corvallis, Oregon: Oregon State University, 2001.
82. R. Scharrroo and P. Visser, "Precise orbit determination and gravity field improvement for the ERS satellites," *J. of Geophysical Research*, vol. 103, pp. 8113–8127, 1998.
83. A. R. Zieger, D. W. Hancock, G. S. Hayne, and C. L. Purdy, "NASA radar altimeter for the TOPEX/Poseidon project," *Proceedings of the IEEE*, vol. 79, pp. 810–826, June 1991.
84. P. C. Marth, J. R. Jensen, C. C. Kilgus, J. A. Perschy, J. L. MacArthur, D. W. Hancock, G. S. Hayne, C. L. Purdy, L. C. Rossi, and C. J. Koblinsky, "Prelaunch performance of the NASA altimeter for the TOPEX/Poseidon Project," *IEEE Transactions on Geoscience and Remote Sensing*, vol. 31, pp. 315–332, 1993.
85. D. B. Chelton, E. J. Walsh, and J. L. MacArthur, "Pulse compression and sea-level tracking in satellite altimetry," *Journal of Atmospheric and Oceanic Technology*, vol. 6, pp. 407–438, 1989.
86. W. J. J. Caputi, "Stretch: a time-transformation technique," *IEEE Transactions on Aerospace and Electronic Systems*, vol. AES-7, pp. 269–278, 1971.
87. D. T. Sandwell, "Antarctic marine gravity field from high-density satellite altimetry," *Geophys. J. Int.*, vol. 109, pp. 437–448, 1992.
88. W. H. F. Smith and D. T. Sandwell, "Conventional bathymetry, bathymetry from space, and geodetic altimetry," *Oceanography*, vol. 17, pp. 8–23, 2004.
89. M. M. Yale, D. T. Sandwell, and W. H. F. Smith, "Comparison of along-track resolution of stacked Geosat, ERS-1 and TOPEX satellite altimeters," *J. Geophys. Res.*, vol. 100, pp. 15117–15127, 1995.
90. L. Phalippou, L. Rey, P. DeChateau-Thierry, E. Thouvenot, N. Steunou, C. Mavrocordatos, and R. Francis, "Overview of the performances and tracking design of the SIRAL altimeter for the CryoSat mission," in *Proceedings IEEE International Geoscience and Remote Sensing Symposium*, pp. 2025–2027, 2001.
91. R. K. Raney, "The delay doppler radar altimeter," *IEEE Transactions on Geoscience and Remote Sensing*, vol. 36, pp. 1578–1588, 1998.
92. J. R. Jensen, "Design and performance analysis of a phase-monopulse radar altimeter for continental ice sheet monitoring," in *Proceedings, IEEE International Geoscience and Remote Sensing Symposium IGARSS'95*, Florence, Italy, IEEE, 1995, pp. 865–867.
93. R. K. Raney and J. R. Jensen, "An Airborne CryoSat Prototype: The D2P Radar Altimeter," in *Proceedings of the International Geoscience and Remote Sensing Symposium IGARSS'02*, Toronto, IEEE, 2002, pp. 1765–1767.
94. S. Laxon, N. Peacock, and D. Smith, "High interannual variability of sea ice thickness in the Arctic region," *Letters to Nature*, vol. 425, pp. 947–950, 2003.

95. A. J. Butrica, *To See the Unseen: A History of Planetary Radar*, Darby, PA: Diane Publications, 1997.
96. S. J. Ostro, "Planetary radar astronomy," in *The Encyclopedia of Physical Science and Technology, 3rd Edition*, R. A. Meyers (ed.), San Diego, Academic Press, 2002, pp. 295–328.
97. D. B. Campbell, R. S. Hudson, and J.-L. Margot, "Advances in planetary radar astronomy," Chapter 35, in *Review of Radio Science, 1999–2002*, R. Stone (ed.), Oxford: U.R.S.I, 2002, pp. 869–899.
98. S. Slavney, R. E. Arvidson, K. Bennett, E. A. Guiness, and T. C. Stein, "Recent and planned Planetary Data System geosciences node activities," Paper 2232.pdf, *Proceedings, Lunar and Planetary Science XXXVII*, Houston, TX, vol., 2006.
99. G. H. Pettengill, P. G. Ford, and B. D. Chapman, "Venus: surface electromagnetic properties," *J. Geophys. Res.*, vol. 93, pp. 14881–14892, 1988.
100. B. A. Ivanov, "Venusian impact craters on Magellan images: View from Venera 15/16," *Earth Moon Planet*, vol. 50/51, pp. 159–173, 1990.
101. G. H. Pettengill, P. G. Ford, W. T. K. Johnson, R. K. Raney, and L. A. Soderblom, "Magellan: Radar performance and data products," *Science*, vol. 252, pp. 260–265, 1991.
102. W. T. K. Johnson, "Magellan imaging radar mission to Venus," *Proceedings of the IEEE*, vol. 79, pp. 777–790, 1991.
103. C. Elachi, E. Im, L. E. Roth, and C. L. Werner, "Cassini Titan radar mapper," *Proceedings of the IEEE*, vol. 79, pp. 867–880, 1991.
104. S. Nozette, C. L. Lichtenberg, P. Spudis, R. Bonner, W. Ort, E. Malaret, M. Robinson, and E. M. Shoemaker, "The Clementine bistatic radar experiment," *Science*, vol. 274, pp. 1495–1498, November 29, 1996.
105. B. Hapke, "Coherent backscatter and the radar characteristics of outer planet satellites," *Icarus*, vol. 88, pp. 407–417, December 1990.
106. R. A. Simpson and G. L. Tyler, "Reanalysis of Clementine bistatic radar data from the lunar South Pole," *J. Geophys. Res.*, vol. 104, pp. 3845–3862, February 25, 1999.
107. D. B. Campbell, B. A. Campbell, L. M. Carter, J.-L. Margot, and N. J. S. Stacy, "No evidence for thick deposits of ice at the lunar south pole," *Nature*, vol. 443, pp. 835–837, 2006.
108. M. T. Zuber and I. Garrick-Bethell, "What do we need to know to land on the Moon again?," *Science*, vol. 310, pp. 983–985, 2005.
109. K. J. Peters, "Coherent-backscatter effect: A vector formulation accounting for polarization and absorption effects and small or large scatterers," *Physical Review B*, vol. 46, pp. 801–812, 1 July 1992.
110. P. D. Spudis, C. L. Lichtenberg, B. Marinelli, and S. Nozette, "Mini-SAR: An imaging radar for the Chandrayaan-1 mission to the Moon," Paper 1153, *Proceedings, Lunar and Planetary Science XXXVI*, Houston, TX, vol., 2005.
111. R. K. Raney, "Hybrid-polarity SAR architecture," in *Proceedings IEEE Geoscience and Remote Sensing Symposium*, Denver, CO, IEEE, 2006.
112. D. J. Mudgway, *Big Dish: Building America's Deep Space Connection to the Planets*, Gainesville: University of Florida Press, 2005.
113. R. K. Moore, "Trade-off between picture element dimensions and noncoherent averaging in side-looking airborne radar," *IEEE Transactions on Aerospace and Electronic Systems*, vol. 15, pp. 697–708, 1979.
114. R. K. Raney, "The making of a precedent: the synthetic aperture radar (SAR) on Magellan," *V-GRAM (Jet Propulsion Laboratory)*, vol. 9, pp. 3–10, 1986.
115. R. Kwok and W. T. K. Johnson, "Block adaptive quantization of Magellan SAR data," *IEEE Transactions on Geoscience and Remote Sensing*, vol. 27, pp. 375–383, 1989.
116. G. G. Stokes, "On the composition and resolution of streams of polarized light from different sources," *Transactions of the Cambridge Philosophical Society*, vol. 9, pp. 399–416, 1852.
117. S. R. Cloude and E. Pottier, "A review of target decomposition theorems in radar polarimetry," *IEEE Trans. Geoscience and Remote Sensing*, vol. 34, pp. 498–518, 1996.
118. R. K. Raney, "Stokes parameters and hybrid-polarity SAR architecture," *IEEE Transactions Geoscience and Remote Sensing*, vol. 45, pp. 3397–3404, 2007.

119. Y. Quilfen, B. Chapron, F. Collard, and D. Vandemark, "Relationship between ERS scatterometer measurement and integrated wind and wave parameters," *J. Atmospheric and Oceanic Technology*, vol. 21, pp. 368–373, 2004.
120. R. K. Moore and A. K. Fung, "Radar determination of winds at sea," *Proceedings of the IEEE*, vol. 67, pp. 1504–1521, 1979.
121. J. Kerkmann, *Review on Scatterometer Winds*, Darmstadt, Germany: European Organization for the Exploitation of Meteorological Satellites EUMETSAT, 1998, p. 77.
122. A. Mouche, D. Hauser, and V. Kudryavstev, "Observations and modelling of the ocean radar backscatter at C-band in HH- and VV-polarizations," in *Proceedings International Geoscience and Remote Sensing Symposium*, Seoul, Korea, IEEE, 2005.
123. M. Migliaccio, "Sea wind field retrieval by means of microwave sensors: a review," in *Proc. URSI Commission F Symposium*, Ispra, Italy, 2005.
124. E. M. Bracalente, D. H. Boggs, W. L. Grantham, and J. L. Sweet, "The SASS scattering coefficient δ_0 algorithm," *IEEE Journal of Oceanic Engineering*, vol. OE-5, pp. 145–154, 1980.
125. R. E. Fischer, "Standard deviation of scatterometer measurements from space," *IEEE Transactions on Geoscience Electronics*, vol. GE-10, pp. 106–113, 1972.
126. P. W. Gaiser and C. S. Ruf, "Foreword to the special issue on the WindSat Spaceborne Polarimetric Radiometer—calibration/validation and wind vector retrieval," *IEEE Transactions on Geoscience and Remote Sensing*, vol. 44, pp. 467–469, 2006.
127. I. H. Woodhouse and D. H. Hoekman, "Determining land-surface parameters from the ERS wind scatterometer," *IEEE Transactions on Geoscience and Remote Sensing*, vol. 38, pp. 126–140, 2000.
128. D. G. Long, M. R. Drinkwater, B. Holt, S. Saatchi, and C. Bertoia, "Global ice and land climate studies using scatterometer image data," *EOS, Trans. American Geophysical Union*, vol. 82, pp. 503, 2001.
129. M. R. Drinkwater, D. G. Long, and A. W. Bingham, "Greenland snow accumulation estimates from satellite radar scatterometer data," *J. of Geophysical Research*, vol. 106(D24), pp. 33935–33950, 2001.
130. L. B. Kunz and D. G. Long, "Calibrating SeaWinds and QuikSCAT scatterometers using natural land targets," *IEEE Geoscience and Remote Sensing Letters*, vol. 2, pp. 182–186, 2005.
131. R. K. Moore, "Simultaneous active and passive microwave response of the Earth: The Skylab RADSCAT experiment," in *Proceedings of the 9th International Symposium on Remote Sensing*, Ann Arbor, Michigan, 1974, pp. 189–217.
132. M. Shimada and A. Freeman, "A technique for measurement of spaceborne SAR antenna patterns using distributed targets," *IEEE Transactions on Geoscience and Remote Sensing*, vol. 33, pp. 100–114, 1995.
133. W. L. Grantham, E. M. Bracalente, L. W. Jones, and J. W. Johnson, "The Seasat-A satellite scatterometer," *IEEE Journal of Oceanic Engineering*, vol. OE-2, pp. 200–206, 1977.
134. J. W. Johnson, L. A. Williams, Jr., E. M. Bracalente, F. B. Beck, and W. L. Grantham, "Seasat-A satellite scatterometer instrument evaluation," *IEEE Journal of Oceanic Engineering*, vol. OE-5, pp. 138–144, 1980.
135. J. Figa-Saldana, J. J. W. Wilson, E. Attema, R. Gelsthorpe, M. R. Drinkwater, and A. Stoffelen, "The advanced scatterometer (ASCAT) on the meteorological operational (MetOp) platform: a follow-on for European wind scatterometers," *Canadian J. of Remote Sensing*, vol. 28, pp. 404–412, 2002.
136. F. M. Naderi, M. H. Freilich, and D. G. Long, "Spaceborne radar measurement of wind velocity over the ocean—An overview of the NSCAT scatterometer system," *Proceedings of the IEEE*, vol. 79, pp. 850–866, 1991.
137. C. Wu, J. Graf, M. H. Freilich, D. G. Long, M. W. Spencer, W.-Y. Tsai, D. Lisman, and C. Winn, "The SeaWinds scatterometer instrument," in *Proceedings, IEEE International Geoscience and Remote Sensing Symposium*, Pasadena, CA, pp. 1511–1515, 1994.
138. M. W. Spencer, C. Wu, and D. G. Long, "Tradeoffs in the design of a spaceborne scanning pencil beam scatterometer: Application to Sea-Winds," *IEEE Transactions on Geoscience and Remote Sensing*, vol. 35, pp. 115–126, 1997.

139. C. Wu, Y. Liu, K. H. Kellogg, K. S. Pak, and R. L. Glenister, "Design and calibration of the SeaWinds scatterometer," *IEEE Transactions on Aerospace and Electronic Systems*, vol. 39, pp. 94–109, 2003.
140. M. W. Spencer, C. Wu, and D. G. Long, "Improved resolution backscatter measurements with the SeaWinds pencil-beam scatterometer," *IEEE Transactions on Geoscience and Remote Sensing*, vol. 38, pp. 89–104, 2000.
141. S. H. Yueh, "Microwave remote sensing modeling of ocean surface salinity and winds using an empirical sea surface spectrum," in *Proceedings IEEE Geoscience and Remote Sensing Symposium*, Anchorage, AK, 2004.
142. S. Gogineni, D. Tammana, D. Braaten, C. Leuschen, T. Atkins, J. Legarsky, P. Kanagaratnam, J. Stiles, C. Allen, and K. Jezek, "Coherent radar ice thickness measurements over Greenland ice sheet," *Journal of Geophysical Research*, vol. 106, pp. 33761–33772, 2001.
143. S. H. Ward, G. R. Jiracek, and W. I. Linlor, "Electromagnetic reflection from a plane-layered lunar model," *Journal of Geophysical Research*, vol. 73, pp. 1355–1372, 1968.
144. L. J. Porello, R. L. Jordan, J. S. Zelenka, G. F. Adams, R. J. Phillips, W. E. Brown, Jr., S. H. Ward, and P. L. Jackson, "The Apollo lunar sounder radar system," *Proceedings of the IEEE*, vol. 62, pp. 769–783, 1974.
145. W. J. Peeples, W. R. Sill, T. W. May, S. H. Ward, R. J. Phillips, R. L. Jordan, E. A. Abbott, and T. J. Killpack, "Orbital radar evidence for lunar subsurface layering in Maria Serenitatis and Crisium," *J. of Geophysical Research*, vol. 83, pp. 3459–3468, 1978.
146. D. Biccari, F. Ciabattoni, G. Picardi, R. Seu, W. T. K. Johnson, R. L. Jordan, J. Plaut, A. Safaeinili, D. A. Gurnett, R. Orosei, O. Bombaci, F. Provvedi, and E. Zampolini, "Mars advanced radar for subsurface and ionosphere sounding (MARSIS)," in *Proc. 2001 International Conference on Radar*, Beijing, China, 2001.
147. J. Farrell, J. Plaut, A. Gurnett, and G. Picardi, "Detecting sub-glacial aquifers in the North Polar layered deposits with Mars Express/MARSIS," *Geophysical Research Letters*, vol. 32, pp. L11204, June 10, 2005.
148. M. Kato, Y. Takizawa, S. Sasaki, and the SELENE Project Team, "SELENE, the Japanese lunar orbiting satellite mission: present status and science goals," in *Proceedings, Lunar and Planetary Science XXXVII*, Houston, TX, pp. 1233.pdf, 2006.
149. T. Ono, T. Kobayashi, and H. Oya, "Interim report of the Lunar Radar Sounder on-board SELENE spacecraft," in *Proceedings, 35th COSPAR Assembly*, Paris, France, pp. 3315, 2004.
150. E. Im, E., S. L. Durden, S. Tanelli, and K. Pak, "Early results on cloud profiling radar post-launch calibration and operations," in *Proceedings of the IEEE International Geoscience and Remote Sensing Symposium*, Denver, CO, 2006.
151. G. L. Stephens and D. G. Vane, "The CloudSat mission," in *Proceedings IEEE International Geoscience and Remote Sensing Symposium*, Toulouse, France, 2003.
152. A. Roitman, D. Berry, and B. Steer, "State-of-the-art W-band extended interaction klystron for the CloudSat program," *IEEE Transactions on Electron Devices*, vol. 52, pp. 895–898, 2005.
153. Y. Senbokuva, S. Satoh, K. Furukawa, M. Kojima, H. Hanado, N. Takahashi, T. Iquchi, and K. Nakamura, "Development of the spaceborne dual-frequency precipitation radar for the Global Precipitation Measurement mission," in *Proceedings International Geoscience and Remote Sensing Symposium*, Anchorage, Alaska, pp. 3566–3569, 2004.
154. R. Seu, D. Biccari, R. Orosei, L. V. Lorenzoni, R. J. Phillips, L. Marinangeli, G. Picardi, A. Masdea, and E. Zampolini, "SHARAD: the MRO 2005 shallow radar," *Planetary and Space Science*, vol. 52, pp. 157–166, 2004.
155. T. Kozu, T. Kawanishi, H. Kuroiwa, M. Kojima, K. Oikawa, H. Kumagai, K. Okamoto, M. Okamura, H. Nakatuka, and K. Nishikawa, "Development of precipitation radar onboard the Tropical Rainfall Measurement Mission (TRMM) satellite," *IEEE Transactions on Geoscience and Remote Sensing*, vol. 39, pp. 102–116, 2001.
156. D. A. Gurnett, D. L. Kirchner, R. L. Huff, D. D. Morgan, A. M. Persoon, T. F. Averkamp, F. Duru, E. Nielsen, A. Safaeinili, J. J. Plaut, and G. Picardi, "Radar soundings of the ionosphere of Mars," *Science*, vol. 310, pp. 1929–1933, December 23, 2005.